

AO-A194 002

BODY AND SURFACE WAVE MODELING OF OBSERVED SEISMIC
EVENTS PART 2(U) CALIFORNIA INST OF TECH PASADENA
SEISMOLOGICAL LAB R W CLAYTON ET AL. 12 MAY 87

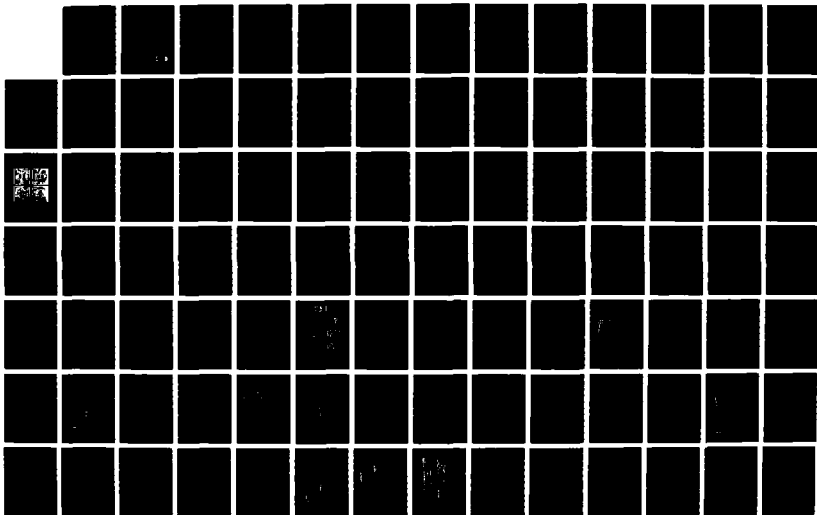
1/2

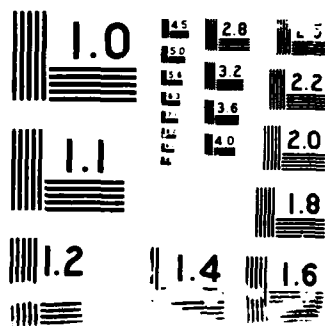
UNCLASSIFIED

AFGL-TR-87-0156 F19620-05-K-0017

F/G 8/11

NL





AFGL-TR-87-0156

DTIC FILE COPY

Body and Surface Wave Modeling of
Observed Seismic Events (Part II)

Robert W. Clayton
David G. Harkrider
Donald V. Helmberger

California Institute of Technology
Seismological Laboratory
Pasadena, CA 91125

12 May, 1987

Semiannual Technical Report No. 3

APPROVED FOR PUBLIC RELEASE; DISTRIBUTION UNLIMITED


AIR FORCE GEOPHYSICS LABORATORY
AIR FORCE SYSTEMS COMMAND
UNITED STATES AIR FORCE
HANSCOM AIR FORCE BASE, MASSACHUSETTS 01731

DTIC
ELECTE
MAY '03 1988
S D
H

88 5 02 325

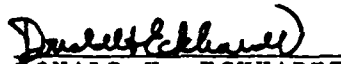
AD-A194 802

"This technical report has been reviewed and is approved for publication"


JAMES F. LEWKOWICZ
Contract Manager


HENRY A. OSSING
Branch Chief

FOR THE COMMANDER


DONALD H. ECKHARDT
Division Director

This report has been reviewed by the ESD Public Affairs Office (PA) and is releasable to the National Technical Information Service (NTIS).

Qualified requestors may obtain additional copies from the Defense Technical Information Center. All others should apply to the National Technical Information Service.

If your address has changed, or if you wish to be removed from the mailing list, or if the addressee is no longer employed by your organization, please notify AFGL/DAA, Hanscom AFB, MA 01731. This will assist us in maintaining a current mailing list.

Do not return copies of this report unless contractual obligations or notices on a specific document requires that it be returned.

UNCLASSIFIED

SECURITY CLASSIFICATION OF THIS PAGE

REPORT DOCUMENTATION PAGE

1a. REPORT SECURITY CLASSIFICATION UNCLASSIFIED			1b. RESTRICTIVE MARKINGS		
2a. SECURITY CLASSIFICATION AUTHORITY			3. DISTRIBUTION/AVAILABILITY OF REPORT Approved for public release; distribution unlimited.		
2b. DECLASSIFICATION/DOWNGRADING SCHEDULE					
4. PERFORMING ORGANIZATION REPORT NUMBER(S)			5. MONITORING ORGANIZATION REPORT NUMBER(S) AFGL-TR-87-0156		
6a. NAME OF PERFORMING ORGANIZATION California Institute of Tech. Seismological Laboratory		6b. OFFICE SYMBOL (If applicable)	7a. NAME OF MONITORING ORGANIZATION Air Force Geophysical Laboratory		
6c. ADDRESS (City, State and ZIP Code) Pasadena, California 91125		7b. ADDRESS (City, State and ZIP Code) Hanscom Air Force Base, Massachusetts 01731			
8a. NAME OF FUNDING/SPONSORING ORGANIZATION Advanced Research Projects Agency		8b. OFFICE SYMBOL (If applicable)	9. PROCUREMENT INSTRUMENT IDENTIFICATION NUMBER F19628-85-K-0017		
8c. ADDRESS (City, State and ZIP Code) (DOD) 1400 Wilson Boulevard Arlington, Virginia 22209		10. SOURCE OF FUNDING NOS.			
		PROGRAM ELEMENT NO. 61102F	PROJECT NO. 5A10	TASK NO. DA	WORK UNIT NO. AA
11. TITLE (Include Security Classification) Body and Surface Wave Modeling of Observed Seismic Events PART II					
12. PERSONAL AUTHOR(S) Robert W. Clayton, David G. Harkrider and Donald V. Helmberger					
13a. TYPE OF REPORT No. 3 Semi-annual Technical		13b. TIME COVERED FROM 1/14/86 TO 7/13/86		14. DATE OF REPORT (Yr., Mo., Day) May 12, 1987	
15. PAGE COUNT 120					
16. SUPPLEMENTARY NOTATION					
17. COSATI CODES			18. SUBJECT TERMS (Continue on reverse if necessary and identify by block number)		
FIELD	GROUP	SUB. GR.	Point -sources from line source 2-D calculations; P-SV and SH applications; Lg propagation; Ocean continent transition zones.		
19. ABSTRACT (Continue on reverse if necessary and identify by block number)					
<p>The research performed under the contract, during the period 14 January 1986 through 13 July 1986, can be divided into two main topics; using 2-D line source calculations to model 3-D point source effects, and the effects of ocean continent transition zones on L_p waves.</p> <p>In section II, we present a scheme for generating synthetic point source seismograms for shear dislocation sources using line source (2-D) theory. It is based on expanding the complete three dimensional solution of the wave equation expressed in cylindrical coordinates in an asymptotic form which provides for the separation of motions into SH</p>					
20. DISTRIBUTION/AVAILABILITY OF ABSTRACT UNCLASSIFIED/UNLIMITED <input type="checkbox"/> SAME AS RPT. <input type="checkbox"/> DTIC USERS <input type="checkbox"/>			21. ABSTRACT SECURITY CLASSIFICATION UNCLASSIFIED		
22a. NAME OF RESPONSIBLE INDIVIDUAL James Lewkowicz		22b. TELEPHONE NUMBER (Include Area Code) (617) 377-3028		22c. OFFICE SYMBOL AFGL/LWH	

(eqn 1) and P-SV systems. We calculate the equations of motion with the aid of the Cagniard-de Hoop technique and derive closed-form expressions appropriate for finite-difference source excitation.

In section III, the effects of a thinning or thickening of the crustal layer on the propagation of L_g mode sum seismograms are examined. The thinning or thickening of the crustal layer is used as a simple model of ocean to continent or continent to ocean transitions. The transition model calculations presented in this section show that passage through a region of thinning crustal thickness, (the model for a continent to ocean transition) increases the amplitude and coda length of the L_g wave at the surface, and allows much of the modal energy trapped in the crust, which forms the L_g phase, to escape into the subcrustal layers as body waves or other downgoing phases. The magnitude of both these effects increases as the length of the transition increases or the slope of the layer boundaries decrease. The passage of the wavefront exiting the continent to ocean transition region through the oceanic structure allows further energy to escape from the crustal layer, and produces a decrease in L_g amplitude at the surface as the length of the oceanic path increases. The amplitude decrease is maximum near the transition region and decreases with distance from it. Passage through a region of thickening crust, the model of an ocean to continent transition, causes a rapid decrease in the L_g amplitude at the surface of the crust. The energy previously trapped in the oceanic crustal layer spreads throughout the thickening crustal layer, and any amplitude which has been traveling through the subcrustal layer but has not reached depths below the base of the continental crust is transmitted back into the continental crust. The attenuation of L_g at the crustal surface along a partially oceanic path occurs in the oceanic structure and in the ocean to continent transition region. The attenuation at the surface depends in part on the escape of energy at depth through the continent to ocean transition region into the underlying half-space.

Accession For	
NTIS GRA&I	<input checked="" type="checkbox"/>
DTIC TAB	<input type="checkbox"/>
Unannounced	<input type="checkbox"/>
Justification	
By	
Distribution/	
Availability Codes	
Dist	Avail and/or Special
A-1	<div style="border: 1px solid black; border-radius: 50%; padding: 5px; display: inline-block;"> COPY INSPECTED 4 </div>

SEMI-ANNUAL TECHNICAL REPORT
14 January 1986 - 13 July 1986

ARPA Order No.: 5299

Name of Contractor: California Institute of Technology

Effective Date of Contract: 14 January 1985

Contract Expiration Date: 13 January 1987

Contract Number: F19628-85-K-0017

Principal Investigators: Robert W. Clayton
(818) 356-6909

David G Harkrider
(818) 356-6910

Donald V. Helmberger
(818) 356-6998

Program Manager: James F. Lewkowicz
(617) 861-3028

Short Title of Work: Body and Surface Wave Modeling of
Observed Seismic Events

The views and conclusions contained in this document are those of the authors and should not be interpreted as necessarily representing the official policies, either expressed or implied, of the Defense Advanced Research Projects Agency of the U. S. Government

Sponsored by
Defense Advanced Research Projects Agency (DOD)
Defense Sciences Office, Geophysical Sciences Division
DARPA/DSO Physical Characterization of Seismic Sources
ARPA Order No. 5299.
Issued by the Air Force Geophysics Laboratory under
Contract# F19628-85-K-0017

Seismological Laboratory
Division of Geological and Planetary Sciences
California Institute of Technology
Pasadena, California 91125

TABLE OF CONTENTS

Summary	v
Modeling strong motions produced by earthquakes with 2-D numerical codes	1
Numerical studies of propagation of L_g waves across ocean continent boundaries using the representation theorem.....	23
Chapter 2: Application of modal propagator matrix to finite element coupling to investigations of L_g propagation across ocean continent boundaries.....	27

I. Summary

The research performed under the contract, during the period 14 January 1986 through 13 July 1986, can be divided into two main topics; using 2-D line source calculations to model 3-D point source effects, and the effects of ocean continent transition zones on L_g waves.

In section II, we present a scheme for generating synthetic point source seismograms for shear dislocation sources using line source (2-D) theory. It is based on expanding the complete three dimensional solution of the wave equation expressed in cylindrical coordinates in an asymptotic form which provides for the separation of motions into SH and P-SV systems. We calculate the equations of motion with the aid of the Cagniard-de Hoop technique and derive closed-form expressions appropriate for finite-difference source excitation.

In section III, the effects of a thinning or thickening of the crustal layer on the propagation of L_g mode sum seismograms are examined. The thinning or thickening of the crustal layer is used as a simple model of ocean to continent or continent to ocean transitions. The transition model calculations presented in this section show that passage through a region of thinning crustal thickness, the model for a continent to ocean transition, increases the amplitude and coda length of the L_g wave at the surface, and allows much of the modal energy trapped in the crust, which forms the L_g phase, to escape into the subcrustal layers as body waves or other downgoing phases. The magnitude of both these effects increases as the length of the transition increases or the slope of the layer boundaries decrease. The passage of the wavefront exiting the continent to ocean transition region through the oceanic structure allows further energy to escape from the crustal layer, and produces a decrease in L_g amplitude at the surface as the length of the oceanic path increases. The amplitude decrease is maximum near the transition region and decreases with distance from it. Passage through a region of thickening crust, the model of a ocean to continent transition, causes a rapid decrease in the L_g amplitude at the surface of the crust. The energy previously trapped in the oceanic crustal layer spreads throughout the thickening crustal layer, and any amplitude which has been traveling through the subcrustal layer but has not reached depths below the base of the continental crust is transmitted back into the continental crust. The attenuation of L_g at the crustal surface along a partially oceanic path occurs in the oceanic structure and in the ocean to continent transition region. The attenuation at the surface depends in part on the escape of energy at depth through the continent to ocean transition region into the underlying half-space.

**Modeling Strong Motions Produced by Earthquakes
With 2-D Numerical Codes**

Donald V. Helmberger

John E. Vidale

March 17, 1987

Abstract

We present a scheme for generating synthetic point-source seismograms for shear dislocation sources using line source (2-D) theory. It is based on expanding the complete three-dimensional solution of the wave equation expressed in cylindrical coordinates in an asymptotic form which provides for the separation of the motions into SH and P-SV systems. We evaluate the equations of motion with the aid of the Cagniard-de Hoop technique and derive close-formed expressions appropriate for finite-difference source excitation.

Introduction

Recent strong motion modeling efforts have been restricted to plane-layered models as displayed in Figure 1a. Point source shear dislocations, or double couples, are applied at each element where the seismic field is decomposed into SH and P-SV type motions and the vertical and horizontal dependences separated following the approach pioneered by Harkrider (1964). Non-uniform fault slip may be simulated by summing weighted point sources distributed along the fault plane to construct realistic synthetic seismograms. Recent inversion studies based on matching these synthetics to observations such as Hartzell and Heaton (1983), Archuleta (1984), and Olson and Apsel (1982) have provided amazing detail on the complex faulting process for the Imperial Valley 1979 earthquake. Unfortunately, most geologic structures in the vicinity of earthquakes are at least as complicated as displayed in Figure 1b. Separating propagational effects from complex faulting becomes much more difficult in these situations.

In this paper we address the construction of synthetics along the surface for 2-D structures such as displayed in Figure 1b. We assume that the model remains constant into and out of the plane of the paper along with line sources through each element. We design the line-source characteristics to mimic the vertical radiation pattern appropriate for double-couples where the SH and P-SV field remain decoupled along paths to the

receivers. Our main objective is to derive these line source excitation functions.

In a companion paper, Vidale and Helmberger (1987a) of this issue, we discuss numerical strong ground motion calculations for a 2-D structural model through the Los Angeles region and compare these results with observations from the San Fernando earthquake.

Theory

The approach follows closely the usual shear dislocation theory developed for treating plane layered models, where the wave-field is separated into vertical and horizontal functions. This separation is essential for expressing the field in terms of SH and P-SV systems and provides the key to our approach. A particularly convenient form of the solution is given by Helmberger and Harkrider (1977) in terms of Laplace-transformed displacements along the vertical, tangential, and radial directions,

$$\begin{aligned}\hat{W} &= \frac{\partial \hat{\phi}}{\partial z} + sp\hat{\Omega} \\ \hat{V} &= \frac{1}{r} \frac{\partial \hat{\phi}}{\partial \theta} - \frac{1}{spr} \frac{\partial^2 \hat{\Omega}}{\partial z \partial \theta} - \frac{\partial \hat{\chi}}{\partial r} \\ \hat{Q} &= \frac{\partial \hat{\phi}}{\partial r} - \frac{1}{sp} \frac{\partial^2 \hat{\Omega}}{\partial r \partial z} + \frac{1}{r} \frac{\partial \hat{\chi}}{\partial \theta}\end{aligned}\tag{1}$$

where z , r and θ are the vertical, radial, polar angle coordinates, respectively. The P wave potential (ϕ), the SV wave potential (Ω), and the SH wave potential (χ) for a strike-slip orientation are:

$$\hat{\phi} = \frac{M_0}{4\pi\rho} \frac{2}{\pi} \operatorname{Im} \int_c^{i\infty + c} (-p^2) \frac{p}{\eta_\alpha} \exp(-s\eta_\alpha |z-h|) K_2(spr) dp \cdot \sin 2\theta\tag{2}$$

$$\hat{\Omega} = \frac{M_0}{4\pi\rho} \frac{2}{\pi} \operatorname{Im} \int_c^{i\infty + c} (-\epsilon p \eta_\beta) \frac{p}{\eta_\beta} \exp(-s\eta_\beta |z-h|) K_2(spr) dp \cdot \sin 2\theta\tag{3}$$

(4)

$$\hat{\chi} = \frac{M_0}{4\pi\rho} \frac{2}{\pi} \operatorname{Im} \int_c^{i\infty + c} \left(\frac{1}{\beta^2} \right) \frac{p}{\eta_\beta} \exp(-s\eta_\beta |z-h|) K_2(spr) dp \cdot \cos 2\theta$$

where

s = Laplace transform variable

p = ray parameter

$\eta_v = (1/v^2 - p^2)^{1/2}$

h = depth of source

α = compressional velocity

β = shear velocity

ρ = density

M_0 = seismic moment

c is a small constant that offsets path of integration from the imaginary axis, and

where $\epsilon = \begin{cases} +1 & z > h \\ -1 & z < h \end{cases}$, and

θ = strike from the end of the fault plane.

The geometry displaying the orientation of the fault in the cylindrical coordinate system is given in Figure 2. Note that a strike-slip event is defined by $\lambda = 0^\circ$ and $\delta = 90^\circ$. Integrals of the type given in equations (2) through (4) can be transformed back into the time domain by applying the Cagniard-de Hoop technique as discussed by Helmberger and Harkrider (1977). An asymptotic solution and one useful for our purpose can be obtained by expanding the modified Bessel functions

$$K_2(spr) = \sqrt{\frac{\pi}{2} spr} e^{-spr} \left[1 + \frac{15}{8spr} + \dots \right] \quad (5)$$

substituting the resulting power series in potentials back into the displacements, expression (1), and expand again in powers of $(1/s)$. The first term of such an expansion has the following form:

$$W = \frac{M_o}{4\pi\rho} \frac{d}{dt} \left[\dot{D}(t) * (w_\alpha + w_\beta) \right] \sin 2\theta \quad (6)$$

$$V = \frac{M_o}{4\pi\rho} \frac{d}{dt} \left[\dot{D}(t) * v_\beta \right] \cos 2\theta \quad (7)$$

$$Q = \frac{M_o}{4\pi\rho} \frac{d}{dt} \left[\dot{D}(t) * (q_\alpha + q_\beta) \right] \sin 2\theta \quad (8)$$

where

$$w_\alpha = \sqrt{\frac{2}{r}} \frac{1}{\pi} \left[\frac{1}{\sqrt{t}} * \text{Im} \left\{ \frac{\sqrt{p}}{\eta_\alpha} (-p^2) (-\epsilon \eta_\alpha) \frac{dp}{dt} \right\} \right] \quad (9)$$

$$w_\beta = \sqrt{\frac{2}{r}} \frac{1}{\pi} \left[\frac{1}{\sqrt{t}} * \text{Im} \left\{ \frac{\sqrt{p}}{\eta_\beta} (-\epsilon p \eta_\beta) (p) \frac{dp}{dt} \right\} \right] \quad (10)$$

$$v_\beta = \sqrt{\frac{2}{r}} \frac{1}{\pi} \left[\frac{1}{\sqrt{t}} * \text{Im} \left\{ \frac{\sqrt{p}}{\eta_\beta} \left(\frac{1}{\beta^2} \right) (p) \frac{dp}{dt} \right\} \right] \quad (11)$$

$$q_\alpha = \sqrt{\frac{2}{r}} \frac{1}{\pi} \left[\frac{1}{\sqrt{t}} * \text{Im} \left\{ \frac{\sqrt{p}}{\eta_\alpha} (-p^2) p \frac{dp}{dt} \right\} \right] \quad (12)$$

$$q_\beta = \sqrt{\frac{2}{r}} \frac{1}{\pi} \left[\frac{1}{\sqrt{t}} * \text{Im} \left\{ \frac{\sqrt{p}}{\eta_\beta} (-\epsilon p \eta_\beta) (-\epsilon \eta_\beta) \frac{dp}{dt} \right\} \right] \quad (13)$$

This is a first term asymptotic expansion similar to the expansion used for explosive sources, see Helmberger (1968). The approximation is accurate for $spr \gg 1$, which means it is most accurate for high frequency, large range, and non-vertical take-off angle. The two arrivals in the w_j and q_j cases are the P-wave and SV-wave. Note that the first term becomes uncouples in that V depends only on χ ; and W and Q only on ϕ and Ω , so the SH solution separates from the P-SV solution in this asymptotic form.

Suppose we now consider the field variable defined by

$$\Psi = \sqrt{\frac{2}{r}} \frac{1}{\pi} \left[\frac{1}{\sqrt{t}} * \text{Im} \left\{ \frac{\sqrt{p}}{\eta_v} \frac{dp}{dt} \right\} \right] \quad (14)$$

which has a simple interpretation following the Cagniard-de Hoop technique, where

$$p = \frac{r}{R^2}t + i \left(t^2 - \frac{R^2}{V^2} \right)^{1/2} \frac{|z|}{R^2} \quad (15)$$

$$\eta_V = \frac{|z|}{R^2}t - i \left(t^2 - \frac{R^2}{V^2} \right)^{1/2} \frac{r}{R^2}$$

and

$$\frac{dp}{dt} = i \eta_V H(t - R/V) / \left(t^2 - \frac{R^2}{V^2} \right)^{1/2},$$

where V can be either α or β . Substituting these equations into (14) yields

$$\Psi \approx \frac{1}{R} H(t - R/V)$$

where $R = (r^2 + z^2)^{1/2}$ and the imaginary parts of p and η_V has been neglected, namely

$$\text{Re}(p) = \sin\phi/V \quad \text{and} \quad \text{Re}(\eta_V) = \cos\psi/V,$$

The (p) becomes the well-known ray parameter and (η_V) the vertical slowness. The extra (p^2) occurring in W_α becomes the vertical radiation pattern and η_α the vertical component of the P wave. The (ϵ) expresses the jump in polarity across the origin, see Figure 3a. This series of simplifications are called the first motion approximations and have proven quite useful in modeling seismograms at teleseismic distances, see Langston and Helmberger (1975).

A more accurate solution at local distances can be obtained by solving expressions (9) through (13) numerically and substituting into (6), (7) and (8), which yields the first term of the asymptotic displacement as discussed. The results for a wholespace model are displayed in Figure 4. Higher order terms, $(1/s)^n$, are included along with the exact Cagniard-de Hoop solution on the bottom, see Helmberger and Harkrider (1977). Note the slight up-turn for the 12 term solution at the end of the radial motion. The solution rises rapidly for longer times and these asymptotics suffer the usual blow-up at large

times characteristic of such series. Also, note that the so-called near-field terms are missing along the top row. The near-field contributions are particularly easy to see by noting that the first term of the tangential motion, V of expression (1), depends on the azimuthal change of the P-wave. A schematic of the horizontal P-wave pattern is displayed in Figure 3b indicating the compressional field peaked at $\theta = 45^\circ$. Since the material at a receiver, as in Figure 4, behaves elastically before the arrival of the shear wave it relaxes by moving counter-clockwise for angles less than 45° . Similar drifts occurs for the other two components between the P and S wave arrivals where each time the material moves to relax from the P-wave loading. This drifting should end upon arrival of the shear-wave which is well known from the exact solution. Unfortunately, the asymptotics continue to drift which can cause severe problems at long periods, and should be avoided for source durations longer than a significant fraction of $(t_\beta - t_\alpha)$, the timing separation between the P and S waves.

Expressions (6) through (13) have produced the goal of separating the motions into vertical and horizontal functions but we still must require these expressions be solutions of the 2-D wave equation. This requires removing the \sqrt{p} dependence.

One approach is to expand \sqrt{p} in a power series about some fixed direction, p_0 ;

$$\sqrt{p} = \sqrt{p_0} = \frac{1}{2} \frac{1}{\sqrt{p_0}} (p - p_0) = \frac{\sqrt{p_0}}{2} + \frac{p}{2\sqrt{p_0}}$$

and carry the second factor as a correction term. The first term has shown to be adequate in, Vidale et al (1985) where we approximated

$$\sqrt{\frac{vp}{r}} = \frac{1}{\sqrt{R}}$$

although we must avoid $p_0 = 0$ or $r = 0$. The effective vertical radiation patterns then become the real-part operator, $\text{Re} ()$, of a product of complex p 's and η 's as defined in (15). For instance, from (9) we obtain

$$\Psi^1 \equiv \text{Im} \left(\frac{1}{\eta_\alpha} \frac{dp}{dt} (-p^2) (-\epsilon \eta_\alpha) \right) = \text{Re} (\epsilon p^2 \eta_\alpha) H(t - R/\alpha) \left(t^2 - \frac{R^2}{\alpha^2} \right)^{1/2}$$

and after some complex algebra

$$\text{Re}(\epsilon p^2 \eta_\alpha) = \frac{-\epsilon |z| t^3}{R^6} \left[\left[z^2 - 3r^2 + \frac{R^2}{t^2 \alpha^2} (2r^2 - z^2) \right] \right]$$

Thus, the vertical displacement for a in-coming p wave from a strike-slip source becomes

$$W_\alpha = \sqrt{\frac{2}{R\alpha}} \frac{1}{\pi} \left[\frac{1}{\sqrt{t}} * \Psi^1 \right]$$

where (Ψ^1) solves the 2-D wave equation. Note that for times near the wave-front $t = R/\alpha$ and the function

$$\text{Re}(\epsilon p^2 \eta_\alpha) = \frac{\cos \phi \sin^2 \phi \epsilon}{\alpha^3}$$

which is the result obtained earlier from the first-motion approximation. To produce transparent source box conditions for the finite-difference requires a complete solution for all times and (Ψ^1) serves this role. In short, the complex near-field terms which change their shape with time is required if we want to send out a simple $\sin^2 \theta$ pattern at larger distances. Similar expressions can be derived from equations (10) through (13) and explicit 2-D excitation functions determined by evaluating the $\text{Re}(\)$ operators. The grid mechanics along with the other fundamental fault orientations are given in Vidale and Helmberger (1987b). We will include these results here for completeness. Let

$$\Gamma_\gamma = \sqrt{\frac{2}{\gamma}} \left(\frac{M_0}{4\pi\rho_0} \right) \frac{1}{\pi} (M_0 \times 10^{-20}) \text{ and } T_\gamma = \frac{R^2}{t^2 \gamma^2}$$

where $\gamma = \alpha$ or β expressed in km/sec, $R = \text{km}$, and M_0 in ergs. We will assume that $D(t) = \delta(t)$, (slightly smoothed as discussed in Vidale et al (1985), or that the slip function across the fault corresponds to a Heavside step function. Also, we define superscripts 1, 2 and 3 to refer to strike-slip, dip-slip and 45° dip-slip fundamental fault orientations. With these definitions the analytic source expressions used in defining the displacements in the grid become:

(Strike=slip)

$$W_{\alpha}^1 = -z (z^2 - 3r^2 + T_{\alpha} (2r^2 - z^2)) \Psi_{\alpha}$$

$$W_{\beta}^1 = -z (3r^2 - z^2 + T_{\beta} (z^2 - 2r^2)) \Psi_{\beta}$$

$$V_{\beta}^1 = \frac{r}{R^2} \frac{1}{t^2 \beta^2} \Psi_{\beta}$$

$$Q_{\alpha}^1 = r (r^2 - 3z^2 + 3T_{\alpha} z^2) \Psi_{\alpha}$$

$$Q_{\beta}^1 = r (3z^2 - r^2 + T_{\beta} (r^2 - 2z^2)) \Psi_{\beta}$$

(Dip-slip)

$$W_{\alpha}^2 = -r (2r^2 - 6z^2 + T_{\alpha} (4z^2 - 2r^2)) \Psi_{\alpha}$$

$$W_{\beta}^2 = -r (6z^2 - 2r^2 + T_{\beta} (r^2 - 5z^2)) \Psi_{\beta}$$

$$V_{\beta}^2 = \frac{z}{R^2} \frac{1}{t^2 \beta^2} \Psi_{\beta}$$

$$Q_{\alpha}^2 = z (6r^2 - 2z^2 + T_{\alpha} (2z^2 - 4r^2)) \Psi_{\alpha}$$

$$Q_{\beta}^2 = z (2z^2 - 6r^2 + T_{\beta} (5r^2 - z^2)) \Psi_{\beta}$$

(45° dip-slip)

$$W_{\alpha}^3 = -z (9r^2 - 3z^2 + T_{\alpha} (z^2 - 8r^2)) \Psi_{\alpha}$$

$$W_{\beta}^3 = -z (3z^2 - 9r^2 + T_{\beta} (6r^2 - 3z^2)) \Psi_{\beta}$$

$$Q_{\alpha}^3 = r (9z^2 - 3r^2 + T_{\alpha} (2r^2 - 7z^2)) \Psi_{\alpha}$$

$$Q_{\beta}^3 = r (3r^2 - 9z^2 + T_{\beta} (6z^2 - 3r^2)) \Psi_{\beta}$$

These expressions and functional form are compatible with cartesian coordinates with the horizontal coordinate, x , replacing r as discussed by Helmberger (1974). Thus,

the above expressions can be used to define the desired line source excitation, see Vidale and Helmberger (1987b) for the details of source loading.

The whole-space FD solutions for the P-SV system are displayed in Figure 5 in the form of divergence and curl. Note that the divergence is nonzero where there is compressional wave energy and the curl is nonzero for shear wave energy. The far-field radiation patterns are the expected ones. For example, in the strike-slip case the outgoing P-wave has the classic two-lobe pattern while the SV-wave has a 4-lobed pattern. The complex near-field pattern can be seen in the inner clover-leaf followed by a 12-lobed pattern at the source box boundary. Note that this complex pattern changes with time but is required to produce the proper far-field behavior as discussed earlier. The corresponding patterns for the tangential displacement fields for the strike-slip and dip-slip cases is given in Figure 6. These solutions are considerably simpler. Note that this FD excitation is appropriate for a homogeneous region which was assumed for convenience. However, with the help of generalized-ray theory we could load this source box in a layered structure if desired.

After the energy propagates across the structural model to the receiver, as shown in Figure 1b, we extract the vertical, radial, and transverse motions from the FD code indicated by the symbols \tilde{W} , \tilde{V} , \tilde{Q} for each of the fundamental orientations. Finally, the point source synthetic seismogram is constructed at the observation point by evaluating

$$\begin{aligned} W_P &= \frac{1}{\sqrt{R}} \frac{d}{dt} \left[\frac{1}{\sqrt{t}} * \left(A_1 \tilde{W}^1 + A_2 \tilde{W}^2 + A_3 \tilde{W}^3 \right) \right] \\ V_P &= \frac{1}{\sqrt{R}} \frac{d}{dt} \left[\frac{1}{\sqrt{t}} * \left(A_4 \tilde{V}^1 + A_5 \tilde{V}^2 \right) \right] \\ Q_P &= \frac{1}{\sqrt{R}} \frac{d}{dt} \left[\frac{1}{\sqrt{t}} * \left(A_1 \tilde{Q}^1 + A_2 \tilde{Q}^2 + A_3 \tilde{Q}^3 \right) \right] \end{aligned}$$

where the azimuthal radiation patterns are defined by

$$A_1 = \sin 2 \theta \cos \lambda \sin \delta + \frac{1}{2} \cos 2 \theta \sin \lambda \sin 2 \delta ,$$

$$A_2 = \cos \theta \cos \lambda \cos \delta - \sin \theta \sin \lambda \cos 2 \delta ,$$

$$A_3 = \frac{1}{2} \sin \lambda \sin 2 \delta ,$$

$$A_4 = \cos 2 \theta \cos \lambda \sin \delta - \frac{1}{2} \sin 2 \theta \sin \lambda \sin 2 \delta ,$$

$$A_5 = - \sin \theta \cos \lambda \cos \delta - \cos \theta \sin \lambda \cos 2 \delta ,$$

where θ is the strike from the end of the fault plane, λ the rake angle and δ the dip angle, as shown in Figure 2. The same definitions have been used in previous source discussions, see Langston and Helmberger (1975).

Conclusion

A procedure for constructing synthetic seismograms appropriate for earthquake sources using 2-D FD codes is discussed. It is based on breaking down the 3-D motion field produced by shear dislocations into SH and P-SV systems which can be solved independently applying the 2-D wave equations. Note that the line sources must be aligned perpendicular to the structure such that no SH-SV mixing is allowed as the motion propagates through the model. Line source SH and P-SV excitation functions are derived using Cagniard-de Hoop theory for the three principal faults which allows an arbitrarily orientated fault to be simulated by linear summation. Numerical tests of this new technique against analytical codes show good agreement, for example see Figure 7 and Vidale and Helmberger (1987b).

The main disadvantage of this approach is the computational expense in running the finite-difference routines and the banded-limited nature of the results. The latter limitations are caused by grid size constraints which controls the highest frequency allowed and by the asymptotic approximations at the lowest frequency. The main advantage of this technique over other analytical methods is that it is unique in allowing

the seismic investigation of complex models such as cross-sections through basins and ridges. The usefulness of this scheme is illustrated in Vidale and Helmberger (1987a) in this issue.

Acknowledgements

We thank Richard Stead, Heidi Houston and Gladys Engen for their reviews and Robert Clayton for his efforts in developing the original finite-difference code. This work was supported by the Geophysical Sciences Division of the Air Force Geophysics Laboratory under Contract No. F19628-85-K-0017 and monitored by the Defense Advanced Research Projects Agency. Contribution number 4458, Division of Geological and Planetary Sciences, California Institute of Technology, Pasadena, CA., 91125.

References

- Archuleta, R. (1984). A faulting model for the 1979 Imperial Valley, California, earthquake. *J. Geophys. Res.*, **89**, 4559-4585.
- Harkrider, D. (1964). Surface waves in multilayered elastic media, I. Rayleigh and Loves waves from buried sources in a multi-layered elastic half-space. *Seismol. Soc. Am., Bull.*, **54**, 627-679.
- Hartzell, S., and T. Heaton (1983). Inversion of strong ground motion and teleseismic waveform data for the fault rupture history of the 1979 Imperial Valley, California earthquake. *Seismol. Soc. Am., Bull.*, **73**, 1553-1583.
- Helmberger, D. (1968). The crust-mantle transition in the Bering Sea. *Seismol. Soc. Am., Bull.*, **58**, 179-214.
- Helmberger, D. (1974). Generalized ray theory for shear dislocations. *Seismol. Soc. Am., Bull.*, **64**, 45-64.
- Helmberger, D. and D. Harkrider (1977). Modeling earthquakes with generalized ray theory: Modern problems in elastic wave propagation. IUTAM Symposium, John Wiley & Sons, New York, 479-518.
- Langston, C. A. and D. V. Helmberger (1975). A procedure for modeling shallow dislocation sources. *Geophys. J., R. Astron. Soc.*, **42**, 117-130.
- Olson, A. H. and R. Apsel (1982). Finite faults and inverse theory with applications to the 1979 Imperial Valley earthquake, *Seismol. Soc. Am., Bull.*, **72**, 1969-2002.
- Vidale, J. E., D. V. Helmberger, and R. W. Clayton (1985). Finite-difference seismograms for SH waves. *Seismol. Soc. Am., Bull.*, **75**, 1765-1782.
- Vidale, J. E. and D. V. Helmberger (1987a). Elastic finite-difference modeling of the 1971 San Fernando, California earthquake. *Seismol. Soc. Am., Bull.*, submitted.
- Vidale, J. E. and D. V. Helmberger (1987b). Path effects in strong motion seismology, seismic strong motion synthetics, in *Methods of Computational Physics*, ed. Bruce Bolt.

Figure Captions

Figure 1: Schematic diagram displaying energy paths for a) flat-layered model versus b) laterally varying structure. The model is two-dimensional or constant properties into and out of the plane of the paper.

Figure 2: Description of conventions for mechanism and orientation.

Figure 3: Comparison of the three components of displacement for a wholespace with a strike-slip source. The top four rows contain the asymptotic summation with 1, 2, 4, and 12 terms. The full solution is displayed on the bottom. The source depth is 8 km and the range is 16 km. Model parameters are $\alpha = 6.2$ km/sec, $\beta = 3.5$ km/sec, and $\rho = 2.7$ g/cm³.

Figure 4: The upper diagram displays the vertical radiation field appropriate for a strike-slip excited P-wave with a $\sin^2\phi$ pattern. The lower panel displays the azimuthal field showing the strong P-wave loading near 45°. Between the times t_a and t_b the material in the fourth quadrant flows away from the maximum compression, namely clockwise for $\theta > 45^\circ$ and counter clockwise for $\theta < 45^\circ$.

Figure 5: P-SV vertical radiation patterns. The divergence and curl fields due to strike-slip, dip-slip, and 45° dip-slip sources are shown after 150 timesteps. The plots have a grey background, where positive is shown in black and negative in white.

Figure 6: SH vertical radiation patterns. The displacement field due to strike-slip, and dip-slip sources are shown after 125 and 250 timesteps. The plots for the earthquakes have a grey background, where positive displacements are shown in black and negative in white.

Figure 7: Comparison of FD and GRT seismograms for the ranges 32, 48, and 64 km for the strike-slip, dip-slip, and 45° dip-slip mechanisms. The far-field source time functions, $D(t)$, is specified by a trapezoidal shape with equal δt_j 's of 0.2 sec. The parameters for the layers are given in Table 1 with a source depth of 8 km. Amplitudes may be scaled to moment.

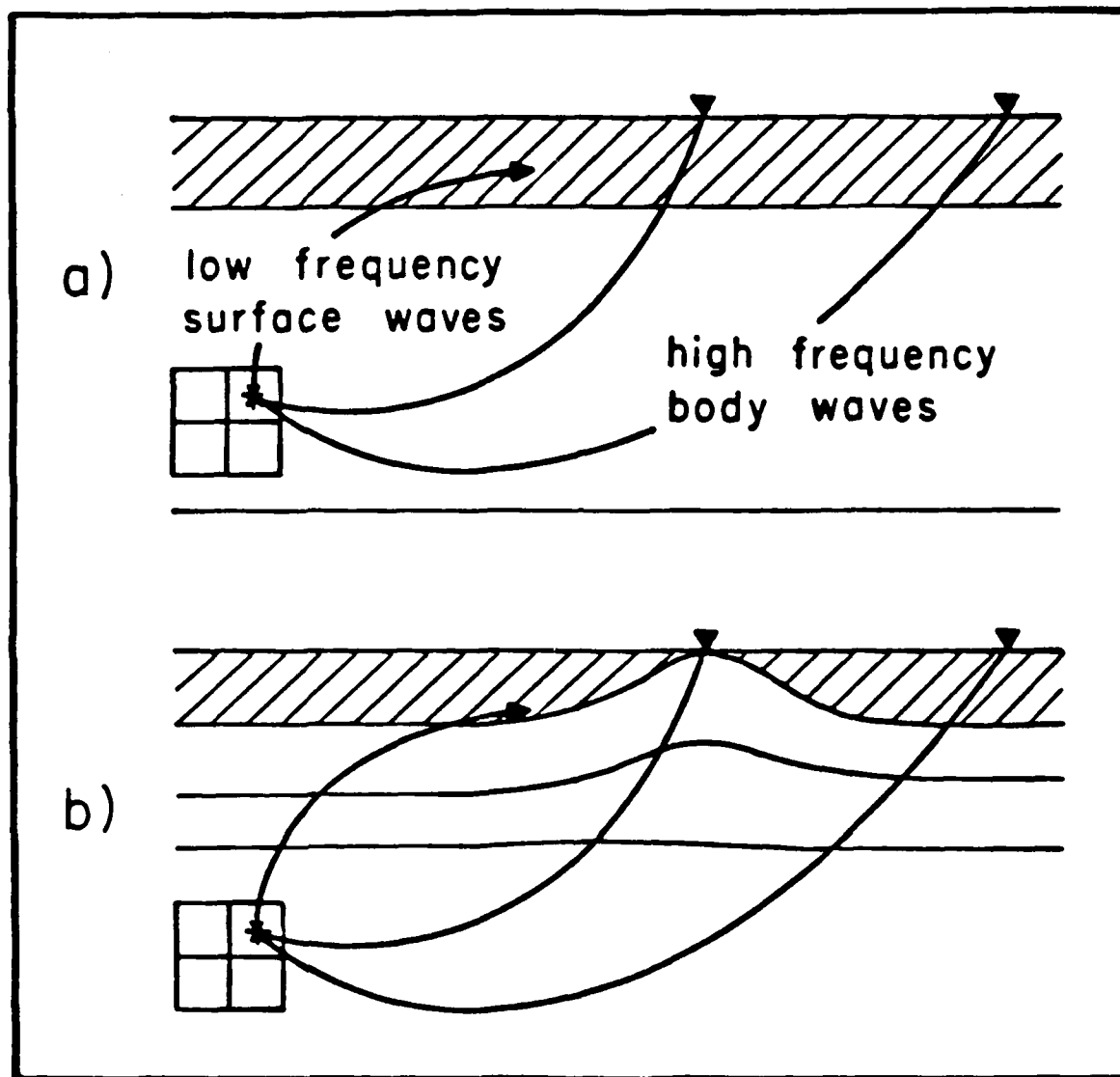


Figure 1: Schematic diagram displaying energy paths for a) flat-layered model versus b) laterally varying structure. The model is two-dimensional or constant properties into and out of the plane of the paper.

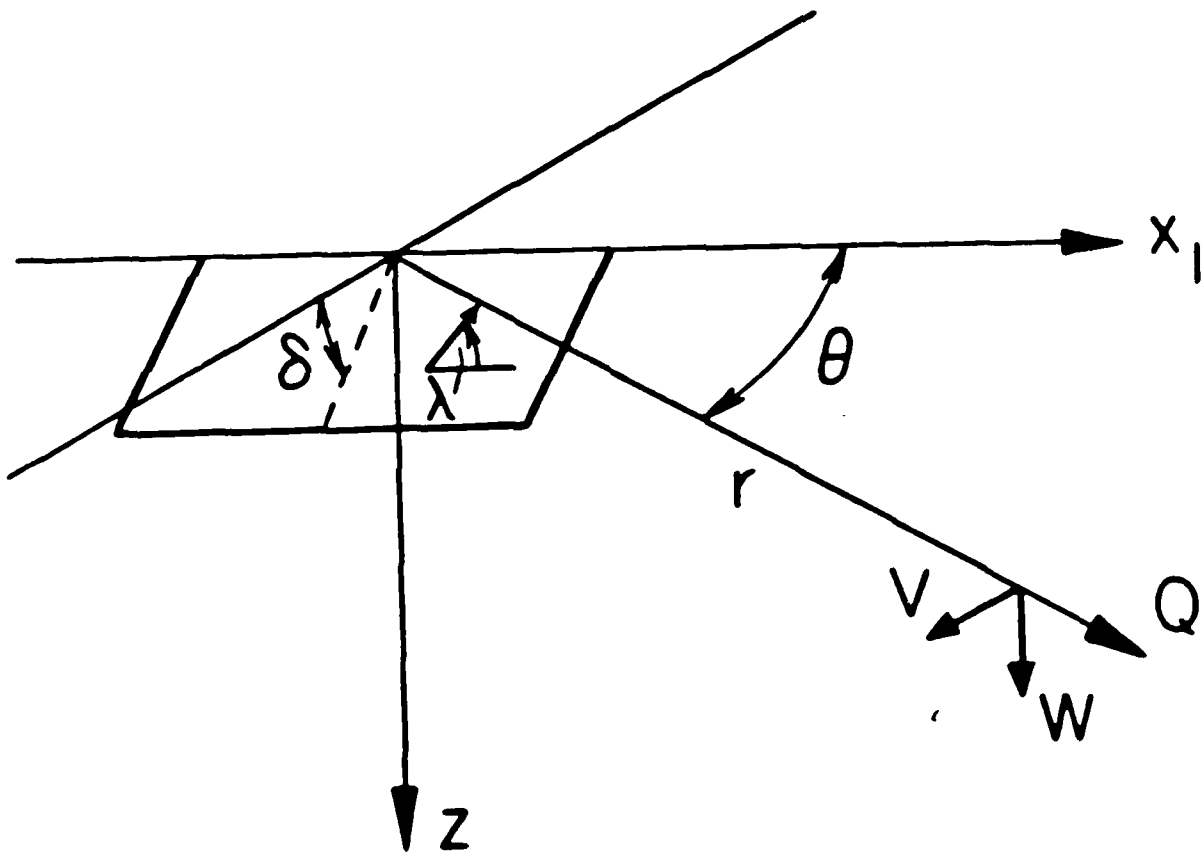
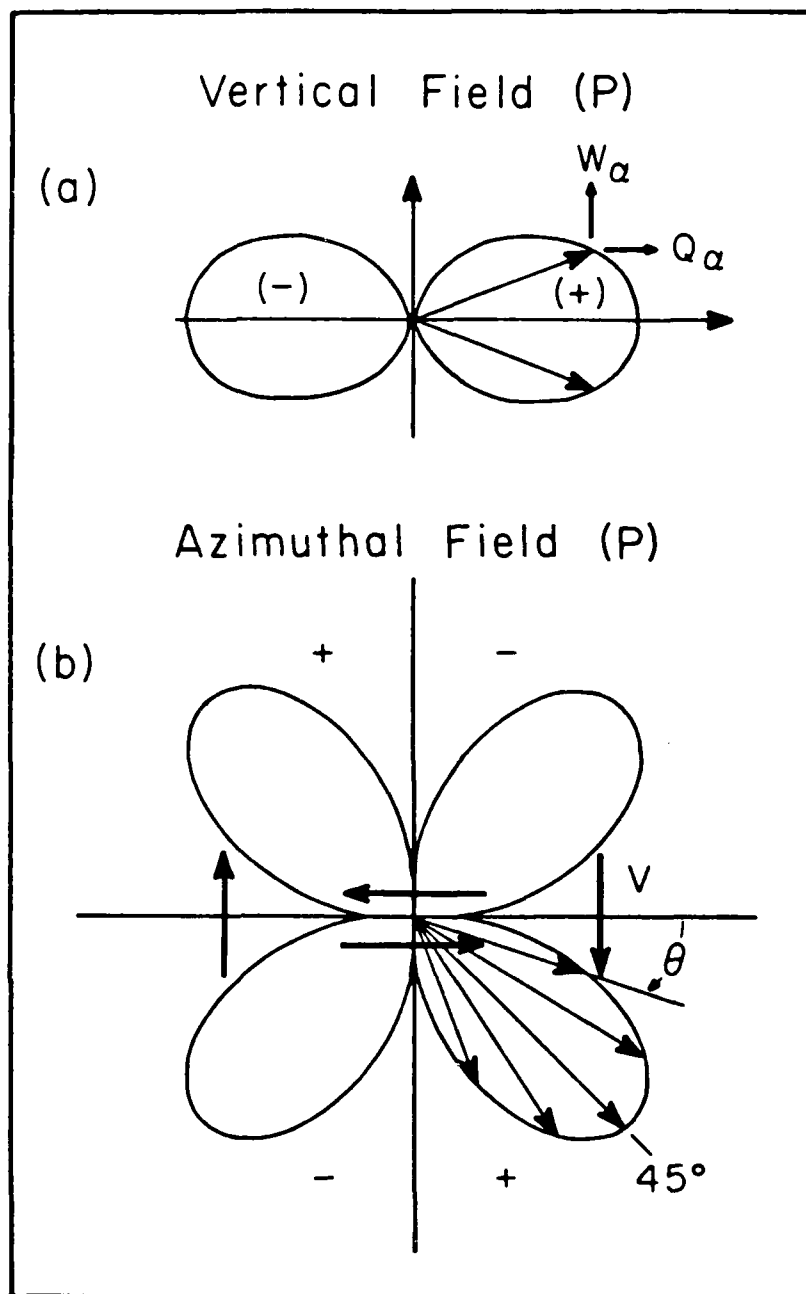


Figure 2: Description of conventions for mechanism and orientation.



3.

Figure 3: The upper diagram displays the vertical radiation field appropriate for a strike-slip excited P-wave with a $\sin^2\phi$ pattern. The lower panel displays the azimuthal field showing the strong P-wave loading near 45° . Between the times t_a and t_b , the material in the fourth quadrant flows away from the maximum compression, namely clockwise for $\theta > 45^\circ$ and counter clockwise for $\theta < 45^\circ$.

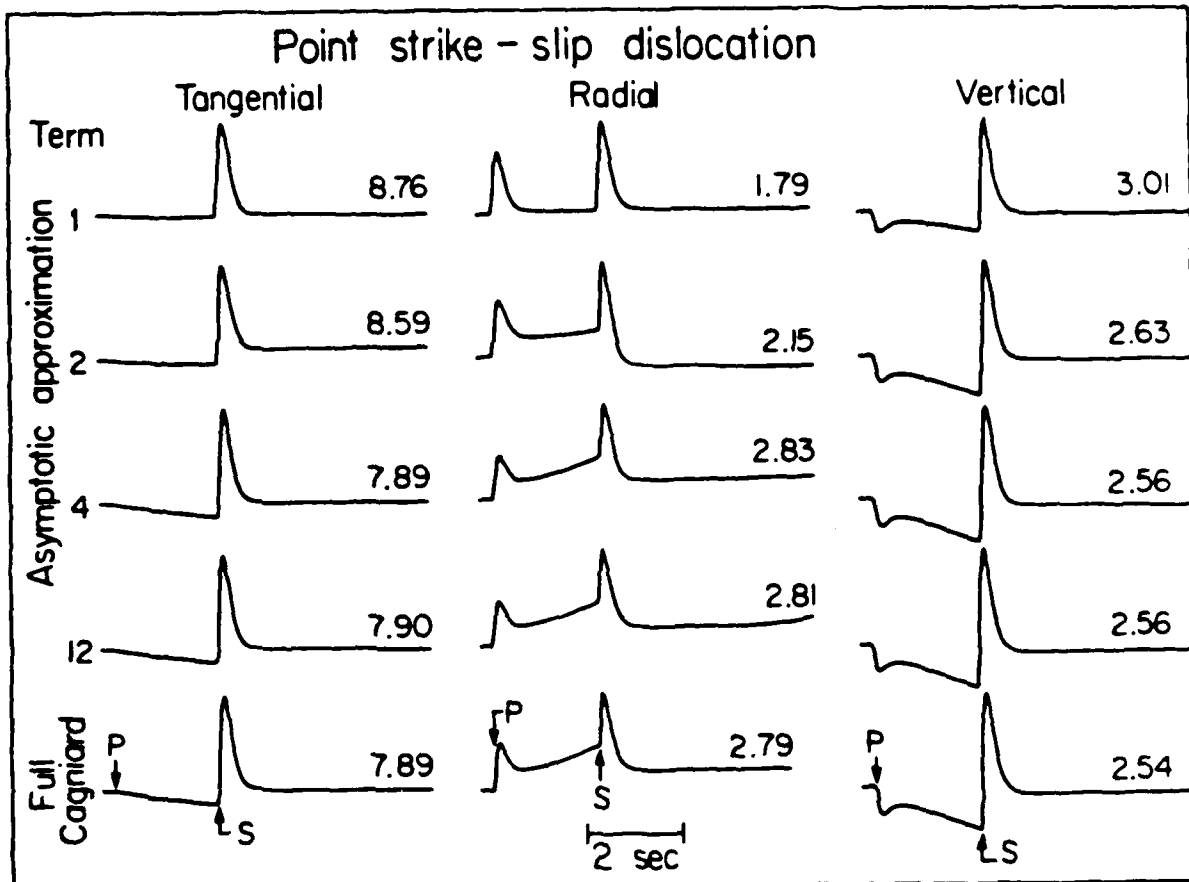


Figure 4: Comparison of the three components of displacement for a wholespace with a strike-slip source. The top four rows contain the asymptotic symmmation with 1, 2, 4, and 12 terms. The full solution is displayed on the bottom. The source depth is 8 km and the range is 16 km. Model parameters are $\alpha = 6.2$ km/sec, $\beta = 3.5$ km/sec, and $\rho = 2.7$ g/cm³.

P-SV VERTICAL RADIATION PATTERNS

Divergence

Curl

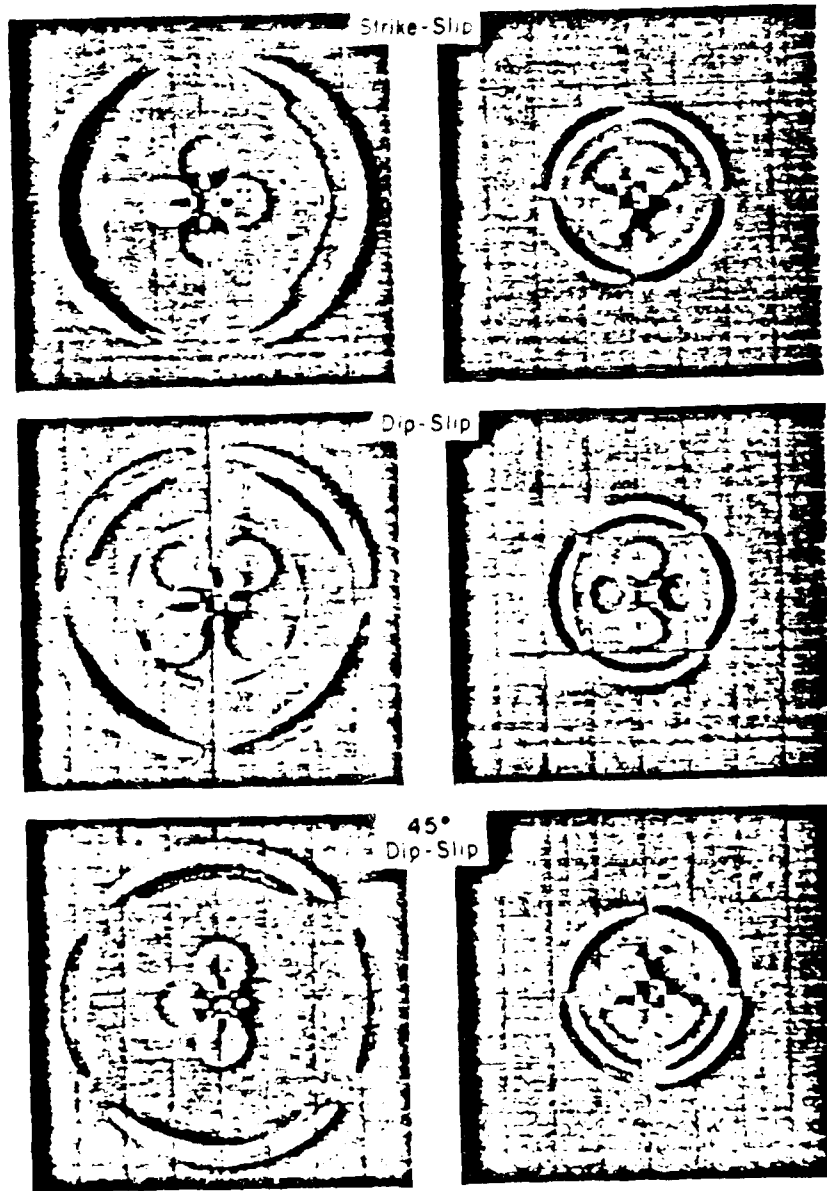


Figure 5: P-SV vertical radiation patterns. The divergence and curl fields due to strike-slip, dip-slip, and 45° dip-slip sources are shown after 150 timesteps. The plots have a grey background, where positive is shown in black and negative in white.

SH VERTICAL RADIATION PATTERNS

$t = 125$ time steps

$t = 250$ time steps

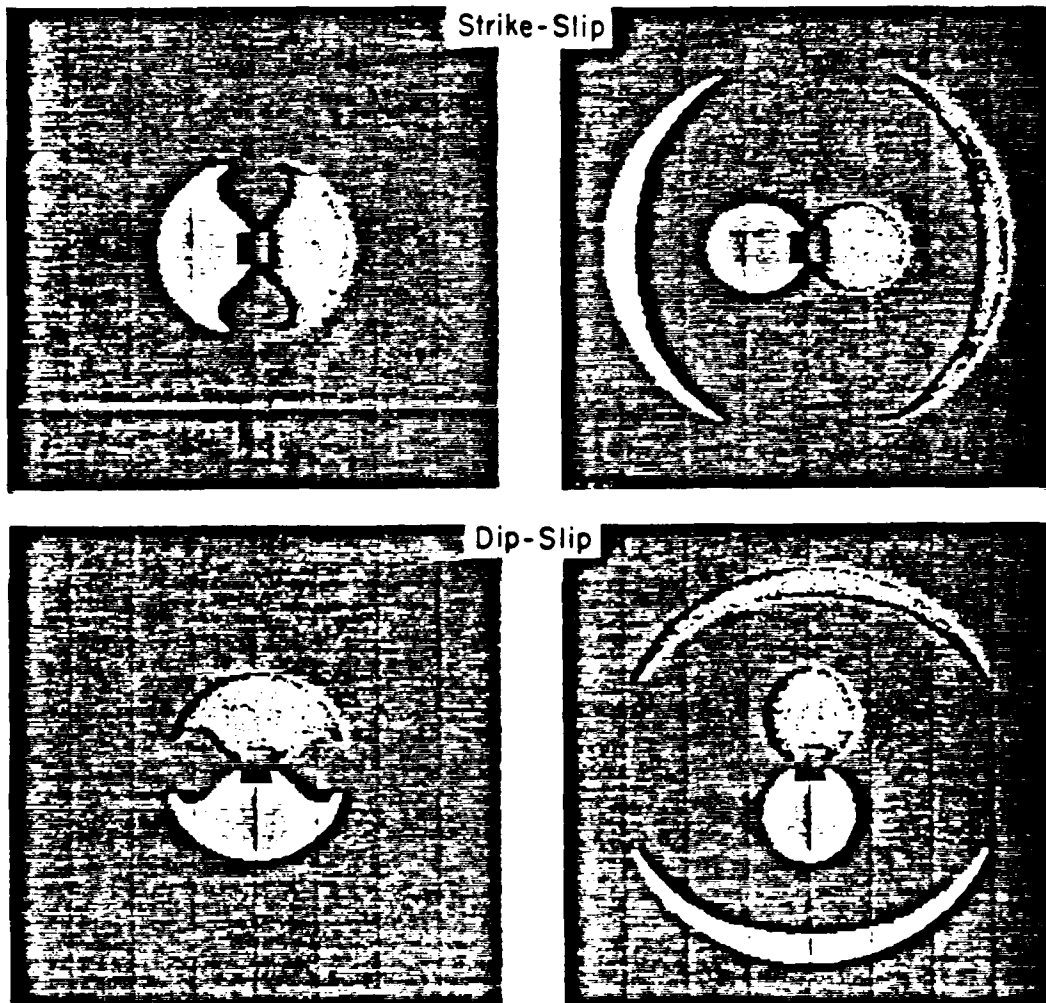


Figure 6: SH vertical radiation patterns. The displacement fields due to strike-slip and dip-slip sources are shown after 125 and 250 timesteps. The plots have a grey background, where positive displacements are shown in black and negative in white.

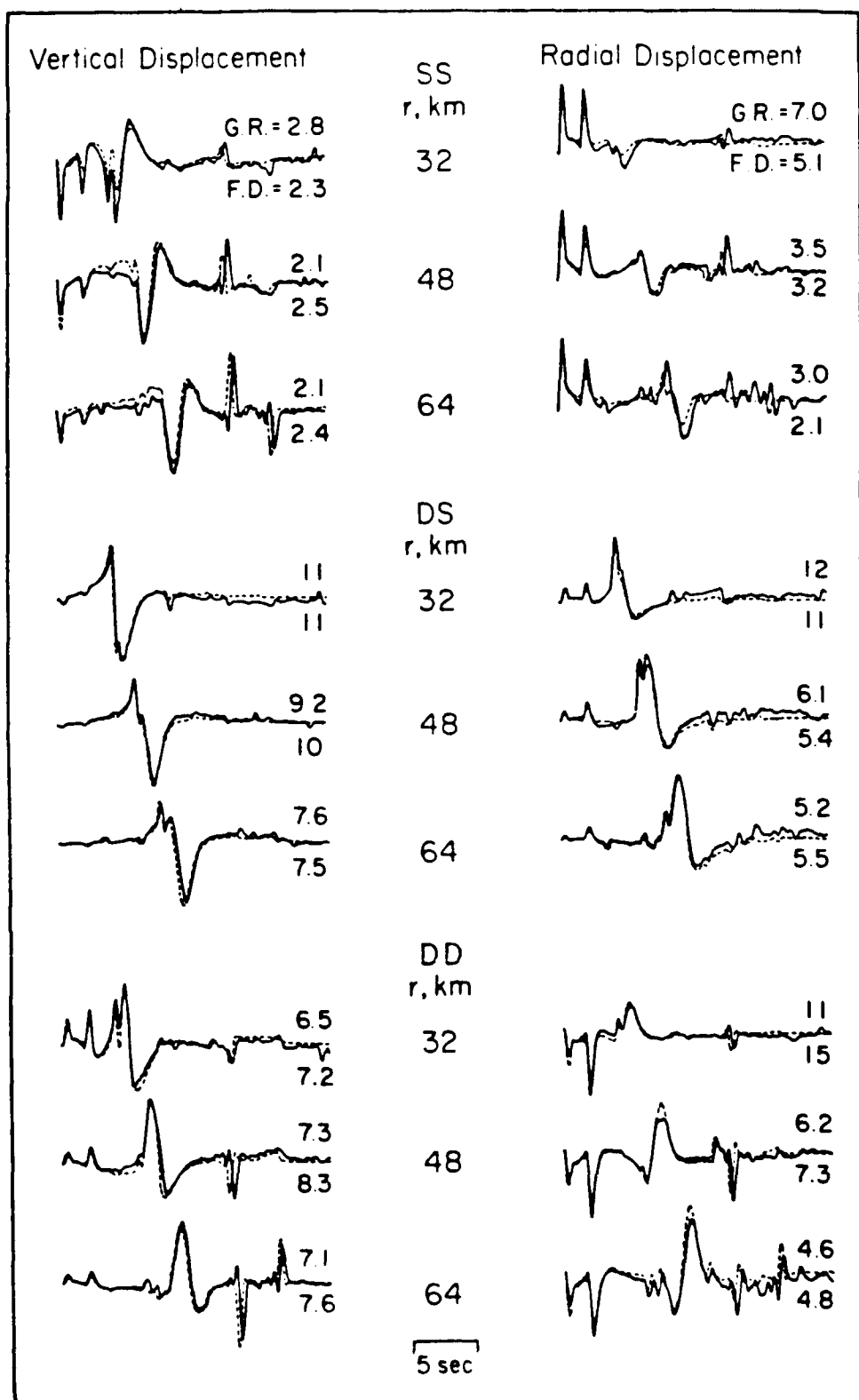


Figure 7: Comparison of FD and GRT seismograms for the ranges 32, 48, and 64 km for the strike-slip, dip-slip, and 45° dip-slip mechanisms. The far-field source time function, $D(t)$, is specified by a trapezoidal shape with equal δt_i 's of 0.2 sec. The model used is layer over a halfspace; the layer is 32 km thick with P- and S-wave velocities of 6.5 and 3.5 km/sec and a density of 2.7 g/cc. The halfspace has P- and S-wave velocities of 8.2 and 4.5 km/sec, and a density of 3.4 g/cc.

Numerical Studies of Propagation of L_g Waves across Ocean Continent Boundaries Using the Representation Theorem

Thesis by
Janice Regan

Table of Contents

Acknowledgements	-24-
Abstract	-25-
 Chapter 2: Application of Modal Propagator Matrix to Finite Element Coupling to Investigations of L_g Propagation across Ocean Continent Boundaries	
1. Introduction	-27-
2. Designing FE grids and sampling FE solutions.	-28-
3. Understanding the accuracy and efficiency of the absorbing BC	-39-
4. Changes to L_g wavetrains on passage through a forward transition region	-57-
5. Changes to L_g wavetrains on passage through a reverse transition region ..	-73-
6. The dependence of changes to L_g wavetrains passing through forward transition regions on transition length	-88-
7. The dependence of changes to L_g wavetrains passing through reverse transition regions on transition length	-98-
8. Conclusions	-103-

Acknowledgements

Many thanks to my thesis advisor, David G. Harkrider, for guidance, support, and encouragement. Thanks, also to the students, faculty, and staff of the Seismo. Lab. for their friendship and encouragement.

This research has been sponsored by the Defense Advanced Research Projects Agency (DOD) with technical management by the Air Force Geophysics Laboratory under Contract # F19628-85-K-0017.

Abstract

The methods for Representation Theorem (RT) coupling of finite element (FE) or finite difference calculations and Harkrider's (Harkrider 1964, 1970) propagator matrix method calculations to produce a hybrid method for propagation of SH mode sum seismograms across paths that contain regions of non plane-layered structure are explained and developed. The coupling methods explained in detail use a 2-D Cartesian FE formulation. Analogous methods for the 3-D method follow directly. Extensive tests illustrating the validity and accuracy of the implementation of these coupling methods are discussed. These hybrid techniques are developed to study the propagation of surface waves across regional transition zones or other heterogeneities that exist in part of a longer, mostly plane-layered, path. The effects of a thinning or thickening of the crustal layer on the propagation of L_g mode sum seismograms have been examined in this study. The thinning or thickening of the crustal layer is used as a simple model of ocean continent transitions. The L_g phase is of particular interest since it is used in several important applications such as mapping the extent of continental crust, magnitude determination, and discrimination between explosive and earthquake sources. The understanding of the observations that L_g wave is attenuated completely when the propagation path includes an oceanic portion of length greater than one hundred to two hundred kilometers or a region of complex crustal structure is not complete, and a clear explanation of these phenomena could have important consequences for all these types of studies. The transition model calculations done in this study show that passage through a region of thinning crustal thickness, the model for a continent to ocean transition, increases the amplitude and coda length of the L_g wave at the surface, and allows much of the modal energy

trapped in the crust, which forms the L_g phase, to escape into the subcrustal layers as body waves or other downgoing phases. The magnitude of both these effects increases as the length of the transition increases or the slope of the layer boundaries decrease. The passage of the wavefront exiting the continent to ocean transition region through the oceanic structure allows further energy to escape from the crustal layer, and produces a decrease in L_g amplitude at the surface as the length of the oceanic path increases. The amplitude decrease is maximum near the transition region and decreases with distance from it. Passage through a region of thickening crust, the model of a ocean to continent transition, causes a rapid decrease in the L_g amplitude at the surface of the crust. The energy previously trapped in the oceanic crustal layer spreads throughout the thickening crustal layer, and any amplitude which has been traveling through the subcrustal layer but has not reached depths below the base of the continental crust is transmitted back into the continental crust. The attenuation of L_g at the crustal surface along a partially oceanic path occurs in the oceanic structure and in the ocean to continent transition region. The attenuation at the surface depends in part on the escape of energy at depth through the continent to ocean transition region into the underlying half-space. The total attenuation of L_g due to propagation through a forward transition followed by a reverse transition is at most a factor of four to six. This is inadequate to explain the observed attenuation of L_g . Thus, additional effects, other than geometry must be considered to provide a complete explanation of the attenuation of L_g .

Chapter 2

Application of Modal Propagator Matrix to Finite Element Coupling to Investigation of L_g Propagation across Ocean Continent Boundaries

Introduction

In this chapter the effects of a thinning or thickening of the crustal layer on the propagation of L_g mode sum seismograms will be examined. The thinning or thickening of the crustal layer is used as a simple model of ocean to continent or continent to ocean transitions. The L_g phase is of particular interest since it is used in several important applications such as mapping the extent of continental crust, magnitude determination, and discrimination between explosive and earthquake sources. The understanding of the observations that L_g wave is attenuated completely when the propagation path includes an oceanic portion of length greater than one hundred to two hundred kilometers or a region of complex crustal structure is not complete, and a clear explanation of this phenomenon could have important consequences for all these types of studies.

The transition model calculations presented in this chapter show that passage through a region of thinning crustal thickness, the model for a continent to ocean transition, increases the amplitude and coda length of the L_g wave at the surface, and allows much of the modal energy trapped in the crust, which forms the L_g phase, to escape into the subcrustal layers as body waves or other downgoing phases. The magnitude of both these effects increases as the length of the transition increases or the slope of the layer boundaries decrease. The passage of the wavefront exiting the continent to ocean transition region through the oceanic structure allows further energy to escape from the crustal layer, and produces a decrease in L_g amplitude at the

surface as the length of the oceanic path increases. The amplitude decrease is maximum near the transition region and decreases with distance from it. Passage through a region of thickening crust, the model of a ocean to continent transition, causes a rapid decrease in the L_g amplitude at the surface of the crust. The energy previously trapped in the oceanic crustal layer spreads throughout the thickening crustal layer, and any amplitude which has been traveling through the subcrustal layer but has not reached depths below the base of the continental crust is transmitted back into the continental crust. The attenuation of L_g at the crustal surface along a partially oceanic path occurs in the oceanic structure and in the ocean to continent transition region. The attenuation at the surface depends in part on the escape of energy at depth through the continent to ocean transition region into the underlying half-space.

Designing FE Grids and Sampling FE Solutions

A study of the effects of the length of simple transition regions on the attenuation of SH type L_g mode sum seismograms passing through them has yielded some interesting results. Two classes of transition models were considered. An example of each class is illustrated in Figure 1. Calculations were performed for four individual models from each class, for a continental crustal layer over a mantle half-space, and for an ocean layer and an oceanic crustal layer over a mantle half-space. The difference between individual transition models was the length of the transition region, or the horizontal distance between points B and D shown in Figure 1. As discussed earlier, real ocean to continent type transitions occur over lengths of order one hundred kilometers. However, an upper limit on the length of the transition of one hundred kilometers was imposed by limiting FE computation time per model to approximately one cpu day. Thus, the lengths used for this investigation were a step transition (0 km), twenty five , fifty, and one hundred kilometers. In order to discuss the results of the FE calculations using these models one must first describe the models.

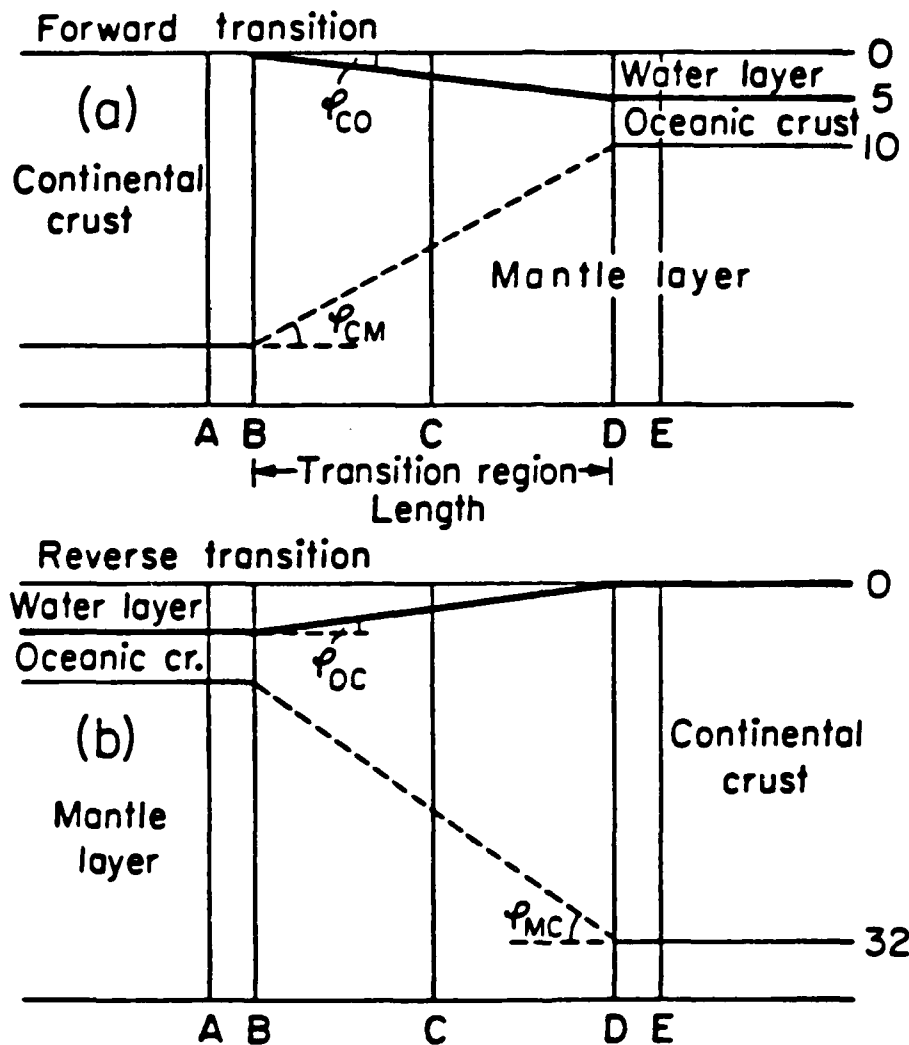


Figure 1: Explanation of terms and illustration of the model classes used to describe the behavior on passage through a transition region. The heavy line (—) between the water layer and the crustal layer is the surface. The sloping portion of this surface is the continent to ocean boundary for the forward transition model and the ocean to continent boundary for the reverse transition model. Similarly, the sloping dashed line (---) between the crust and mantle layers is the crust to mantle boundary for the forward transition and the mantle to crust boundary for the reverse case. The length of the transition is the distance from B to D, B is referred to as the beginning of the transition, D as the end of the transition, C as the center of the transition. A is 5 km from B, E is 5 km from D.

Also, the methods used to obtain and display the results of the calculations using those models must be considered.

Analysis of the effects of various transitions on the waveforms and amplitudes of L_g waves using FE techniques requires that the motions of the nodes of the FE grid be sampled so that the progress of the L_g waves across the transition can be observed. Two methods of sampling are used in this study. Complete displacement time histories are recorded for selected nodes, and the displacements of all nodes in the grid are recorded at given time intervals. The first approach produces seismograms which can be used to illustrate variations of amplitude and waveform with distance or depth, the second approach produces time slices and is a clear way to illustrate the propagation and distortion of wavefronts caused by passage through the inhomogeneous structure. For each model seismograms were recorded at intervals of approximately five kilometers along the surface. Groups of seismograms at the same horizontal distance, Δ , from the edge of the grid, were recorded at each of several different Δ' 's. At each of these Δ' 's the surface seismogram and seismograms equally spaced in depth below it were recorded. Such depth sections, with a vertical spacing of 2.5 km, were recorded at distances including those corresponding to positions A through E (Figure 1) for each model. For each one hundred kilometer transition additional depth sections were recorded midway between B and C and midway between C and D. For the fifty kilometer forward transition an additional depth section with vertical spacing of 0.5 km was recorded twenty five kilometers beyond the end of the transition region. This section was used as input for later reverse transition calculations. For the continental layer over a half-space model, or the forward reference model, depth sections were recorded at distances corresponding to positions A through E in each forward transition calculation. Thus, each depth section in a forward transition model corresponds to a depth section in the forward reference model whose component seismograms have

propagated the same distance, both as mode sum synthetics in the same plane layered medium, and as waves in their respective FE grids. Similarly, depth sections at distances corresponding to positions A through E in each reverse transition model are recorded in the reverse reference model calculation. For each model time slices were recorded once or twice every twenty five seconds, that is, every two hundred fifty or five hundred time steps.

At this point it is useful to digress and explain the time slices used in these studies. A time slice records the displacement at each point in the FE grid. These displacements are graphically represented by centered symbols plotted at an array of points depicting the nodes in the FE grid. The size of the symbol plotted at the node is increased as the absolute value of the displacement increases, producing darker areas where larger displacements are occurring. Each of the time slices is self scaled, that is the largest value of the absolute value of amplitude in the grid sets the symbol size to 1.5 element widths at the node where it occurs. At all other nodes the product of two quantities, the ratio of the amplitude at that point to the maximum amplitude, and the size of the largest symbol (1.5 element widths), is the size of the symbol plotted. The symbols also have a minimum size set by the resolution of the plotter. Therefore, to avoid plotting points whose amplitudes vary by orders of magnitude at the same minimum size, a cutoff must be defined below which no symbol is plotted. For the illustrated layer over a half-space time slices this cutoff is one percent of the maximum amplitude. For the illustrated forward and reverse time slices the cutoff is two percent of the maximum amplitude. Setting the cutoff this low means that the smallest symbols cover a range of amplitudes between one or two percent and about eight to ten percent of the maximum amplitude. The self scaling of the time slices means that successive time slices may show the same absolute amplitude as a different symbol size. Thus, the same region of the waveform will appear darker on a time slice

with a given maximum amplitude than on another time slice with a larger maximum amplitude. This difference must be remembered when interpreting the time slices. At any depth within the grid the pattern of displacements seen in a time slice, as a function of distance, can be understood by comparing it to a seismogram recorded at that same depth. The oscillations in amplitude with distance at a given time are similar to those seen as a function of time at a given distance. Thus, the seismogram can be considered to be a recording of the passage of successive points of the coherent wavefield seen in the time slice past a fixed recorder. Conversely, the time slice can be viewed as showing the location in space of the energy that forms each peak in the seismogram, at a given instant of time.

Now, returning to the definition of the model classes used in this study, the two classes of transition models and the two classes of reference models used will be discussed. An example of each transition model class is shown in Figure 1. The difference between individual transition models within each class is the length of the transition region, or the horizontal distance between points B and D shown in Figure 1. The first class of models are used to describe continent to ocean transition regions. In further discussions these models will be referred to as forward models, and the transitions they represent as forward transitions. The second class of models are used to describe ocean to continent transition regions. In further discussions these models will be referred to as reverse models and the transitions they represent as reverse transitions. As the length of the transition region increases in either class of transition model, the angle that the the ocean to crust boundary or crust to ocean boundary makes with the horizontal (ϕ_{OC} or ϕ_{CO} in Figure 1) varies between 3° and 90° , and the angle the the crust to mantle boundary or the mantle to crust boundary makes with the horizontal (ϕ_{MC} or ϕ_{CM} in Figure 1) varies from 12° to 90° . The differences in slope of the boundaries and the different elastic properties of the layers they separate

indicate that different behavior should be expected along those two boundaries. The first type of reference model consists of a thirty two kilometer thick layer over a half-space. This will be referred to as the continental reference model. The second type of reference model consists of two five kilometer thick layers, one water and one of the same material as the layer in the continental reference model, and a half-space of the same material as the half-space in the continental reference model. This model will be referred to as the oceanic reference model. All of these models will be described in detail below. Then the design of the FE grids to represent these models will then be discussed.

The first class of models are models of forward transitions. In each forward model the transition region is characterized by a continuous rate of thinning of the crustal layer between the thirty two kilometer thick continental crust at the beginning of the transition region and the five kilometer thick oceanic crust, overlain by five kilometers of water, at the end of the transition region. The crustal layer has a SH wave velocity, v_C , of 3.5 km/s and a density of 2.7 g/cc, while the half-space has an SH wave velocity, v_M , of 4.5 km/s and a density of 3.4 g/cc. Each transition model has the same boundary conditions (BC's) applied to it. Thus, the same set of forcing functions are used to drive the FE calculation performed on each forward model. In each case the leftmost column of nodes of the forward transition FE grid are constrained to move with the displacement time histories specified by the forcing functions. The forcing functions are a vertical section of sixty mode sum seismograms, calculated at depth intervals of 0.5 km beginning at the surface, for a source at eight kilometers depth at a distance of $\Delta=1500$ km. The same mode sum forcing functions are also used as input to the continental reference model.

The second class of models are models of reverse transitions. Each reverse transition is modeled as a smooth increase in thickness of the crustal layer between a five

kilometer thick oceanic crust, overlain by five kilometers of ocean, at the beginning of the transition and a thirty two kilometer thick continental crust at the end of the transition. The forcing functions for the reverse transition tests are recorded during the fifty kilometer forward transition calculation. They consist of a depth section of hybrid seismograms recorded twenty five kilometers past the oceanic end of the fifty kilometer forward transition region, which corresponds to a distance of 1755 km from the source. The vertical spacing within the depth section is 0.5 km. The reverse transition forcing functions are also used as input to a reverse reference or oceanic model of a five kilometer thick ocean layer and a five kilometer thick oceanic crustal layer over a mantle half-space. An additional series of calculations using the reverse transition models were done to investigate the effects of ocean to continent transitions on mode sum seismograms from an oceanic source. The forcing functions used for these calculations were determined as a sum of the fundamental and the first ten higher modes for a source 1500 km from the grid edge at a depth of eight kilometers below the ocean surface in an oceanic structure. These oceanic mode sum seismograms are also used as input for the reverse reference model.

Finite Element calculations are computationally intensive, consuming many hours of computer time. In order to maximize the information yielded by a calculation using a particular amount of cpu time, the model grids must be carefully designed. It is important to minimize the number of grid points, and the time spacing, and to maximize the spacing between nodes. Other considerations are also important, most notably, the removal of reflections created by the boundaries of the grid from the portion of the waveform to be studied.

The first step in designing a grid for FE calculations is to determine grid size, grid spacing, and the time step duration. These quantities are chosen so that the FE calculation remains stable but executes as rapidly as possible. The highest frequency

of the waveform to be modeled and the S velocity of the material through which it propagates determine the smallest allowable grid spacing. At least six nodes per wavelength are needed to avoid numerical dispersion problems. Therefore, to propagate a wave with a maximum frequency of f through a medium with velocity V , the grid spacing required is

$$dx \leq \frac{V}{6f} \quad (1)$$

It should be noted that in a structure containing regions of different velocities the slowest velocity should be used to determine dx to insure stability of the calculations. Given the minimum grid spacing dx , the maximum time step duration follows directly. To maintain numerical stability in the code the wavefront can travel no more than half the grid spacing per time step.

$$dt \leq \frac{dx}{2V} \quad (2)$$

In this case the minimum velocity, V , within a complicated model should be used to insure stability within the whole model. In this study, we are considering L_g waves with a predominant period of approximately one second propagating through a layer of 3.5 km/s over a half-space of 4.5 km/s. Thus, we have chosen $dx = .5$ km and $dt = .05$ s. This will allow the inclusion of frequencies as high as 1.17 Hz.

The next step in designing the grid is determining the number of grid points that will be needed, the dimensions of the grid, the location of the transition region within the grid, and the duration of the input forcing functions. The dimensions of the grid are expressed as the number of grid points in the horizontal direction, n_x , and in the depth direction, n_z . The location of the transition region within the grid is defined in terms of the distances from the leftmost grid edge to positions A, B, C, D, E, in Figure 1. The values of these parameters were chosen to satisfy two criteria. First, that a

seismogram of duration D_s seconds could be recorded at A (Figure 1) before the multiple reflection of the input wave from the beginning of the transition, B, to the leftmost grid boundary then back to A reaches A. Second, that a seismogram uncontaminated by the multiple reflection with duration D_s seconds could be recorded at the receiver closest to the rightmost edge of the grid. This receiver is defined to be at a distance x_r from the leftmost grid edge. For the calculations in this study x_r was chosen to be twenty five kilometers past the end of the transition. These two criteria concern themselves only with reflections from the leftmost edge of the grid. Nonphysical reflections can also occur from the bottom and the rightmost edge of the grid. These latter reflections are removed using transparent BC's which are explained and verified in a later section. Using the present code it is not possible to apply these BC's to a node which is constrained to a given displacement time history. Applying such a constraint makes the boundary appear rigid to any wave incident upon it from the grid. Since the leftmost column of nodes must be so constrained to couple the source into the FE grid, the left hand edge of the grid is considered to be reflecting. The duration D_s was chosen to be fifty five seconds because it was observed to be the coda length for a SH L_g mode sum seismogram, including the fundamental and the first five higher modes, at a distance of one thousand kilometers from the source. Although the input seismograms finally used were calculated at 1500 km and have a coda of at least seventy seconds, the amplitudes in the coda are reduced by an order or magnitude at fifty five seconds with respect to the beginning of the trace, and are rapidly decreasing. Thus, extending the grids and the number of time steps was considered to be an unnecessary expenditure of computer time. For all the models used in this study the values of parameters defining the size of the grid and the location of the transition region within it are given in table 1. In this table all quantities except n_t and T_{mcalc} are given as the number of nodes in the horizontal direction from the left edge of the

grid to the depth section or boundary indicated. For the corresponding distances in kilometers divide the numbers by two. The quantity nt is given as a number of time steps, and the value of T_{mcalc} is in seconds.

TABLE 1 GRID CHARACTERISTICS FOR TRANSITION MODELS									
	n_x	n_z	nt	T_{mcalc}	A	B	C	D	E
model	# nodes		# Δt	s	# nodes				
Of	310	90	1921	96	230	240	240	240	250
25f	365	90	2101	105	240	250	275	300	310
50f	525	90	3101	155	350	360	410	460	470
100f	500	90	2441	122	250	260	360	460	470
Or	350	90	2561	128	275	285	285	285	295
25r	400	90	2501	125	275	285	310	335	345
50r	450	90	2601	130	275	285	335	385	395
100r	525	90	2941	147	275	285	385	485	495
31f	575	90	2701	135	255	265	315	365	375
31r	575	90	2701	135	417	427	477	527	537
69f	675	90	3001	150	265	275	325	375	385
69r	675	90	3001	150	523	533	583	633	643
fref	530	90	3201	160					
rref	525	90	3201	160					

To calculate the duration of the displacement time histories used to drive the calculation, T_{mi} , the distance from the leftmost side of the grid to the beginning of the transition region, A (see Figure 1), and the number of time steps the calculation must run to produce the desired seismograms, T_{mcalc} , a simple series of calculations was performed. The duration of the forcing functions, T_{mi} , must be long enough that a seismogram of duration D_s can be recorded at both x_f and A. In a layered medium the first arrival at a distance x will occur between the arrival times of a wave traveling entirely in the slowest medium, $T_{\text{slow}} = r/V_{\text{min}}$, and the wave traveling entirely in the fastest medium, $T_{\text{fast}} = r/V_{\text{max}}$. In these expressions $r = \sqrt{x^2 + (h-z)^2}$ where h is source depth and z is receiver depth. To allow the possible arrival time of the first significant energy to be anywhere between T_{slow} and T_{fast} , T_{mi} is chosen to be D_s plus

the travel time difference $\Delta T = T_{\text{slow}} - T_{\text{fast}}$. Since ΔT will be largest for the longest distance, providing a long enough seismogram at x_f will automatically provide one at A. So T_{mi} becomes

$$T_{mi} = D_s + x_f \frac{V_{\text{max}} - V_{\text{min}}}{V_{\text{max}} V_{\text{min}}} \quad (3)$$

In this expression r has been replaced by x . This is a valid substitution for distances $x \gg x_c$, the critical reflection distance. For the examples considered here the source to receiver distance is larger than 1500 km, well in excess of the critical reflection distance. This would seem to imply that this substitution is valid for these calculations. However, the coupling of the energy from the distant source into the FE grid requires the specification of displacement time histories on a column of nodes. This is equivalent to applying a time variable source at each of the nodes constrained by a forcing function. The distance from these sources to the receivers within the FE grid is less than or of the same order as x_c . It can still be shown that the substitution of x for r is valid, although, it may give an overestimate of the necessary duration, T_{mi} . To demonstrate this consider a receiver at depth z . The first significant energy at that receiver arrives from the nearest source, that at depth $h=z$. Thus, substituting x for r in the expression for T_{slow} is correct. Substituting x for r in the expression for T_{fast} will either make no difference or decrease the value of T_{fast} . Thus the travel time distance, ΔT , can be larger than the exact value but not smaller. This guarantees that portions of the seismogram that should not be contaminated with reflections will not be.

To determine a numerical value for T_{mi} , the distance x_f must be known. The value of x_f follows directly when the distance to the beginning of the transition, B, is known. To assure a seismogram at A of duration D_s which is not contaminated by reflections from the leftmost edge of the grid it is sufficient to specify that the two

way travel time from A to the leftmost edge of the grid be T_{mi} . Then the unknown value of x_r cancels and A can be expressed as

$$A = \frac{D_s V_{min} V_{max} + (T_l + x_r)(V_{max} - V_{min})}{(V_{max} + V_{min})} \quad (4)$$

where V_{min} is the velocity in the oceanic and continental crustal layers (3.5 km/s), V_{max} is the velocity in the mantle layer (4.5 km/s), and T_l is the length of transition region, (0, 25, 50, 100 km), x_r is the distance from the end of the transition to the last receiver (25 km) plus the distance from A to B (5 km). Once the distance to A is determined the distances to B, C, D, E, and x_r are known. This allows T_{mi} to be determined from (3), and the duration of the calculation follows directly.

$$T_{mcalc} = D_s + \frac{x_r}{V_{min}} \quad (5)$$

These calculations are modified slightly when the output at x_r is to be used as the input to a subsequent FE calculation. The necessary duration of uncontaminated seismogram at x_r becomes the duration of the input forcing functions needed for the second FE calculation. This is why the values of A, T_{mi} , and T_{mcalc} , for the fifty kilometer forward transition are larger than the values given by the above relations. The seismograms from the fifty kilometer forward transition at x_r are used as the forcing functions for all the reverse transition calculations. When a series of more than two FE calculations are performed, the values of the parameters above should first be determined for the final calculation. The value of T_{mi} for this calculation will give the value of D_s for the penultimate calculation. In this way the values of the parameters for each FE calculation from the last to the first can be determined.

Understanding the Accuracy and Efficiency of the Transparent BC

Transparent boundary conditions (BC's) are applied at two boundaries, both the rightmost edge and the bottom edge of each transition model FE grid. These, BC's

are introduced to remove the nonphysical reflections created by the interaction of the wavefronts with those two boundaries. Their introduction removes the requirement that those boundaries be far enough from the receivers that no reflections from them contaminate the desired results. However, the BC's do not remove all of the reflected energy, thus for detailed waveform modeling it is preferable to enlarge the grid rather than using the BC's, if such an enlargement is feasible. In all other cases, where small discrepancies in waveform can be tolerated, the interference on the small reflection with the incoming seismogram produces changes of less than 1% in the RMS amplitudes. For seismograms of fifty five seconds duration, removing the reflection from the right end of the grid by extending the grid would require increasing n_x by almost two hundred grid points. This increases execution time by thirty to sixty percent. If reflections from the bottom edge of the grid must also be removed, n_z must also be increased by two hundred grid points. The increase in execution time to remove both types of reflection by extending the grid is a factor of three to five. Clearly, a more efficient way to remove the reflections is desirable.

The transparent BC used in the calculations discussed in this study is implemented by averaging a rigid boundary solution with a free boundary solution for the displacement at the edge nodes. If no boundary condition is applied the boundary nodes form a free surface. When a wavefront interacts with a free surface a complete reflection of the incident wavefront occurs. If the edge nodes are constrained to have zero displacement, that is to produce a rigid boundary, the incident wavefront is completely reflected, but a change in the sign of the amplitude is introduced. This suggests that one way to remove contamination due to reflections is to add a solution with a rigid right edge boundary to a solution with a free right edge boundary (Smith 1974). Adding the corresponding seismograms from these two separate calculations is, however, a poor solution. Such an approach takes more computer time than simply

extending the grid in n_x , and it also removes only the primary reflections, leaving multiple reflections to contaminate the results. The situation for removing reflections due to both bottom and edge boundaries is little better since four separate calculations are required to remove the primary reflections in this case. A better solution, suggested by Frazier, Alexander, and Petersen (1973), is to calculate displacements for the rigid boundary and for the free boundary cases, for each edge node at each time step. Those two displacements can then be averaged to give a displacement closer to that observed if the boundary was not present. For a normally incident plane wave this average exactly represents the transparent boundary. However in practice the incident wavefront is neither normally incident nor a plane wave. This means that the actual value at the transmitting boundary is a linear combination of the rigid boundary and free boundary solutions whose coefficients depend upon the angle of incidence of the energy. The boundary condition used here assumes that the average of the two solutions will in most cases be the best approximation to the transparent boundary that can be simply implemented. To implement the transparent BC's about twice as many calculations are necessary at each node on the transparent boundary. This increases the overall execution time of a transition type run by less than two percent.

The efficiency of the transparent BC's must be demonstrated and their limitations must be understood. The validity of the BC's for L_g mode sum input will be discussed later, but to more clearly illustrate their limitations it is useful to examine their effects on a simple SH pulse traveling in a homogeneous 2-D half-space. Two different situations are examined, first reflections from the rightmost edge of the grid are considered, then reflections from the bottom of the grid. The grids used for each of these tests are shown in Figure 2. The heavy lines within the grid show the nodes where hybrid seismograms are recorded. The time step used was of 0.05 seconds duration,

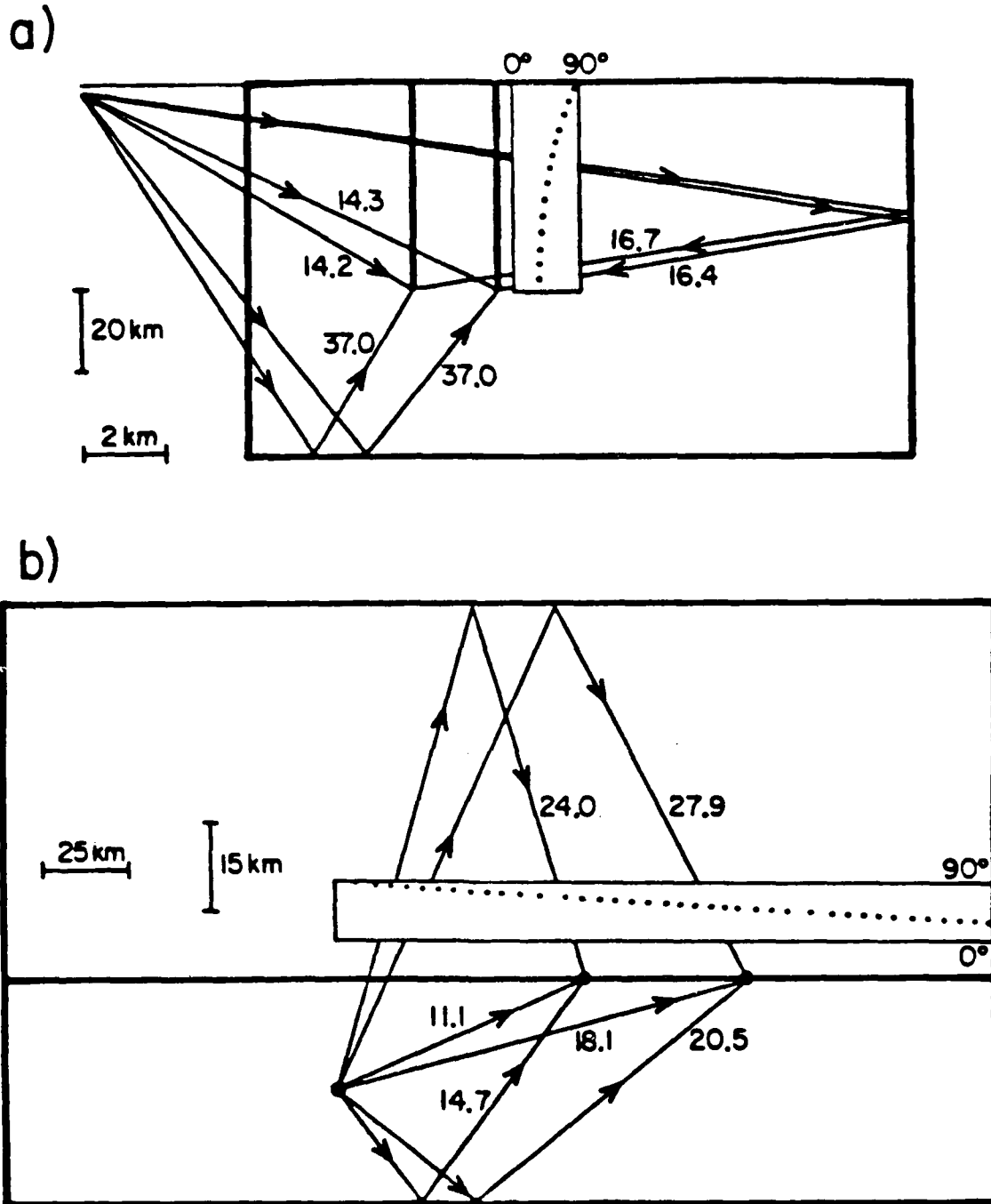


Figure 2: Grid geometries for the tests of the boundary condition for a 2-D SH pulse. Part a) shows the grid used to investigate reflections from the right end of the grid, part b) the grid used to study reflections from the bottom of the grid. Sample source to receiver ray paths are shown in both grids for the direct path, and for the path reflected from the grid bottom. Sample ray paths including a reflection from the right grid edge in a), or a free surface reflection in b) are also shown. Each ray path is labeled with its travel time. The sets of receivers are indicated by the solid lines within the grids. The dotted lines in the inset boxes show the variation of incident angle as a function of receiver depth or range.

and the grid spacing was 0.5 km. The dotted line in the inset rectangle shows the variation of the angle between the incident SH ray and the boundary being investigated along that boundary. In each grid the important SH ray paths are illustrated for sample receivers, and labeled with their travel times.

The geometry of the grid used to examine edge reflections is illustrated in Figure 2a). The size of this grid, 80x450 nodes. Examining the illustrated travel times shows that no contamination from bottom reflections reaches the receivers during the thirty five second duration of the seismograms. The horizontal distance from the source to the left edge of the FE grid is four kilometers. The horizontal distances from the source to the depth sections where results are recorded are eight and ten kilometers. The vertical range of receivers is between the surface and fifty kilometers depth. Thus, angles of incidence at the right end boundary of the FE grid are between thirty and ninety degrees.

The geometry of the grid used to study reflections from the bottom of the FE grid is shown in Figure 2b). The dimensions of the grid are 350x110 nodes. For this series of calculations the source used is a line source applied at a single point within the grid. The source was located within the grid to allow for a large range of angles of incidence at the bottom boundary. The time history of the force applied at the source is triangular with a rise time of ten time steps and a total width of twenty time steps. The small higher frequency oscillations superimposed on the decaying portion of the pulse in both calculations is due to finiteness of the embedded source. The illustrated travel times indicate that the reflection from the free surface arrives at a time well separated from the reflection from the bottom of the grid.

Figure 3 illustrates the effect of introducing the transparent BC's at the right-most grid edge of the grid shown in Figure 2a). Each pair of seismograms represents one of the receivers on the depth section eight kilometers from the source. Figure 4

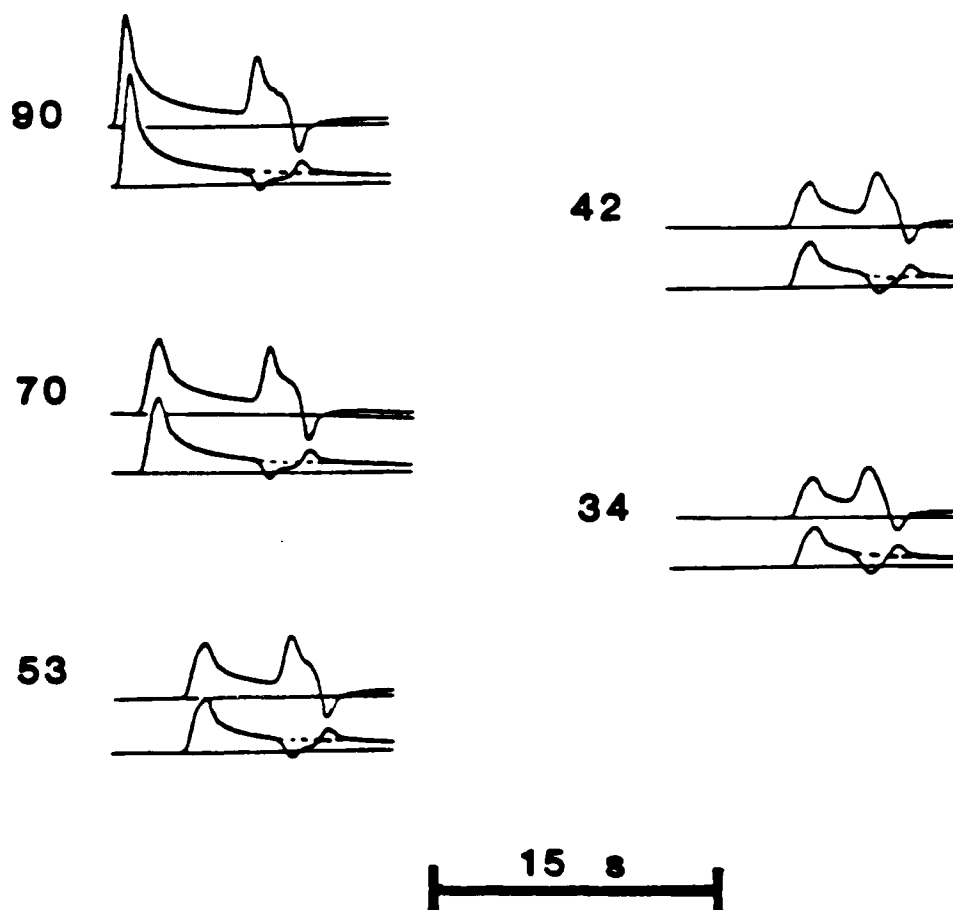


Figure 3: Efficiency of the absorbing BC demonstrated by results from calculations in the grid illustrated in Figure 2a. The uppermost seismogram in each pair is the hybrid solution with no BC's applied. The lower seismogram of each pair shows the hybrid solution with the BC applied to the appropriate boundary as a solid trace and the direct synthetic solution as a dotted line. The numbers beside each pair indicate the angle of incidence of the arrival at the reflecting boundary.

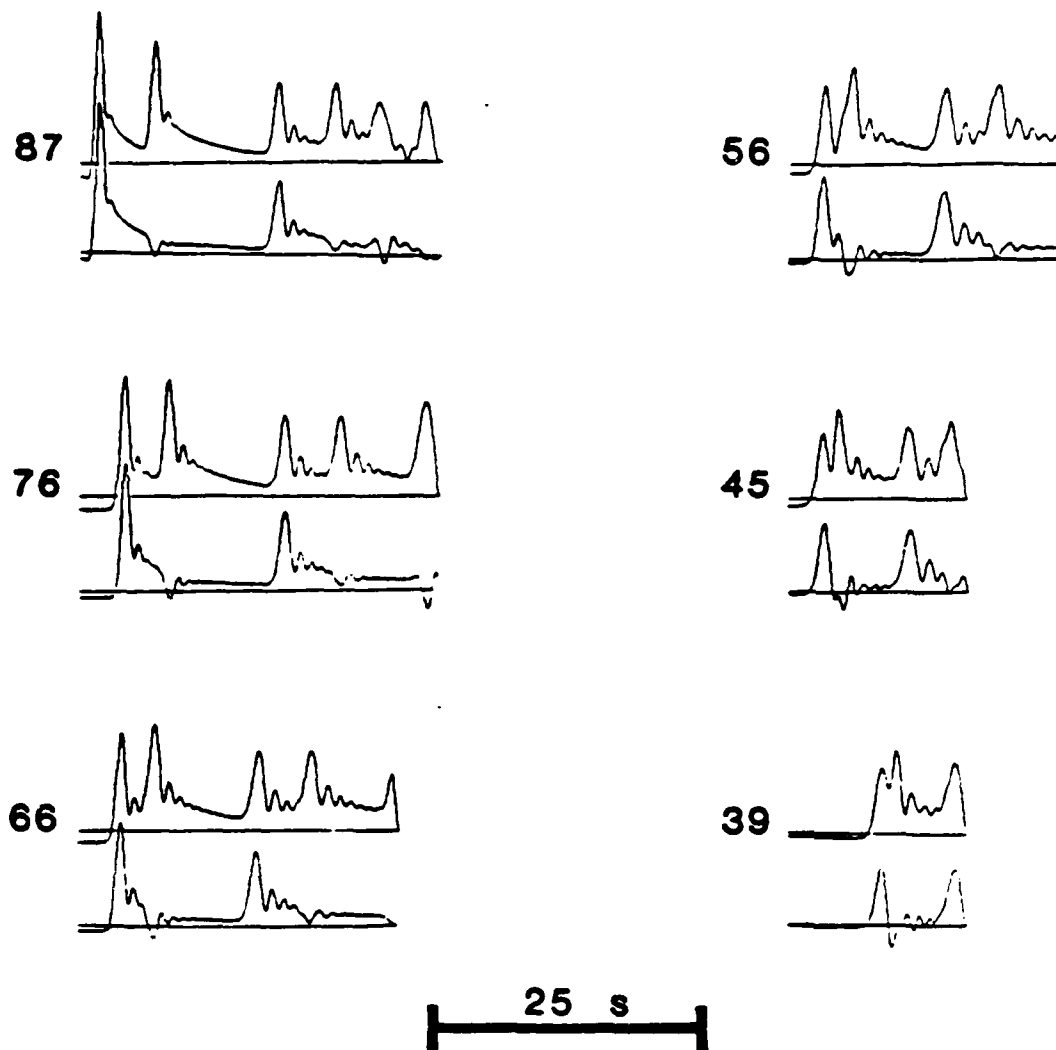


Figure 4. Efficiency of the absorbing BC demonstrated by results from calculations in the grid illustrated in Figure 2b. Details are identical to those explained in Figure 4.

illustrates the effect of introducing the them at the bottom grid edge of the grid shown in Figure 2b). Each pair of seismograms represents one of the receivers along the plane at thirty five kilometers depth. The uppermost trace in each pair shows the hybrid synthetic with no BC applied. The lowermost trace of each group shows both the analytic synthetic and the hybrid synthetic calculated using the BC. on the rightmost edge of the grid. The dotted portion of this trace shows where the analytic synthetic departs from the hybrid solution. The number to the left of each pair of traces indicates the angle of incidence, in degrees, at the rightmost edge of the grid in Figure 3 or the bottom edge of the grid in Figure 4. A second reflection, whose amplitude is inverted with respect to the first, is seen in Figure 3 only. This is the multiple reflection from the rightmost grid edge then from the rightmost grid edge. It illustrates that a boundary, such as the rightmost grid edge, with displacement time history constraints applied to it acts as a rigid boundary when considering energy incident upon it from the FE grid. In Figure 4 the upper trace in each group shows two pairs of almost equivalent sized peaks. The first pair of peaks are the direct arrival and its reflection from the bottom edge boundary of the grid, the second smaller pair of peaks shows the free surface reflection followed by its multiple reflection from the bottom grid edge.

For normal incidence the BC is very efficient, removing 93% of the reflected amplitude. The reflected pulse prominent when no BC is applied is very small when it is applied. For near normal incidence, the BC continues to be efficient, reflecting at most thirty percent of the incident amplitude for angles of incidence as small as fifty degrees. The BC is equally efficient for the same angle of incidence on either boundary. The two grids used to investigate the two boundaries separately illustrate some difficulties that occur when using such an angularly dependent transmitting BC. Most geometries of interest here involve a distant source, so the angles of incidence at the

bottom boundary are much smaller than at the rightmost edge boundary. When the angle of incidence is small less than half the incident energy is removed. Thus, although the reflections from the rightmost grid edge are uniformly small and produce on the order of a one percent change in RMS amplitude for a distant source, the reflections from the bottom of the grid are only slightly reduced in amplitude and contribute significant unwanted components to the resulting seismograms. Conversely, a nearby source was chosen for the test of the BC at the rightmost edge of the grid and a source in the grid was chosen for the bottom grid boundary test. In both cases these choices were made to give a large range of incident angles in the calculations.

Next the validity of the BC's for L_g mode sum seismogram input will be discussed. Figure 5 shows the layer over a half-space (L/HS) grid models used to verify the accuracy and efficiency of the BC's as applied to SH L_g wave propagation. All FE calculations discussed for the test use the forward transition forcing functions as input. The results of these calculations are illustrated in Figure 6 and Figure 7. Both figures show seismograms that have been band pass filtered between .01 and 1.0 Hz. The seismograms shown in Figure 6 have also been convolved with the WWSSN short period instrument response. Four separate calculations were performed. First, an L_g mode sum synthetic seismogram for the same source used to generate the forward transition forcing functions was calculated for surface nodes at distances corresponding to R1 and R2 in Figure 5. These are the uppermost traces in each group in Figure 6. Next, seismograms were generated using the hybrid method and the long grid, in Figure 5. No BC's were applied when the seismograms were propagated through the FE portion of the path. The length of the long grid, $n_x=200$, was chosen so that fifty five seconds of seismogram could be recorded at R1 and R2 without contamination from end reflections. Sample results from this calculation are shown as the second seismogram in each group in Figure 6 and the uppermost seismogram in each group in

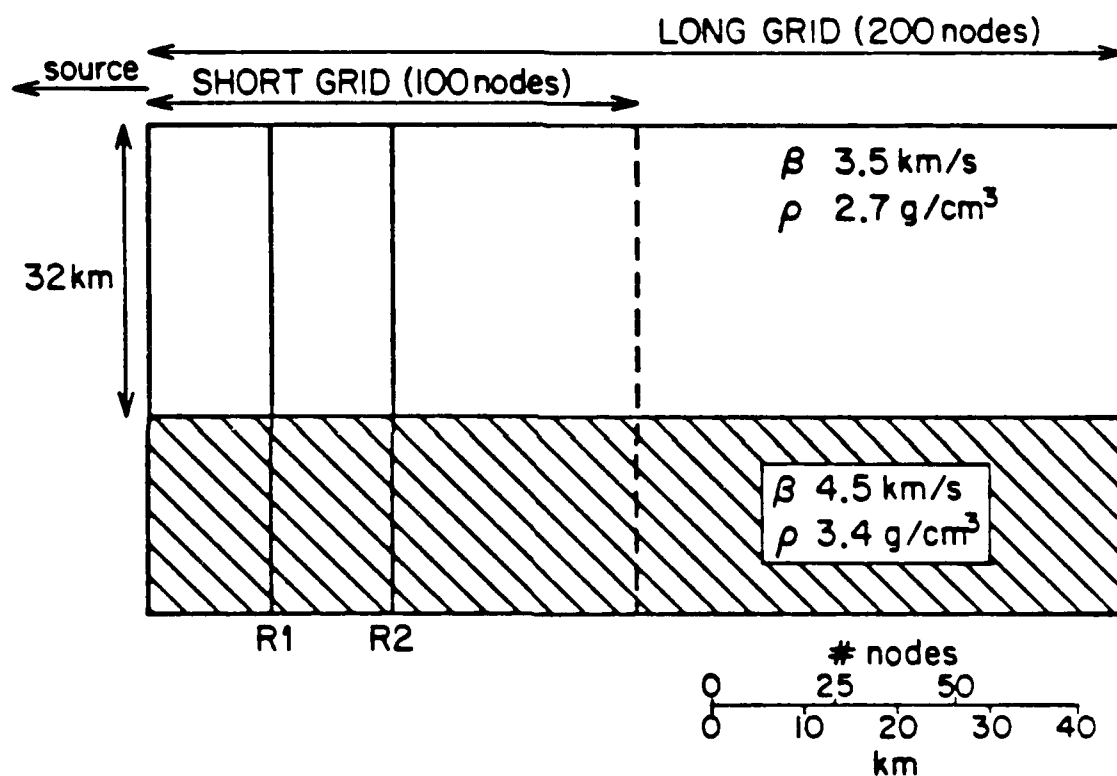


Figure 5: Grid configuration for test of absorbing BC's for the case of incident L_g mode sum waves. The solid vertical lines within the grid shown the locations of the depth sections of receivers where results are recorded. The dotted vertical line indicates the end of the short grid.

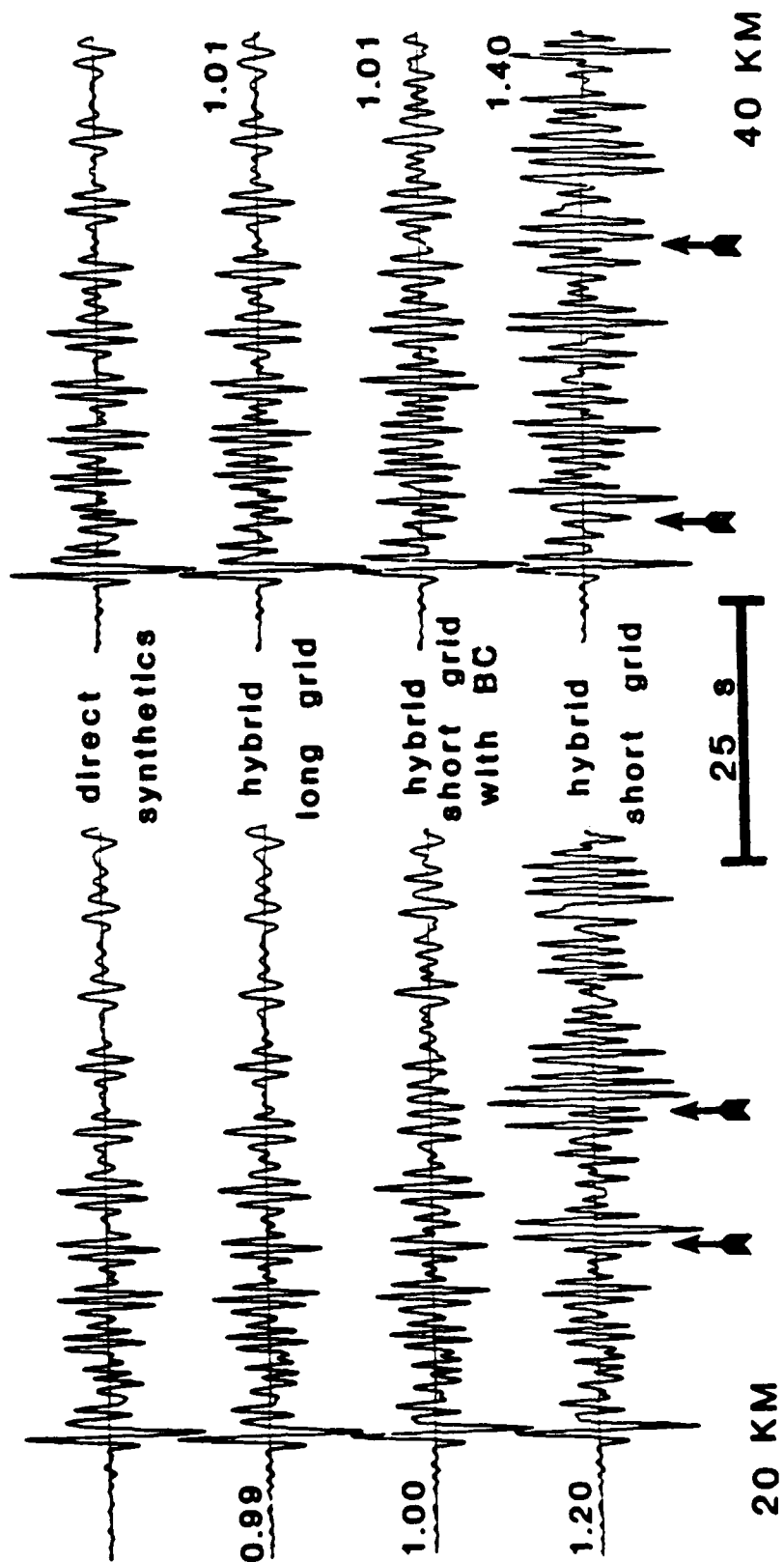


Figure 5: Seismograms recorded at the surface for the distances R1 and R2 in Figure 5. The first seismogram in each group is a direct synthetic, the second is a hybrid synthetic determined using the long grid shown in Figure 5, the third and fourth are hybrid synthetics determined using the short grid in Figure 5 with and without the applied BC respectively. The number beside each of the hybrid synthetics is the RMS amplitude ratio. The amplitude ratio is taken with the direct synthetic as a reference. Seismograms are plotted at the same scale after they have been band pass filtered between .01 and 1 Hz and have been convolved with the short period WWSSN instrument.

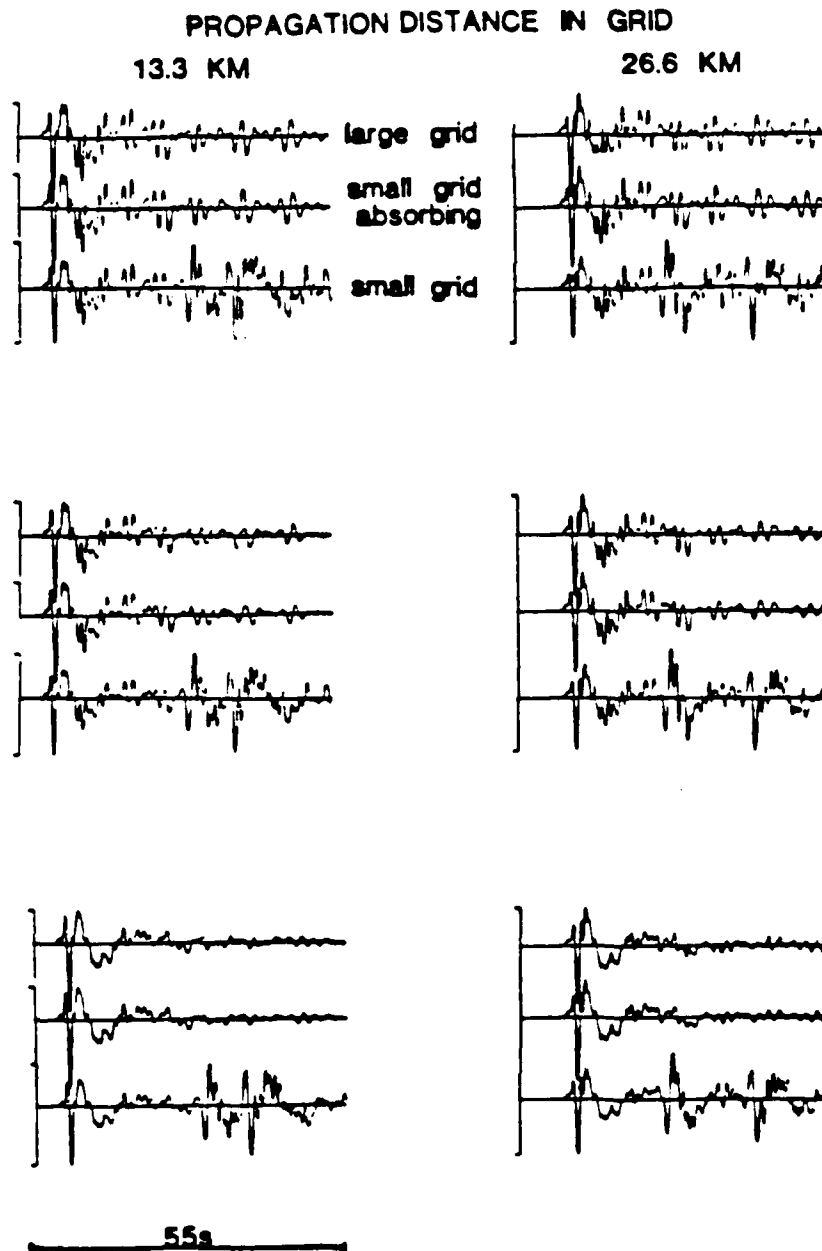


Figure 7: Seismograms recorded at the surface and at depth at the distances R1 and R2 in Figure 5. The first seismogram in each group is a hybrid synthetic determined using the long grid shown in Figure 5. The second and third are hybrid synthetics determined using the short grid with and without BC's respectively. Seismograms are normalized so the peak to peak amplitude of each trace appears identical. RMS amplitudes of each group of traces agree to within 1% before the arrival of the reflection. The seismograms have been band pass filtered between .01 and 1.0 Hz.

Figure 7. Third, seismograms were generated using the hybrid method and the short grid illustrated in Figure 5. The short grid is terminated at its rightmost edge by the vertical dotted line. Along this edge the transparent BC was applied at each node at each time step in the calculation which propagated the input seismograms through the FE portion of the path. Seismograms resulting from this calculation are shown as the third trace in each group in Figure 6 and as the center trace in each group in Figure 7. Finally, the previous FE calculation was repeated without the transparent BC's, and the results are illustrated as the fourth and final trace in each group in Figure 6 and as the bottom trace in each group in Figure 7.

When the final three traces in each group in Figure 6 are compared to each other or the three traces in each group in Figure 7 are compared to each other it becomes clear that the transparent BC's are removing most of the reflected energy. In the last trace the reflection from the grid edge is clearly visible, and the multiple reflection is also clear. Arrival times of the two large peaks marking these reflections are consistent with their identification as reflections. The arrival time of the two reflections are shown on Figure 6 as arrows below the bottom seismogram in each group. Comparison of the long grid and the short grid with transparent BC's shows that most of the reflected amplitude has been removed by the BC's. Comparing the results show in Figures 6 and 7 shows that the BC's are also somewhat frequency dependent for L_g mode sum seismogram type input. Very little difference is seen between the hybrid long grid solutions and the hybrid short grid solutions with the BC's applied when the results in Figure 7 are examined, and the changes that are seen appear to be in the higher frequency component of the traces. This observation is corroborated by the results shown in Figure 6. These results have had the WWSSN short period instrument applied to them, and thus, have had their higher frequency component enhanced and their lower frequency component attenuated. They show larger differences

between the hybrid long grid solutions and the hybrid short grid solutions with the BC's applied than are visible in the results before the instrument is applied. The increased differences are coincident with reflections obvious on the seismogram showing the hybrid short grid results without BC's. The differences are largest for the multiple reflections. Despite easily visible differences in waveform the seismograms shown in Figure 6 have RMS amplitudes that agree to within less than two percent for all RMS window lengths. This indicates that small changes in waveform may be expected but the amplitudes of the seismograms should be stable and not significantly contaminated by reflections from the grid edges. The increased discrepancies in both waveform and amplitude introduced by the multiple reflections will be avoided in the transition FE grids described below. This reduces the discrepancies in RMS amplitude to less than one percent.

Reflections from the bottom edge of the grid should also be considered. As previously discussed, the transparent BC can be very inefficient for the case of an SH pulse incident at the bottom of the grid. Due to the small angle between the SH ray and the grid bottom for any source which is not in the grid or in close proximity to the grid the BC will remove only a small portion of the reflected amplitude. Fortunately, this behavior does not generalize to modal displacement in a layered half-space. For the case of L_g mode sums propagating in a layer over a half-space, the L_g wave input to the grid is constructed as a superposition of Love wave modes. These Love wave modes can be thought of as the superposition of the constructive interference between multiply reflected post-critical SH waves in the crust. This suggests that much of the energy in the SH type L_g waves for a layer over a half-space should be contained in the layer, interacting predominantly with the real boundary between the layer and the half-space, and with the free surface. The waveforms of the hybrid seismograms with and without the transparent BC's on the grid bottom are almost identical. Amplitude

comparisons show differences of less than 0.1%. This can be seen by examining the first two seismograms in each group in Figure 6. The analytic synthetics and the hybrid results with no BC's are in excellent agreement indicating that reflections from the bottom boundary in the FE portion of the hybrid calculation are not significant. Thus, it appears that, for a layer over a half-space, reflections from the grid bottom are not important when modal displacements are being propagated. This argument applies to the forward and reverse reference models when mode sum SH L_g seismograms generated for the forward or reverse reference modes respectively are used. This argument cannot, however, be generalized to imply that little energy reaches the bottom boundary for the transition model calculations, or for the reverse reference model using the depth section recorded at x_r in the fifty kilometer forward transition model as forcing functions. It will be shown that in these models significant energy escapes from the crustal layer into the mantle half-space.

The properties discussed above are also observed in the time slices from the layer over a half-space calculation shown in Figure 8. At the upper right corner of each time slice a number indicating the time, in seconds, since the beginning of the FE calculation is shown. The arrows pointing to the surfaces of the bottom three time slices show the location that the slowest traveling energy seen at the leftmost edge of the wavefield of the previous time slice has moved to in the time elapsed between the two sections. The first striking feature of the time slices are that the SH type L_g waves are, in the most part, confined within the layer. The bottom of the layer in the illustrated depth sections is easily visible as the bottom of the high amplitude portion of the wavefield. This delineation is clear even though forcing functions are applied to all illustrated rows of nodes. Thus, the time slices show that a negligible portion of the energy interacts with the bottom of the grid. Thus, introducing transparent BC's on the bottom of the grid where little energy reaches makes no perceptible difference in

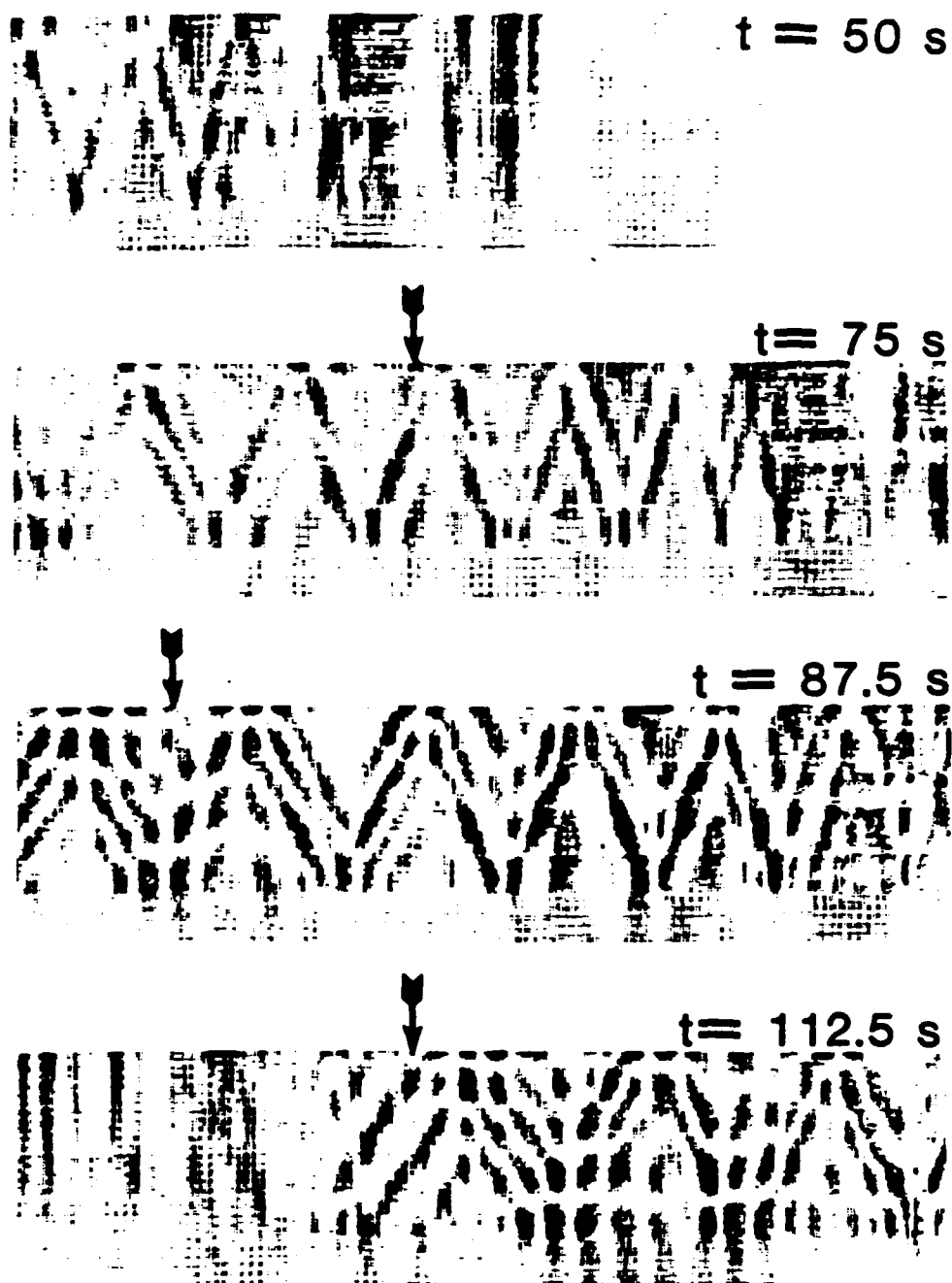


Figure 8: Time slices showing the propagation of an SH type L_g wavefield through a layer over a half-space structure. The bottom of the layer can be seen as the lower termination of the darker regions. The dark triangular regions show the wavefronts. The arrows above the lower three time slices show the location of the slowest traveling energy visible at the lefthand edge of the previous time-slice at the time of the present time slice. The time since the initiation of the FE calculation is shown at the upper right corner of each time slice.

the results. The second striking feature is that the high amplitude portions of the wavefield resemble the wavefronts for multiply reflected SH waves of a collection of different phase velocities superimposed upon one another.

Another feature clearly visible in these time slices is the energy reflected back toward the source from the rightmost edge of the grid. The upper two time slices both show the maximum amplitude portion of the waveform propagating through the grid. In the first time slice the large peaks at the beginning of the waveform, seen as the darkest regions, have propagated about halfway across the grid. In the second time slice they have reached the right end of the grid. In the third time slice these high amplitude regions have propagated beyond the rightmost edge of the grid. Thus, the maximum amplitude in the third time slice is smaller than that in the first two time slices. The same regions of wavefield in the third time slice appear darker than in the second time slice. The reflection from the grid edge is also visible if the time slice is carefully examined. In the fourth time slice, the maximum amplitude has again been reduced and the end of the applied wavefield is accentuated. The amplification also makes the reflected wavefield clearly visible particularly in the portion of the grid which the incident wavefield has completely passed through. The end of the incident wavefield is clearly visible in this time slice as the end of the portion of the wavefield showing superimposed triangular regions of high amplitude. To the left of this area an attenuated mirror image of the beginning of the incident wavefield can be seen. This is the beginning of the reflected wavefield. Examining seismograms shows that actual amplitudes of this reflection are between five and eight percent of the incident amplitudes.

This discussion has established that the transmitting BC at the grid bottom boundary is not important for SH type L_g mode sum seismograms traveling through the same layered structure in which the source is located. However, the purpose of

this study is to examine the effects of continental oceanic boundaries on the transmission of L_g mode sum seismograms. When the crustal layer is thinned or thickened with distance, the modes are no longer completely trapped within the layer. Energy can be converted to modes compatible with the local layer thickness and to other forms including forms such as body waves that can propagate into the half-space and away from the layer. When the wavefield reaches the second layered structure, modes incompatible with that new layer thickness will leak out of the layer, rapidly at first, then at a steadily decreasing rate. These phenomena are observed and will be discussed and explained in detail later as the results are presented. They imply that reflections of energy escaping from the crustal layer towards the bottom boundary of the grid could possibly seriously contaminate transition calculation results. The grids are designed to minimize these problems. Consider a node on one of the dotted boundaries shown in Figure 1. At this node energy is converted into modes consistent with the local layer thickness and into forms that will propagate into the half-space. Thus, it can be considered as a source for a wavefield propagating into the half-space. Wide angle reflections, of the energy escaping from the thinning crustal layer, from the grid bottom require long distances, Δ , to travel from this source to the grid bottom to the receiver. In almost all cases the model grids do not extend far enough, in the x direction, beyond the transition for this to be a problem. The energy will encounter the rightmost end of the grid, either on the downgoing or the upgoing portion of its path, rather than reaching a receiver at or near the surface as a wide angle reflection. Since a wavefront which has a small angle of incidence with the bottom boundary has a large angle of incidence with respect to the end boundary, most of the amplitude of the wavefront from the conversion source incident on the rightmost end boundary, will be transmitted rather than reflected. Therefore, it is removed from the grid. Careful grid design will prevent significant contamination from wide angle bottom reflections.

The results from the forward and reverse transition calculations will now be discussed. First the effects of a forward transition on the incoming SH L_g mode sum seismograms will be explained. Then, the further effects due to continued propagation of this energy through a reverse transition will be considered. Next, the variation in the effects introduced by the forward transition as a function of transition length will be discussed. Finally, the variations in the effects observed as the wavefront passes through the reverse transition, as a function of the length of that transition will be explained. The consideration of the effects due to varying the length of the oceanic path between the two transition regions will be discussed briefly. A more complete discussion of this problem will be given in the next chapter.

Changes to L_g Wavetrains on Passage through a Forward Transition Region

The passage of a wavefield consisting of SH type L_g mode sum energy contained mainly in the layer above the half-space through a forward transition such as that illustrated in Figure 1a) has several effects on that wavefield. These effects are illustrated in Figures 9 to 15. These figures show several important tendencies. As expected the behavior along the continent ocean boundary shows distinct differences when compared to the behavior at the crust mantle boundary. Along the continent ocean boundary amplitudes are seen to increase with distance, Δ . No energy is propagated into the ocean layer. Energy which is not reflected back from the crust ocean boundary toward the source appears to be concentrated near this boundary and propagated along it to produce an amplification of amplitude which is maximum at the surface of the crust. Along the crust mantle boundary a similar but smaller concentration effect is seen. However, this effect is dominated by the conversion and/or escape of energy across the boundary into the mantle layer. The propagation of the energy remaining in the crustal layer when the wavefront leaves the transition region

through the oceanic layered model shows that energy is leaking out of the bottom of the oceanic crustal layer, particularly at the beginning of the oceanic layer near the end of the transition region. Each of these observations will be discussed in detail below and supporting results will be shown in the figures.

First the results of a sample calculation with a transition length of twenty kilometers will be discussed. The geometry of the grid is illustrated, to scale, in Figure 9. The upper hatched region is the ocean layer, the unhatched region the crustal layer, and the lower hatched region is the mantle layer. The heavy vertical line at the left-most edge of the grid represents the column of nodes constrained to move with the input L_g displacement histories. The heavy vertical line labeled A is the column of nodes for which displacement time histories are recorded to use as input to the reverse transition. The two vertical lines labeled Fc1 and Fc2 show receiver sections used to illustrate the effect of the transition on the distribution of amplitude with depth. Dots on Fc1, and Fc2 indicate positions of receivers for which displacement time histories are illustrated in Figure 10. Open circles, and dots located at the surface of the crustal layer, refer to nodes for which displacement histories are plotted in Figure 11. In both Figures 10 and 12 all seismograms are band pass filtered between .01 and 1.0 Hz, but no instrument is applied. The numbers above and to the right of each seismogram are the maximum peak to peak amplitudes of each seismogram.

Figure 10 shows seismograms recorded at the positions shown as dots in Figure 11. The first column of seismograms in this figure shows the changes seen with depth at distance Fc1. The second column shows the seismograms on depth section Fc2. The seismogram at the surface of the oceanic crustal layer in the depth section at Fc2 shows a substantial increase in amplitude over the seismogram at the same depth in depth section Fc1. These seismograms are shown as the second row in this figure. Not only is the peak to peak amplitude fifty percent larger but the average amplitude

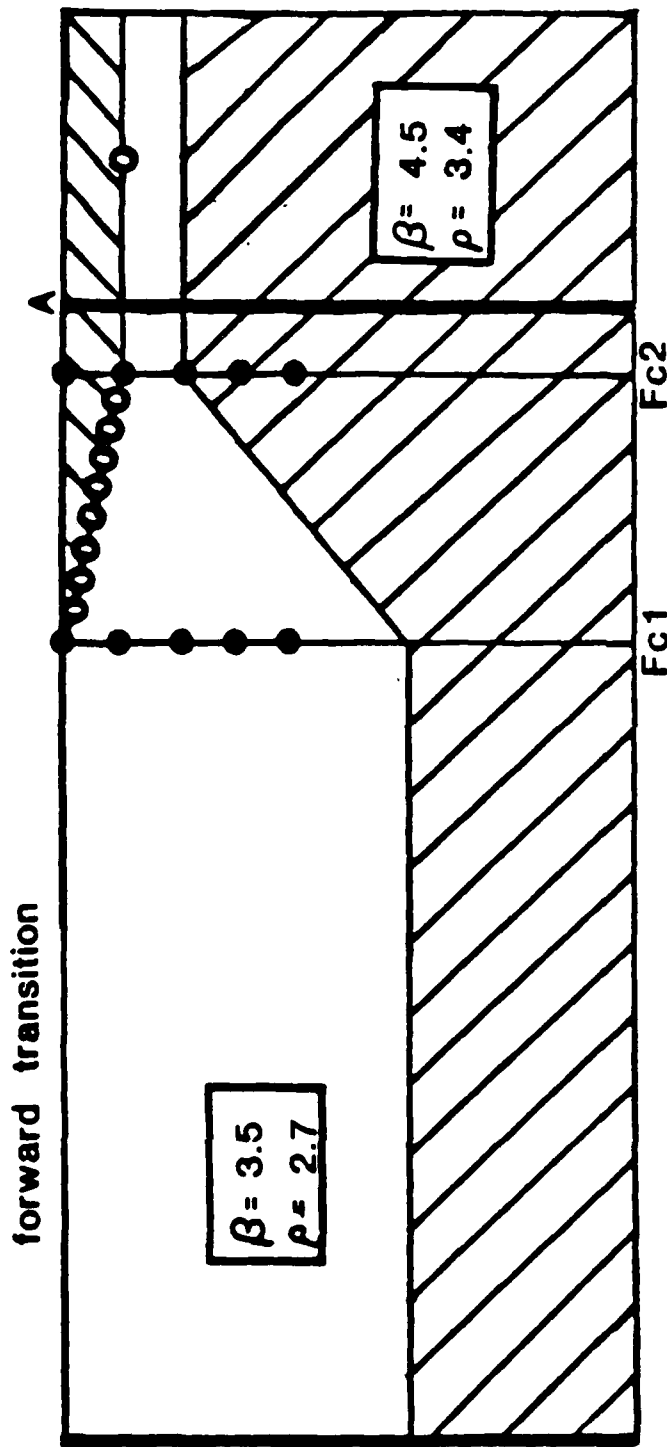


Figure 9: Grid geometry for the twenty kilometer forward transition used to illustrate the effects of a forward transition on the waveforms and amplitudes of seismograms as a function of distance, Δ , and depth. The upper hatched region is the oceanic layer, the lower hatched region the mantle layer, and the unhatched region the crustal layer. The heavy vertical line labeled A shows where seismograms are recorded for use as forcing functions in the reverse transition calculation. The heavy line at the left end of the grid is the column of receivers to which SH L_q seismograms are applied as forcing functions. The vertical lines labeled Fc1 and Fc2 show depth sections of receivers. The dots on Fc1 and Fc2 show receivers for which seismograms are illustrated in Figure 10. The open circles along the surface of the crustal layer show the receivers for which seismograms are shown in Figure 11.

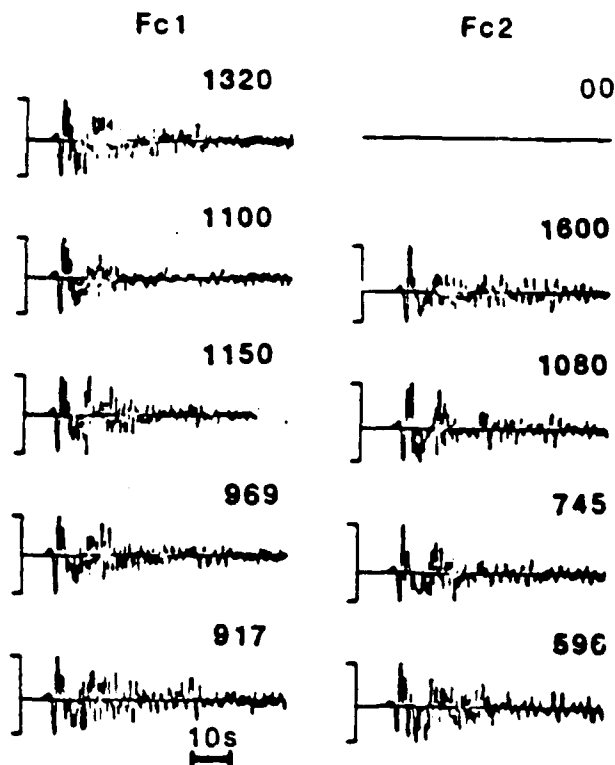


Figure 10: Seismograms recorded at receivers shown as dots on depth sections Fc1 and Fc2 in Figure 9. The first column shows the seismograms recorded at Fc1, the second the seismograms recorded at Fc2. The numbers above the right end of each seismogram show the peak to peak amplitude. The first row of seismograms show receivers at the depth of the surface of the continental crust. Successive rows show pairs of receivers at increasing depths. The second row is at the depth of the surface of the oceanic crust, the third at the depth of the base of the oceanic crust. All receivers illustrated are above the base of the continental crust.

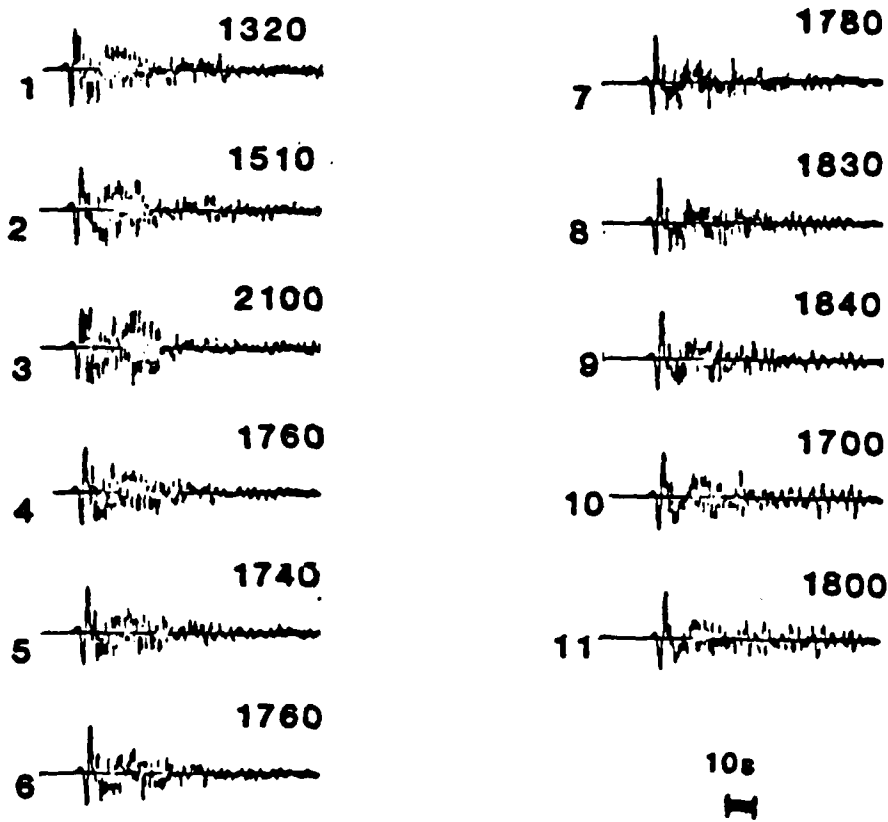


Figure 11: Seismograms recorded at receivers along the surface of the crustal layer in a forward transition calculation. These seismograms are recorded at the receivers shown as open circles and dots on the surface of the crustal layer in Figure 10. The numbers to the left of each seismogram indicate the location of the node at which that seismogram is recorded. The leftmost open circle is receiver 1. The numbers increase as one moves to the left along the surface of the crustal layer. The numbers above the right end of each seismogram give the peak to peak amplitude of that seismogram.

of the coda has increased by a factor of approximately two with respect to the maximum peak to peak amplitude. Thus, the increase in RMS amplitude is considerably larger. The nodes at the depth of the bottom of the oceanic crustal layer, the third row of seismograms in this figure, show a small decrease in peak to peak amplitude and a relatively constant RMS amplitude across the transition. Examination of the nodes on Fc1 and Fc2 with depths between these pairs shows that the increase in amplitude is largest at the surface of the crust and decreases rapidly toward the base of the crust. The amplitudes of the seismograms transmitted across the crust mantle boundary, rows four and five in this figure, are decreased by passage through the transition region. The transmitted waveforms are similar to the incident waveforms and show an increasing reduction in transmitted peak to peak amplitude as depth increases. Amplitude is seen at depths below the depth of the bottom of the continental crustal layer. These results support the statements that energy is concentrated at and then travels along the crust ocean boundary, and that energy escapes from the crustal waveguide when the wavefield crosses the transition. They also indicate that some of the energy escaping from the transition region into the half-space is traveling down towards the bottom boundary of the grid. This figure helps quantify the magnitudes of these effects. The actual distortions of the wavefield will be clearer when the time slices, Figures 12 to 14, are discussed.

Figure 11 shows seismograms recorded at the receivers along the surface of the crust. These receivers are shown in Figure 9 as open circles and as the dots on crustal surface on depth sections Fc1 and Fc2. The numbers to the left of each seismogram show the sequence, in space, at which the seismograms were recorded. Seismogram one was recorded at the leftmost surface receiver shown in Figure 9. The number used as the label increases as one moves towards the right across Figure 9. A clear increase in peak to peak amplitude is seen as one moves down the crust ocean boundary

towards the oceanic portion of the model. This increase is not necessarily monotonic, as will be shown later when the properties of the transition response to an incident wavefield as a function of transition length are discussed. Not only is the amplitude increasing but the length of the coda with amplitudes above one third of the maximum peak to peak amplitude is also increasing. These seismograms are some of the strongest evidence for the concentration of amplitude at the surface of the crust as the wavefield passes through the transition. They also illustrate how the nature of the waveforms change as the wavefield passes through the transition.

A series of time slices is shown in Figures 12 through 14. These time slices were recorded during the FE calculation for the twenty five kilometer long forward transition discussed earlier. The time slices are recorded at intervals of twenty five seconds beginning twenty five seconds after the initiation of the FE calculation. The time elapsed since the start of the FE calculation is shown for each time slice above and at the right end of that time slice. The dimensions of the illustrated grid are 365x90 nodes. The heavy lines outlining the grid show the bounds of the crustal layer, the bottom edge, and both end edges of the grid. The water layer is not outlined as no displacements take place within it. For this calculation sixty forcing functions were used. Thus all displacement input to the grid through the leftmost grid edge is within the crustal layer. The cutoff for minimum amplitude to be plotted on each time slice is two percent of the maximum amplitude within that time slice. The arrow above each time slice except the first shows the location to which the component of the wavefield with velocity 2.8 km/s, seen at the leftmost edge of the grid in the previous time slice, has moved in the time elapsed since the previous time slice.

Figure 12 shows the first two time slices, which illustrate the wavefield approaching the transition region within the grid through the plane layered continental structure. In the first time slice the displacements which are seen entering the grid are

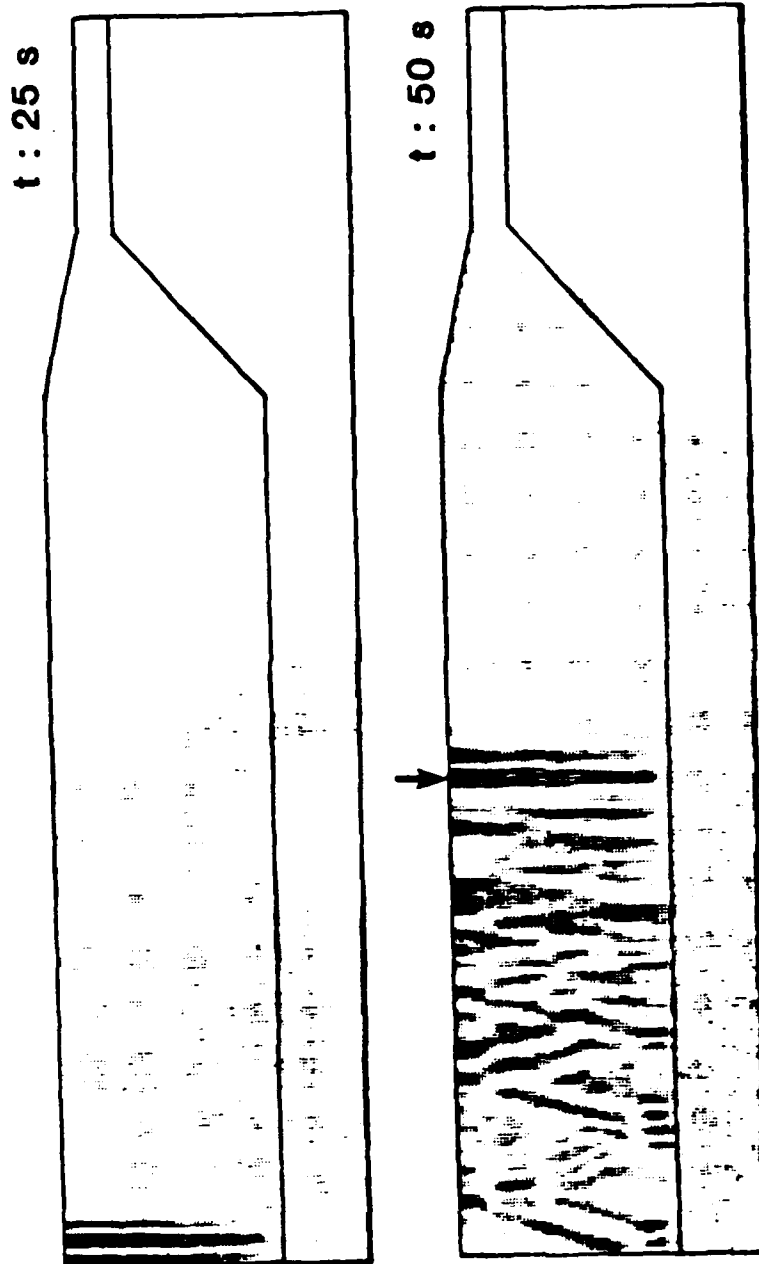


Figure 12: Time slices recorded during the 25 km forward transition calculation. The crustal layer and the ends and bottom of the FE grid which contain it are outlined. Within these outlines the displacements at each grid point at the indicated instant of time are plotted at the location of that point. A larger displacement produces a larger point. Thus, high displacement areas appear darker. The maximum amplitude in each time slice produces a point of maximum size. An amplitude of less than 2% of this maximum produces no point. The time since the initiation of the FE calculation is shown above the right end of each grid. The arrow above a time slice shows the location to which the disturbances moving at 2.8 km/s, seen at the left end of the previous time slice, have moved in the intervening duration.

equivalent to the largest peak to peak amplitudes in the seismograms. The dark, almost vertical lines show the same displacements seen in the seismograms as the highest amplitude initial peaks. The light grey areas seen to the right of the dark vertical linear areas are very low amplitude disturbances that precede the large arrivals in the seismograms. The second time slice shows the same high frequency arrivals after they have propagated about halfway through the plane layered portion of the transition grid. In this time slice more of the wavefield can be seen. As more of the wavefield enters the grid triangular regions of maximum amplitude become visible.

Figure 13 shows the next two time slices in the sequence which illustrate the passage of the highest amplitude portions of the wavefield through the transition region. In the third time slice, the first shown in this figure, the dark linear vertical region at the beginning of the wavefield has passed about halfway through the transition region. Comparing the portion of the wavefield visible within the grid in the second time slice with the same portion in the third time slice shows that the normalized amplitudes of all the displacements have been reduced in the third time slice with respect to the first two. This is evidence that the maximum amplitudes seen within the transition region are considerably larger than the displacements in the unperturbed layer over a half-space wavefield. As the high amplitude disturbance passes through the transition the maximum amplitude along the crust ocean boundary is most strongly amplified, and the dependence of amplitude on depth becomes more pronounced, since the amplitude near the depth of the base of the continental crustal layer is reduced. The sections of the wavefield present in both the third and fourth time slices are much more prominent in the fourth time slice. This is because the highest amplitude region of the wavefield, seen within the transition in the third time slice, has propagated past the rightmost edge of the grid. Thus, the maximum amplitude in the fourth time slice is much smaller than in the third. Figure 14 shows an additional time slice. Again the

amplitude has been reduced with respect to the previous time slice and the portion of the wavefield visible in both slices is amplified in the fifth time slice. The wavefield continues to show triangular regions of maximum amplitude. The extent of each triangular region, in the x direction, increases for regions of the wavefield incident on the left end of the grid at a later time.

The triangular pattern of maximum amplitudes in the wavefields can easily be explained. Let the SH L_g energy in the crustal layer be interpreted in terms of being the superposition of the constructive interference of post-critically reflected multiple SH wave reflections. The critical angle, the minimum angle between the ray and the normal to the boundary for which total internal reflection occurs, is about fifty one degrees. Since the wavefront can be considered to be perpendicular to the ray, the wavefronts that are visible as the triangular regions of maximum amplitudes can be expected to show angles of incidence with the boundary of between 0° and 39° . In the first two time slices the angles of incidence range between 0° and 25° . In the third time slice the angles of incidence of the wavefronts at the layer boundary reach 35° , in the fourth time slice they reach 38° . The superimposed triangular regions of maximum amplitude are seen to increase in average width as the left edge of the grid is approached in any given time slice, that is, as portions of the wavefield incident on the left grid edge at later times are considered. This increase in width of the triangular maxima corresponds to an increase in phase velocity which can be translated to a increase in period and/or a larger contribution from higher modes. Thus, the higher frequency content at the beginning of the seismogram is also clearly visible in the time slices. The later parts of the seismogram are predominantly of longer periods and contain more higher mode energy.

It can be seen that some energy is leaking into the half-space even in the plane layered region, this leakage is small and cannot be seen in the seismograms in this

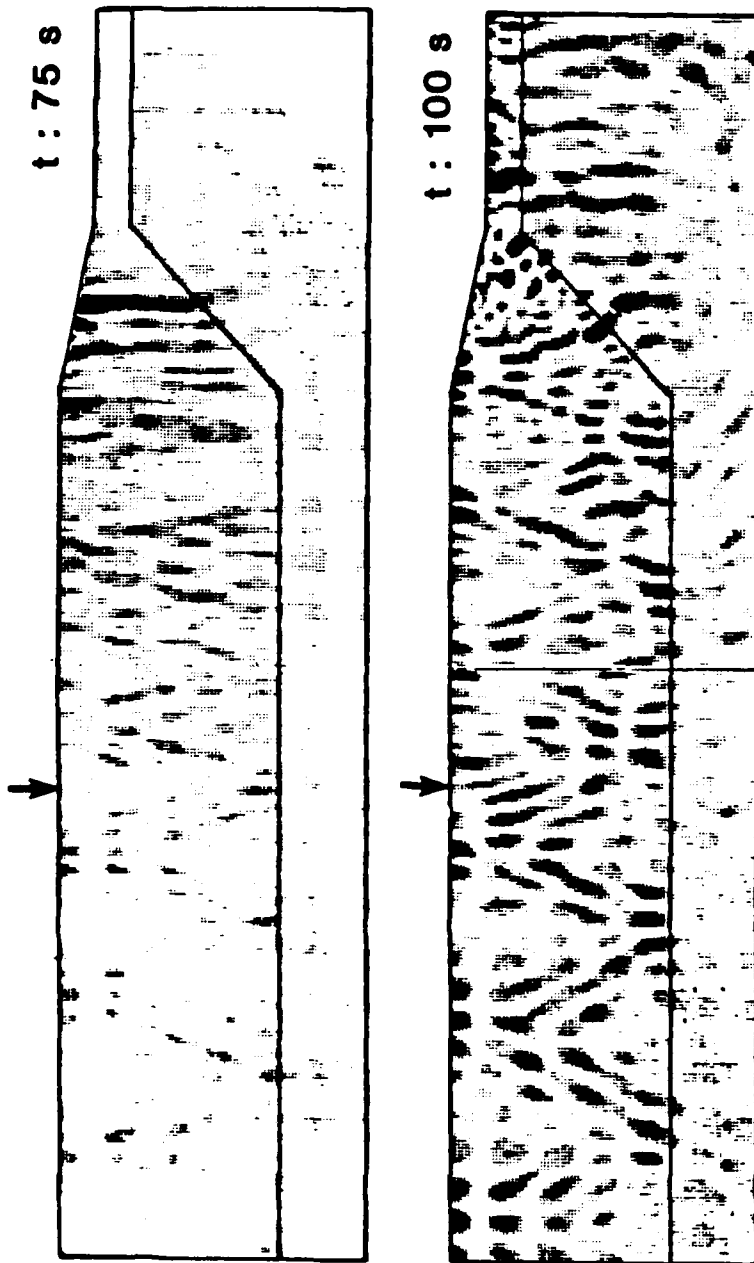


Figure 13: Time slices recorded during the 25 km forward transition calculation. Details of the form of these time slices are the same as for Figure 12. The time slices in this figure are recorded after the completion of additional time steps in the same FE calculation that produced the time slices in Figure 12.

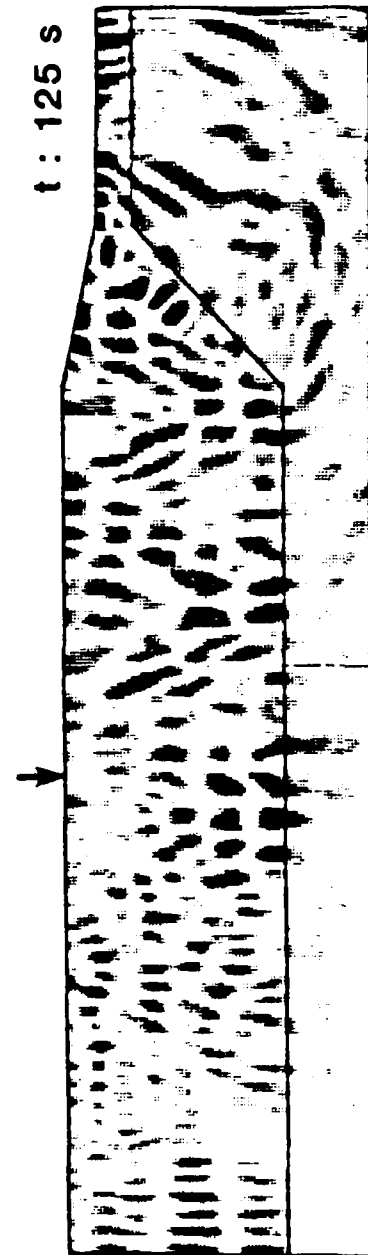


Figure 14: Time slice recorded during the 25 km forward transition calculation. Details of the form of these time slices are the same as for Figure 12. The time slices in this figure are recorded after the completion of additional time steps in the same FE calculation that produced the time slices in Figure 12 and 14.

example. However, in the layer over a half-space reference model the time slices show this leakage is largest closely following the maximum amplitude regions, seen as the dark vertical lines in the first two time slices. The extent of the low amplitude disturbance produced by this leakage increases with distance propagated through the grid. The region of the seismogram corresponding to this region of the wavefield where leakage is maximum is the region in which small discrepancies are seen between synthetics and FE results for large propagation distances in the grid. The observation of amplitude passing into the half-space helps explain why some small waveform changes can be seen.

When regions of the wavefield with large amplitudes pass through the transition region, amplitude can be seen crossing the crust mantle boundary particularly adjacent to the high amplitude regions within the crustal layer of the transition region. The energy crossing the boundary produces regions of significant amplitudes that are visible in the oceanic half-space both in the transition region and in the region of oceanic structure. In the region of this oceanic half-space corresponding in depth to the continental crust two main effects on the propagating amplitudes can be seen. First, as x increases, the highest amplitude regions in the half-space which form at the intersections of the wavefronts with the crust mantle boundary in the transition region, are propagating at some angle away from the crustal layer toward the bottom boundary of the grid. The component of the motion towards the bottom boundary increases as the width of the triangular regions of maxima in the incident wavefield increases. Thus, as the angle between the wavefront and the crust mantle boundary in the continental crustal layer decreases the maximum amplitude regions crossing the crust mantle boundary in the transition region propagate to the grid bottom while traveling a shorter horizontal distance. The high amplitude regions in the half-space of the oceanic structure propagate towards the bottom boundary of the grid more rapidly for

the energy later in the incident wavefield. Second, energy is escaping from the high amplitude regions in the crustal layer as they propagate through the oceanic crustal layer. This energy forms a forward bending arc in the mantle half-space, due to the higher velocity in that half-space, that connects to the energy which escaped from the same portion of the wavefield when the wavefield passed through the transition to the bottom of the half-space. As the high amplitude regions of the wavefield propagate more directly towards the grid bottom the tails forming due to leakage from the oceanic crustal layer become fainter and detach from the high amplitude downward traveling portions of the wavefield.

To explain the observations made of the time slices the ray diagrams shown in Figure 15 are useful. This figure shows two transition structure outlines identical to those used to accentuate the structure on the time slices. The lines within these outlines show three multiply reflected rays, for angles of incidence, i , at the crust mantle interface of the continental structure of 55° , 65° , and 75° respectively, and the effect of the forward transition region on each. The angles chosen give a good sampling of the possible post-critical range of incident angles ($>51^\circ$). The arrows on the rays show the directions of propagation. The triangular regions of high amplitude in the time slices show the wavefronts which are perpendicular to the rays shown in Figure 15.

The upper transition shows the ray paths when the rays encounter the crust mantle boundary of the transition before the crust water boundary. When these rays pass into the transition region their incident angles, i , at the crust mantle interface in the continental structure are reduced by the angle, ϕ_{CM} , to give their incident angles, $j = i - \phi_{CM}$, at the crust mantle boundary. This angle of incidence, j , allows transmission into the mantle layer when $j < 51^\circ$. The angle between the transmitted ray and the normal to the crust mantle boundary, shown in the figure as a dashed line, is j' .

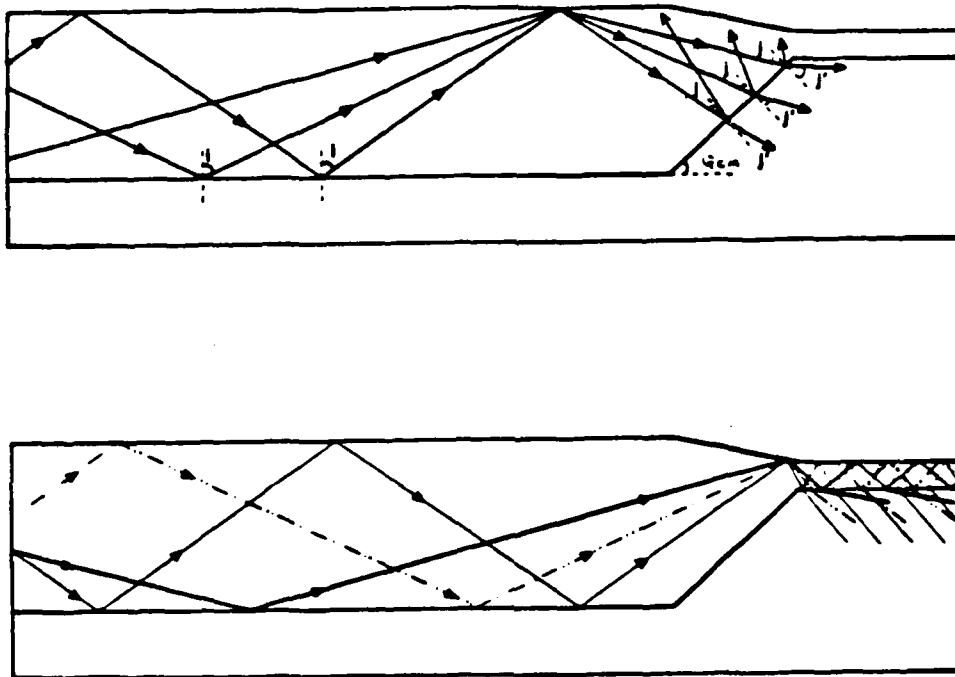


Figure 15: Illustration of ray paths within a forward transition structure. Each diagram shows rays with angles of incidence, i , 55° , 65° , and 75° , at the free surface and crust mantle interface in the continental portion of the model. The transition structure within which the rays are traveling is a 25 km forward transition drawn to scale. The upper diagram shows propagation paths for rays that encounter the crust mantle boundary before the crust water boundary. The lower diagram shows propagation paths for rays that encounter the crust ocean boundary only as they pass through the transition region. The arrows indicate the direction of propagation of the wavefront along the ray.

The angle, $j' = \sin^{-1} \left(\sin j \frac{V_M}{V_C} \right)$, increases as the angle, j , increases and the portion of the incident amplitude transmitted across the crust mantle boundary decreases. Thus, as the angle i increases the fraction of the incident amplitude transmitted into the half-space decreases and the resulting regions of high amplitude in the half-space travel across the crust mantle boundary more horizontally. It follows that as the angle of incidence of the wavefront at the crust mantle interface of the continental structure increases the wavefield propagates more directly towards the base of the grid as it crosses the crust mantle boundary. This explains the increase in z component of propagation in the half-space as the calculation proceeds and the incident energy is of higher phase velocity and period. The rays reflected from the crust mantle boundary are reflected back toward the source for angles of incidence at the crust mantle boundary less than twice ϕ_{CM} . For reflections points immediately preceding the beginning of the transition region rays can propagate through the transition region without interacting with either boundary within the transition and then propagate with unchanged angles of incidence through the oceanic crustal layer.

The lower transition shows the ray paths when the rays encounter the crust ocean boundary before they encounter the crust mantle boundary. For reflection points close to the end of the transition reflected rays are transmitted directly into the oceanic crustal layer. The same angles of incidence at the crust mantle interface in the continental structure are used as in the previous example. These angles of incidence in the continental crustal layer yield angles of incidence $j = i - \phi_{CO}$ in the oceanic crustal layer. The illustrated paths show one way modes which are not of appropriate frequencies to be trapped within the oceanic crustal layer enter that layer. They produce multiply reflected rays at pre-critical angles within the oceanic crust and demonstrate why amplitude is seen crossing the crust mantle boundary in the oceanic structure following the transition. They also explain why this leakage is

maximum near the transition and decreases as the distance from the transition increases. If, at each successive reflection at the crust mantle interface the transmission coefficient is T , then the amount of transmitted amplitude for the n^{th} bounce is $(1-T)^{n-1}TA$, where A is the original amplitude, and T is less than one. Clearly, the amount of escaping energy decreases with distance. Rays that pass through the transition without encountering any boundary can be directly converted to oceanic modes and continue to bounce with the same post-critical angles of incidence at the crust mantle interface and the free surface as they did in the continental structure. Rays that reflect from the crust ocean boundary then from the crust mantle boundary have angles of incidence of $i - \phi_{CM} - 2\phi_{CO}$ at the crust mantle boundary. If this angle is less than twice ϕ_{CM} then the ray is reflected back towards the source. If the angle is larger than this value then pre-critically reflected rays in the oceanic crustal layer, with angles of incidence $i - 2\phi_{CM} - 3\phi_{CO}$ are produced.

Changes to L_g Wavetrains on Passage through a Reverse Transition Region

The passage of a wavefield consisting of SH type L_g mode sum energy for a continental layer over a half-space model, which has passed through a forward transition of fifty kilometers length, through a reverse transition such as that illustrated in Figure 1b) has several effects on the wavefield. These effects are illustrated in Figures 16 through 21. The figures show several important properties. Again, behavior along the ocean continent boundary shows distinct differences when compared to the behavior along the mantle crust boundary. Along the surface of the oceanic crustal layer amplitudes decrease with distance, Δ . Along the surface of the crustal layer in the transition region amplitudes are seen to decrease with distance, Δ , even more rapidly than along the oceanic crustal surface. No energy is propagated from the ocean layer into the continental crustal layer. Energy incident from the oceanic crustal layer travels

up the surface the ocean crust transition while the distribution with depth of amplitude changes considerably. The concentrations of amplitude within the oceanic crust distribute themselves throughout the entire continental crustal layer. Amplitude seems to travel up the ocean crust boundary more readily than it spreads into the lower section of the continental crust. Amplitude incident on the mantle crust boundary appears to be primarily transmitted into the continental crustal layer. As the wavefield exiting the transition propagates through the continental structure the distribution of amplitude with depth continues to readjust thus reducing the surface amplitudes. Each of these observations will be discussed in detail below and supporting results will be shown in the figures.

First, the results of a sample calculation with a transition length of twenty five kilometers will be discussed. The geometry of the grid containing this transition region is illustrated, to scale, in Figure 16. The heavy line labeled A at the left end of the grid represents the column of nodes constrained to move according to the time histories recorded twenty five kilometers beyond the right end of the forward transition region shown in Figure 9. These time histories result from recording the wavefield after passage through the forward transition due to SH L_g mode sum seismogram forcing function applied to the right end of that transition. The two vertical lines labeled Rc1 and Rc2 show receiver depth sections used to illustrate the effects of the transition on the distribution of amplitude with depth. The upper hatch region shows the ocean layer, the lower hatched region shows the mantle layer, and the unhatched region shows the crustal layer. Dots on Rc1 and Rc2 indicate positions of receivers for which displacement time histories are illustrated in Figure 17. Open circles and dots located on the surface of the crustal layer refer to a surface section of nodes for which displacement time histories are illustrated in Figure 18.

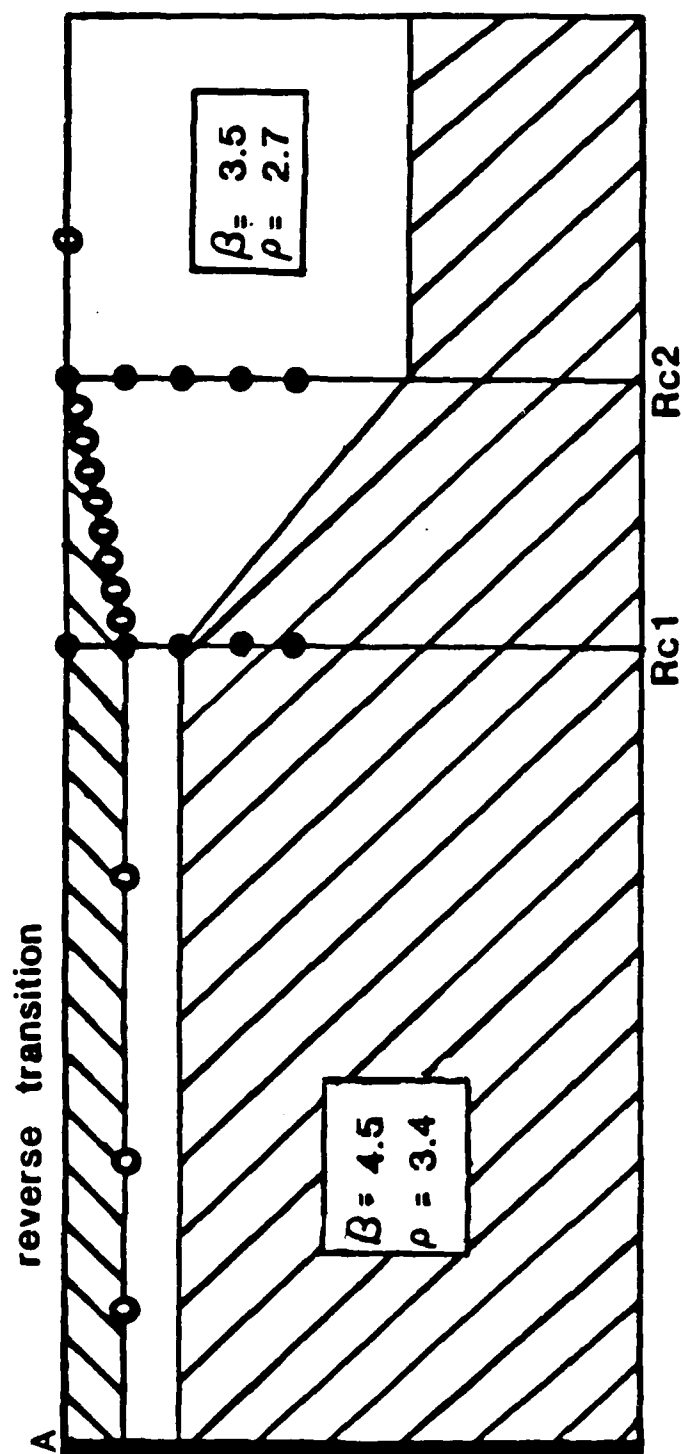


Figure 16: Grid geometry for the 20 km reverse transition used to illustrate the effects of a forward transition on the waveforms and amplitudes of seismograms as a function of distance, Δ , and depth. The upper hatched region is the oceanic layer, the lower hatched region the mantle layer, and the unhatched region the crustal layer. The heavy vertical line labeled A shows where seismograms recorded in the forward transition calculation are applied as forcing functions. The vertical lines labeled Rc1 and Rc2 show depth sections of receivers. The dots on Rc1 and Rc2 show receivers for which seismograms are illustrated in Figure 17. The open circles along the surface of the crustal layer show the receivers for which seismograms are shown in Figure 18.

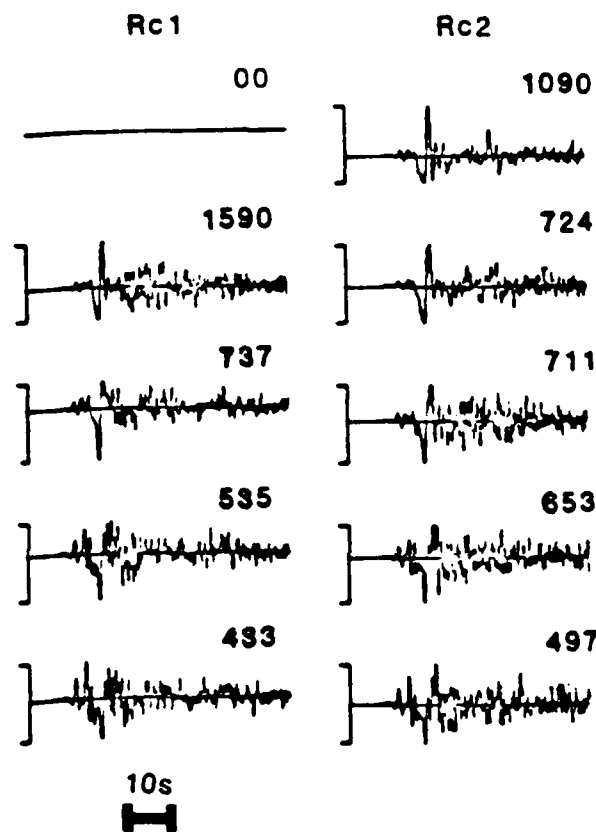


Figure 17: Seismograms recorded at receivers shown as dots on depth sections Rc1 and Rc2 in Figure 16. The first column shows the seismograms recorded at Rc1, the second the seismograms recorded at Rc2. The numbers above the right end of each seismogram show the peak to peak amplitude. The first row of seismograms show receivers at the depth of the surface of the continental crust. Successive rows show pairs of receivers at increasing depths. The second row is at the depth of the surface of the oceanic crust, the third at the depth of the base of the oceanic crust. All receivers illustrated are above the base of the continental crust.

Figure 17 shows seismograms recorded at positions shown as dots in Figure 16. All seismograms are band pass filtered between .01 and 1.0 Hz. No instrument is applied. The first column of seismograms in this figure shows the changes to waveform and amplitude as a function of depth at distance Rc1. The second column shows the seismograms illustrating the same type of variations on depth section Rc2. The numbers above and to the right of each seismogram show the maximum peak to peak amplitude of each seismogram. The surface seismogram on section Rc2, the first seismogram in the second column, shows a 25% decrease in peak to peak amplitude when compared to the surface seismogram in column Fc1 of Figure 10. Thus, even without considering attenuation, transmission of L_g type waves from continental to oceanic to continental structures can reduce the surface amplitudes by twenty five percent. At the depth of the surface of the oceanic crustal layer, the second row in this figure, propagation through the transition reduces the peak to peak amplitude by more than a factor of two. At depths between the surface of the continental crust and the depth of the surface of the oceanic crust the decay of amplitude with depth decreases with depth. The amplitude concentrated in the oceanic crust also spreads into the continental crustal layer below the oceanic crustal layer. The last two pairs of seismograms in this figure are recorded at depth below the bottom of the oceanic crust and above the bottom of the continental crust. Propagation across the transition at these depths produces an increase of about twenty percent in peak to peak amplitude. An increase in the amplitudes of the coda with respect to the maximum amplitude is also observed, giving an increase in RMS amplitude of about thirty five percent. Clearly, most or all of the amplitude incident on the mantle crust boundary is transmitted into the continental crustal layer, and the increase in amplitude is due to energy previously concentrated in the oceanic crust spreading throughout the continental crust within the transition region. These results support the statements that

energy incident from the oceanic crustal layer travels up the surface of the ocean crust transition, and that the concentrations of amplitude within the oceanic crust distribute themselves throughout the continental crustal layer on passage through the reverse transition and the first kilometers of the continental structure. It is also clear that amplitudes incident on the mantle crust boundary are largely transmitted across it into the crustal layer. The actual distortions of the wavefield will be cleared when the time slices, Figures 19 through 21, are discussed.

Figure 18 shows seismograms recorded along the surface of the crust, shown in Figure 16 as open circles and as dots on the crustal surface at distances Rc1 and Rc2. The numbers to the left of each seismogram show the sequence, in space, in which the seismograms were recorded. Seismogram 1 was recorded at the leftmost surface receiver, the leftmost open circle on the oceanic crustal surface in Figure 16. The number used as a label increases as one moves to the right across Figure 16. Peak to peak amplitudes are shown as the numbers above and to the right of each seismogram. A clear decrease in peak to peak amplitudes is seen as one moves along the surface of the oceanic crustal layer approaching the transition region. The amount of this reduction in amplitude is becoming smaller per unit distance as the wavefront travels through the oceanic portion of the model. Not only are the peak to peak amplitudes being reduced, but the portion of the coda with amplitudes comparable to the maximum amplitude is being reduced in length. Thus, the RMS amplitude decreases faster than the peak to peak amplitude. As the wavefront enters the transition region the decay of amplitude as a function of the distance, Δ , is accelerated. Although the decrements in amplitude appear to be smaller in the transition region than in the crustal layer of the oceanic structure, examining Figure 16 shows that the distance between the receivers in the transition region is one eighth of the distance between those on the surface of the oceanic layer. Thus, the decay per unit distance in the

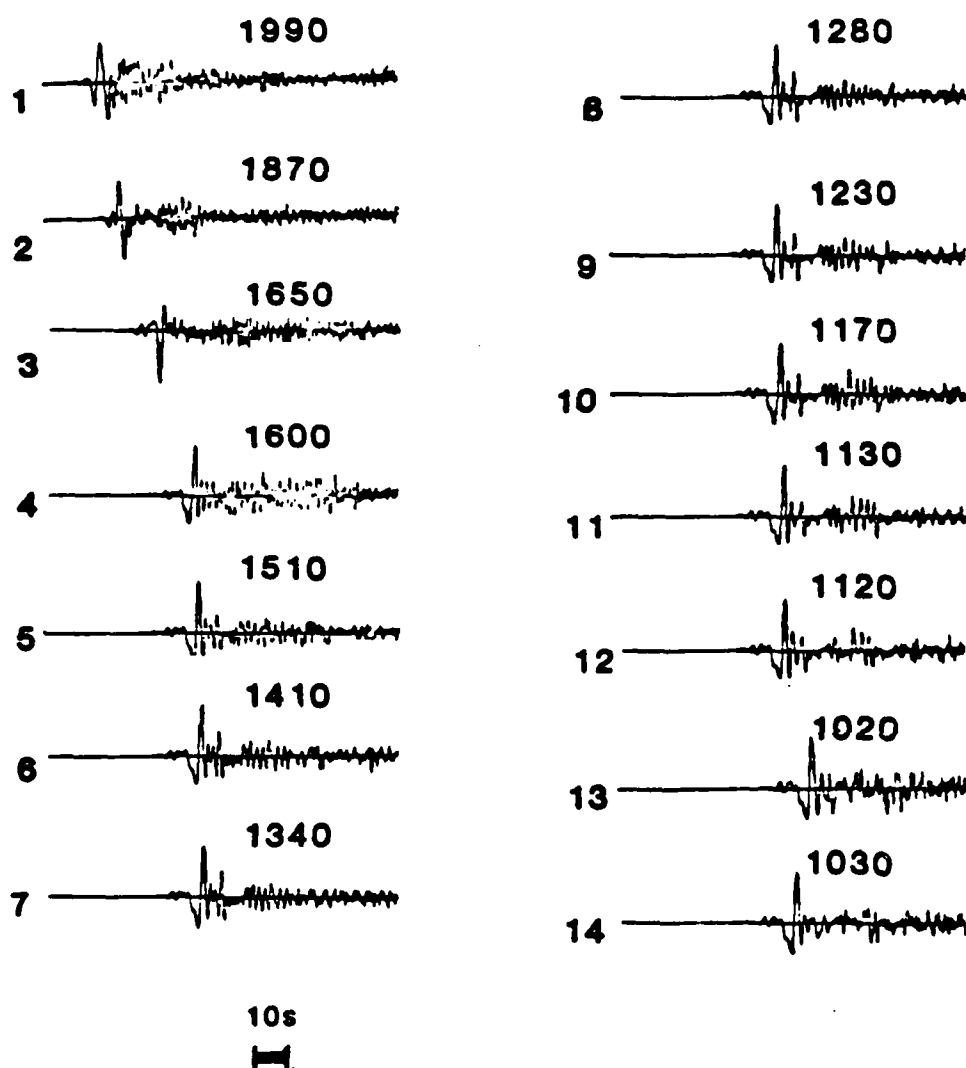


Figure 18: Seismograms recorded at receivers along the surface of the crustal layer in a reverse transition calculation. These seismograms are recorded at the receivers shown as open circles and dots on the surface of the crustal layer in Figure 16. The numbers to the left of each seismogram indicate the location of the node at which that seismogram is recorded. The leftmost open circle is receiver 1. The numbers increase as one moves to the left along the surface of the crustal layer. The numbers above the right end of each seismogram give the peak to peak amplitude of that seismogram.

transition is a factor of two to eight larger than in the oceanic structure. The amplitude decay within the transition is monotonic. The rate of decay is not necessarily constant showing some tendency to become smaller towards the end of the transition. A slight peak to peak amplitude increase is seen as the wave travels through the first kilometers of the continental structure. However, the RMS amplitude continues to decrease slowly until the wavefield readjusts to the new structure.

It should be noted that the continuation of the forward transition calculation by coupling results recorded during that calculation into the reverse transition grid calculation does introduce some uncertainties in the results. First, sixty of ninety nodes at the leftmost edge of the reverse transition grid have forcing functions applied to them. This vertical truncation of the incoming wavefield will have some effect. Also, any reflections included in the seismograms recorded to use as forcing functions will be added to the forward propagating wavefield in the reverse calculation. These effects tend to increase the amplitudes at the surface of the oceanic layer near the left end of the grid. In this region results are available at the same physical locations in both forward and reverse transition grids. An example of a seismogram recorded at the same physical position but at different nodes in the two transition grids the first seismogram in Figure 18 and the eleventh seismogram in Figure 9 can be compared. The latter portion of the seismogram shown in Figure 9 is contaminated with reflections and should be ignored. Comparing the first twenty seconds of these two seismograms shows that the amplitude is increased when the coupling procedure is used. Examining other common results shows that the discrepancy seen in this example is much larger than average, but agrees in sign with other points. Thus, the uncertainties introduced by the coupling process appear to increase the amplitudes in the second grid by about three percent. Therefore, they could possibly lead to a slight underestimate of the magnitude of the attenuation effect, but should not lead to an

overestimate. Propagation through a fifty kilometer forward transition followed by 120 km of oceanic structure followed by a fifty kilometer reverse transition reduces the amplitudes at the surface by at least twenty five percent.

A series of time slices is shown in Figures 19 through 21. These time slices were recorded during the FE calculation for the fifty kilometer long reverse transition discussed earlier. The time slices are recorded at intervals of 12.5 seconds beginning 37.5 seconds after the initiation of the FE calculation. The time elapsed since the start of the FE calculation is shown for each time slice above and at the rightmost end of that time slice. The dimensions of the illustrated grid are 450x90 nodes. The heavy lines outlining the grid show the bounds of the crustal layer, and the horizontal and vertical extent of the grid. The water layer is not outlined. No displacements take place within it. Again, sixty forcing functions, this time recorded in the fifty kilometer forward transition calculation, are applied to the left end of the grid. Thus input forcing functions extend to three times the depth of the bottom of the crustal layer, or to six crustal layer thicknesses below the water surface. The cutoff for minimum amplitude to be plotted on each time slice is two percent of the maximum amplitude in that time slice. The arrow above each time slice except the first shows the location to which the component of the wavefield traveling at 3.5 km/s seen at the leftmost edge of the grid for the previous time slice has moved in the time elapsed since the previous time slice.

Figure 19 shows the first two time slices, which illustrate the wavefield traveling through the oceanic layer over a half-space structure. In the first time slice the leading edge of the wavefield has propagated about halfway through the oceanic structure, in the second the leading edge of the wavefield is about to enter the reverse transition. The high amplitude concentrations in the oceanic crust travel slower than the lower amplitude disturbances in the half-space. Triangular regions of maxima can be seen but they are not nearly so clear as in the case of the wavefield seen in the forward

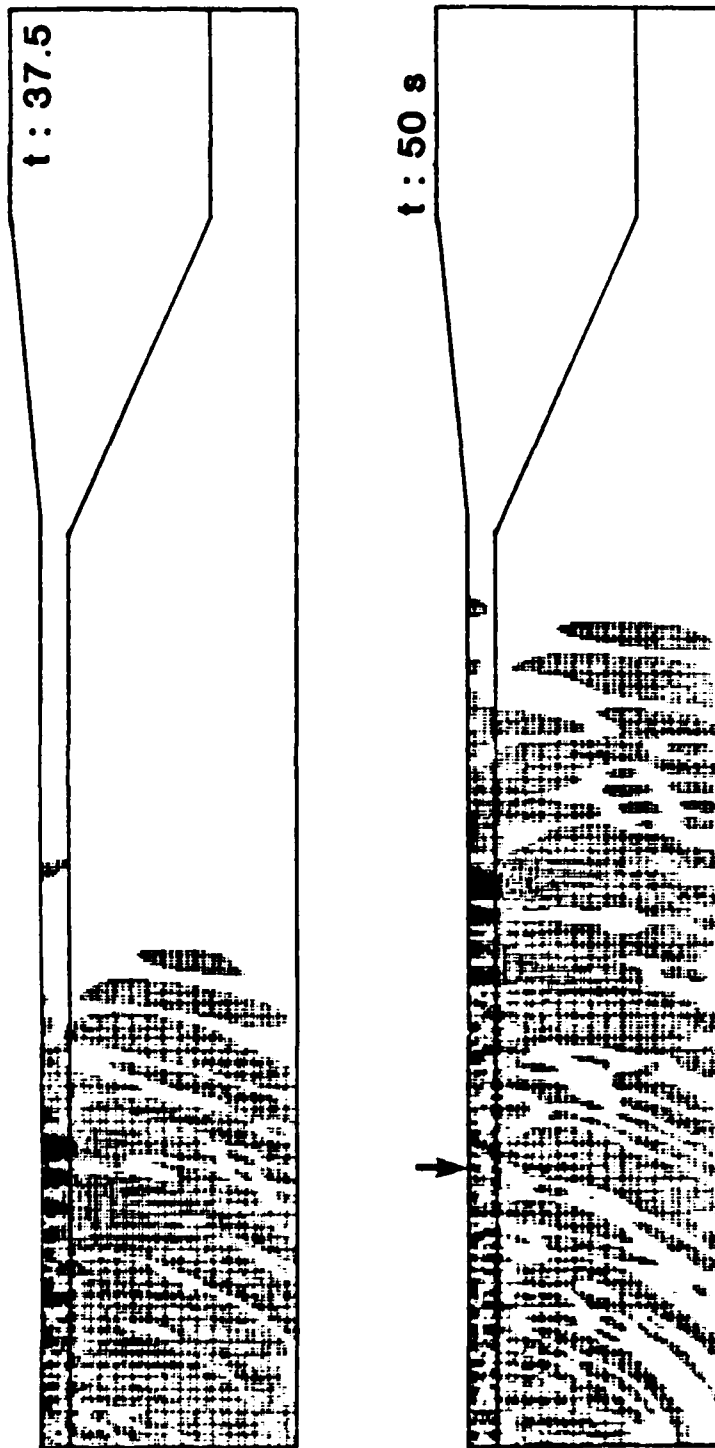


Figure 19: Time slices recorded during the 50 km reverse transition calculation. The crustal layer and the ends and bottom of the FE grid which contain it are outlined. Within these outlines the displacements at each grid point at the indicated instant of time are plotted at the location of that point. A larger displacement produces a larger point. Thus, high displacement areas appear darker. The maximum amplitude in each time slice produces a point of maximum size. An amplitude of less than 2% of this maximum produces no point. The time since the initiation of the FE calculation is shown above the right end of each grid. The arrow above a time slice shows the location to which the disturbances moving at 3.5 km/s, seen at the left end of the previous time slice, have moved in the intervening time.

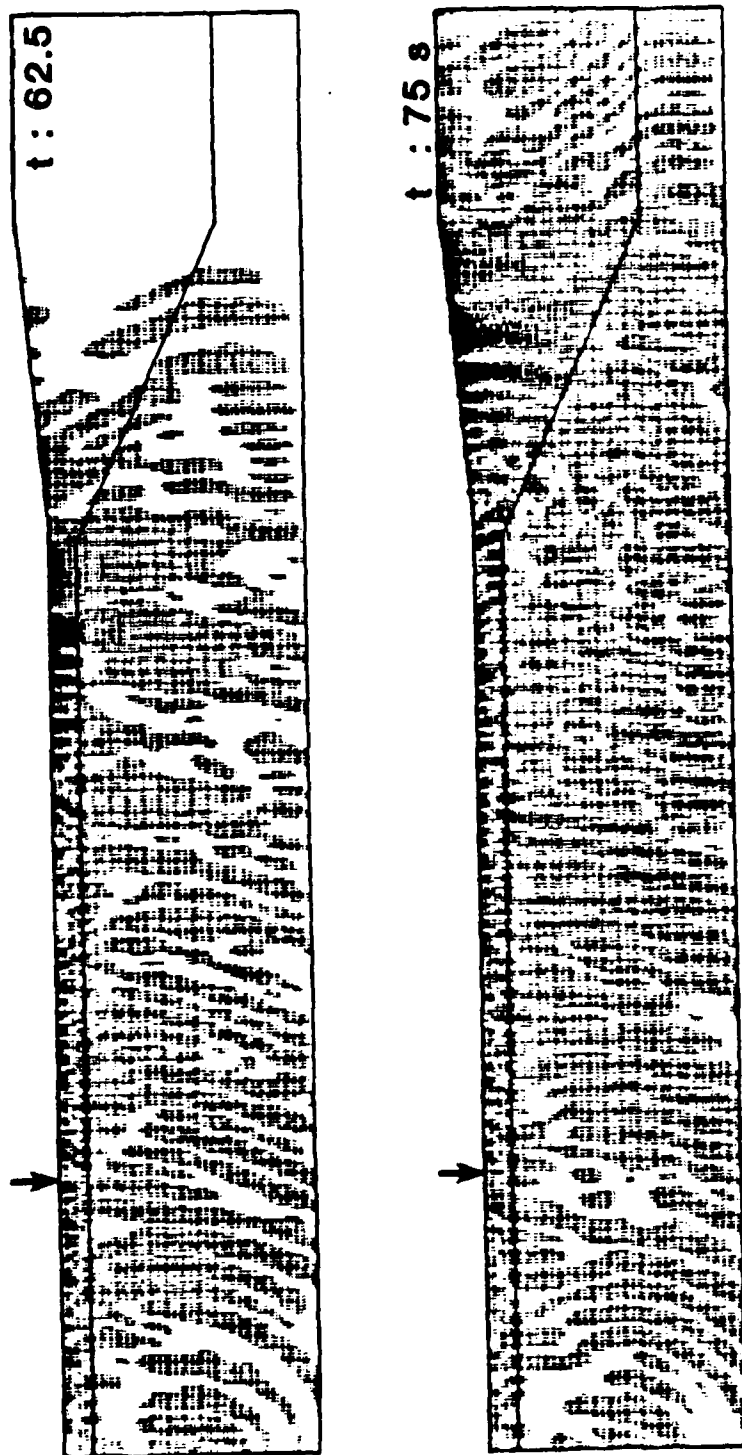


Figure 20: Time slices recorded during the 25 km forward transition calculation. Details of the form of these time slices are the same as for Figure 19. The time slices in this figure are recorded after the completion of additional time steps in the same FE calculation that produced the time slices in Figure 19.

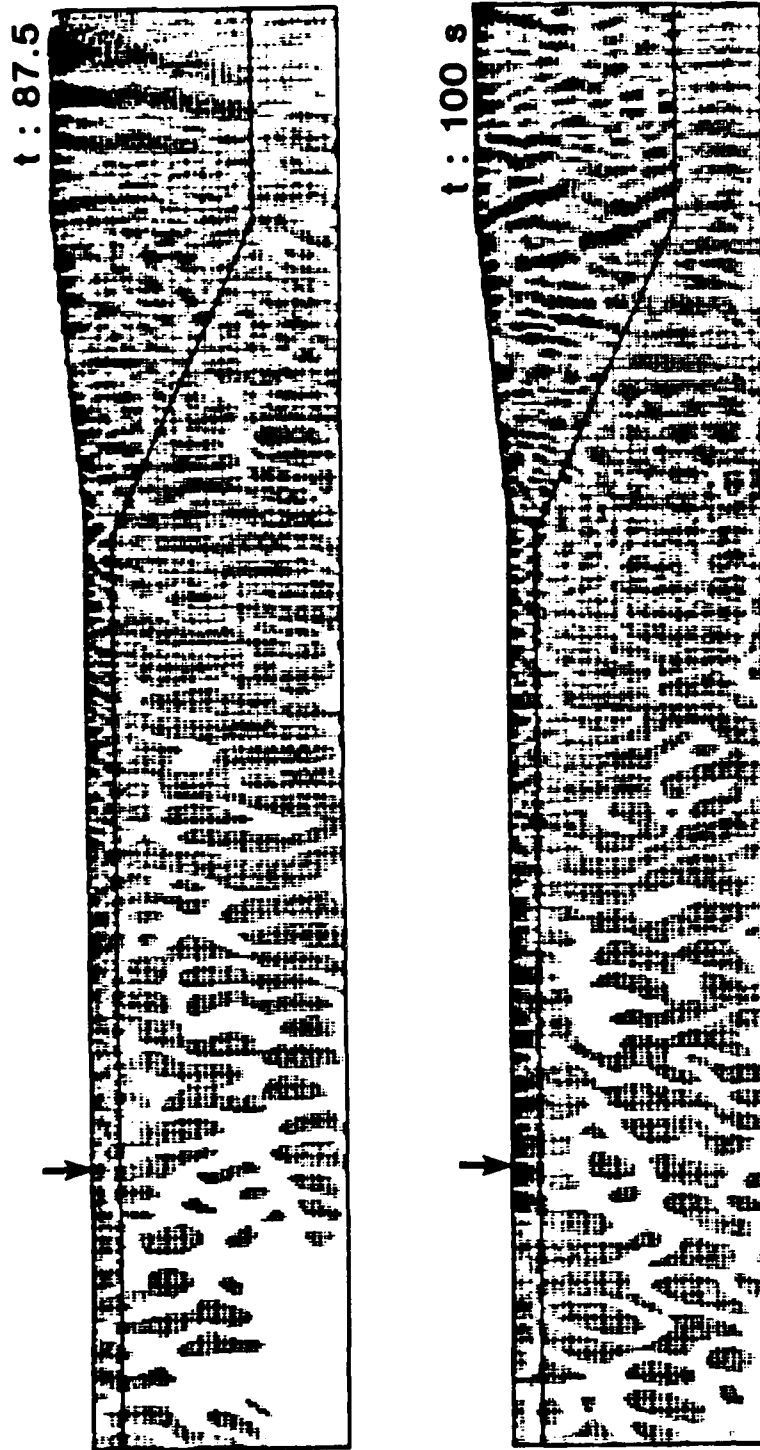


Figure 21: Time slice recorded during the 25 km forward transition calculation. Details of the form of these time slices are the same as for Figure 19. The time slices in this figure are recorded after the completion of additional time steps in the same FE calculation that produced the time slices in Figure 19 and 21.

transition. Some of the regions of displacement within the half-space are larger in the second time slice than in the first. This growth is due mainly to a reduction in the maximum amplitude. Some of the clear shape changes in these areas are due to propagation effects.

Figure 20 shows the next two time slices in the sequence. Figure 21 shows the two time slices following those shown in Figure 20. The time slices in Figure 20 illustrate the passage of the highest amplitude portions of the wavefield through the transition region. The time slices in Figure 21 show the propagation of the highest amplitude portions of the wavefield through the continental structure at the end of the grid, and the propagation of later portions of the wavefield through the transition region. In the third time slice, the uppermost in Figure 20, the maximum amplitude has been slightly reduced with respect to the second time slice, but the differences in the wavefield due to this amplitude reduction is small. In the fourth time slice, however, the maximum amplitude has been significantly reduced. Thus, the remainder of the wavefield has been amplified. This reduction of maximum amplitude illustrates that the regions of maximum amplitude passing through the transition region are spreading to include all depths in the continental crustal layer and are thus being reduced in amplitude at any particular node. This decrease in maximum amplitude in the fourth time slice accounts for many of the enlargements of the disturbances seen in the oceanic half-space when the third and fourth time sections are compared. The fifth time slice, the uppermost in Figure 21, has maximum amplitude somewhat smaller than the fourth time slice. The differences do not produce significant changes in the lower amplitude portions of the wavefield. However, the sixth time slice shows a substantially amplified wavefield since the initial maximum amplitude disturbances have propagated out of the grid. The triangular regions of maxima are beginning to appear in the continental structure. Additional propagation in x in the continental structure may

be needed to stabilize the wavefield in the region of the grid with continental structure. Examining these time slices verifies that very different kinds of effects occur along the ocean crust boundary and along the mantle crust boundary. It also shows that due to propagation into the half-space at an angle to the crust mantle boundary in the forward transition some energy in the reverse transition calculation is propagating out of the bottom of the grid. These different effects will be discussed separately below.

Regions of significant amplitude incident on the mantle crust boundary are transmitted across it. In the third and fourth time slices the reflection from this boundary are too small to be seen. The pattern of the displacements seen in the oceanic half-space is significantly distorted by transmission across the mantle crust boundary. The uppermost portion of a disturbance crosses the boundary first and begins to move more slowly. The remainder of the disturbance, still in the mantle layer continues to move with the mantles faster velocity. As the disturbance moves through the length of the transition, an increasing section of it moves into the crustal layer. This results in a slope being superimposed on the portion of the disturbance which has propagated back into the crustal layer. This slope is dependent of the length of the transition, l , the velocity in the crustal layer, v_c , and the velocity in the mantle slope clearly visible in both the third and the fourth time slices ahead of the layer, v_M , $\text{Slope} = \tan^{-1} \left[\frac{l(v_M - v_c)}{v_M} \right]$. In this case the angle is about fifty two degrees. This region of the wavefield with largest amplitudes. This pattern is also seen in the fifth and sixth time slices shown in Figure 21. In these time slices the amplitude incident from the oceanic crustal layer dominates that transmitted from the oceanic mantle layer.

The effect of the reverse transition region on the energy previously traveling in the oceanic crustal layer is very different. A concentration of amplitude leaving the oceanic crustal layer propagates along the ocean crust boundary. While it propagates along this boundary the lower edge of the amplitude concentration is no longer constrained as trapped modes by the lower edge of the oceanic crustal layer. Consequently, amplitude can migrate downwards within the crustal layer of the transition and in the crustal layer of the continental structure following the transition region. The small concentrations in amplitude traveling along the ocean continent boundary in the third time slice show little change in form. The amount of amplitude escaping from them is smaller than the low amplitude cutoff imposed on the plot. In the fourth time slice the maximum amplitude regions have propagated to the center of the transition region and spread throughout the depth range above the depth of the bottom of the oceanic crust. Some evidence is visible that some amplitude has been translated to depths below the oceanic crust. In the fifth time slice, shown in Figure 21, The maximum amplitude regions have propagated to the rightmost end of the grid. In this time slice it is clear that the amplitude previously confined to the oceanic crustal layer has distributed itself throughout the entire depth range of the continental crust. Some transmission of amplitudes, spreading down from concentrations of amplitude originally trapped in the oceanic crustal layer, across the the crust mantle interface is also seen. The amplitudes are still much larger near the surface, and decay rapidly with depth.

The disturbances seen in the half-space of the oceanic region of the reverse transition grid contain significant energy but the amplified surface amplitudes make them appear small. Comparing the first two time slices shows that for a subset of these disturbances the component of motion in the z direction in the half-space is increasing for successive groups or disturbances. This tendency continues in the later sections.

These packets of amplitude propagate rapidly enough in z that some will pass across the bottom boundary of the grid before they reach the reverse transition region. The amount of energy that passes out of the grid in this way as the wavefield travels between the two transition regions is related to the angles of incidence of the wavefronts at the crust ocean and crust mantle boundaries in the forward transition region. For the case of a single reflection within the transition region the angle of incidence for a wavefront which first encounters the crust mantle boundary is $i-\phi_{CM}$, for a wavefront which first encounters the crust ocean boundary it is $i-\phi_{CO}$, where the angles mentioned are illustrated in Figures 1 and 16. When discussing the time slices for the forward transition these waves were also visible and were seen to travel at angles dependent on the phase velocity of the incoming waves. Adding the results seen in these time slices to those observed in the forward transition time slices to help interpret the problem shows that the direction is also a function of the length of the transition, and the amount of escaping energy is clearly dependent on the length of the intervening oceanic structure. Results supporting the existence of these effects will be discussed in detail and explained later.

The Dependence of Changes to L_g Wavetrains Passing through a Forward Transition Region on Transition Length

The forward transition tests using a variety of transition lengths illustrate several properties that change with the length the transition model or the slopes of the crust ocean and the crust mantle boundaries. At depths corresponding to the crust water boundary the amplitude of the reflected component of the seismograms traveling back into the continental crustal layer, that is back toward the source, decreases as the length of the transition increases. A similar reflected component is observed at depths corresponding to the crust to mantle boundary. The reflected amplitudes are much smaller with respect to the incident amplitudes for depths coincident with the crust

mantle boundary than at depths coincident with the crust ocean boundary. The difference in the magnitudes of the effects in these two depth ranges will be explained by the difference in velocity contrast across the two boundaries in the transition region and the difference in the angles ϕ_{CM} and ϕ_{CO} shown in Figure 1. Although no energy is transmitted into the water layer, not all energy impinging on the water layer is reflected back toward the source. Instead some of the energy is concentrated by the transition into the oceanic crustal layer. The amount of concentrated energy, increases as the length of the transition increases. Quantification of a similar concentrating effect associated with the crust mantle boundary is difficult because this effect is dominated by transmission of energy across that boundary. The amplitudes in the mantle layer within the transition region are maximum immediately below the crust mantle boundary, and decay nearly exponentially with depth below that boundary. The amplitude of the transmitted seismograms recorded at nodes below the oceanic crustal layer, at the end of the forward transition, decrease as the length of the transition increases. Despite this observation the time slices show that the amount of amplitude transmitted across the boundary increases as the length of the transition increases. The amplitudes of seismograms recorded at nodes along the surface of the crustal layer show a general increase as one passes through the transition. However, this increase does not appear to be monotonic. The variation in surface amplitude within the transition zone has similar pattern for all lengths of transitions, but the width of the oscillations are proportional to the width of the transition region. Each of these effects will be discussed and explained below.

The effects discussed above will be explained with the aid of Figures 15 and 22. Figure 22 illustrates two forward transition structure outlines for a one hundred kilometer transition region, at the same scale as the twenty five kilometer forward transition outlines used in Figure 15. The lines within each of these four outlines

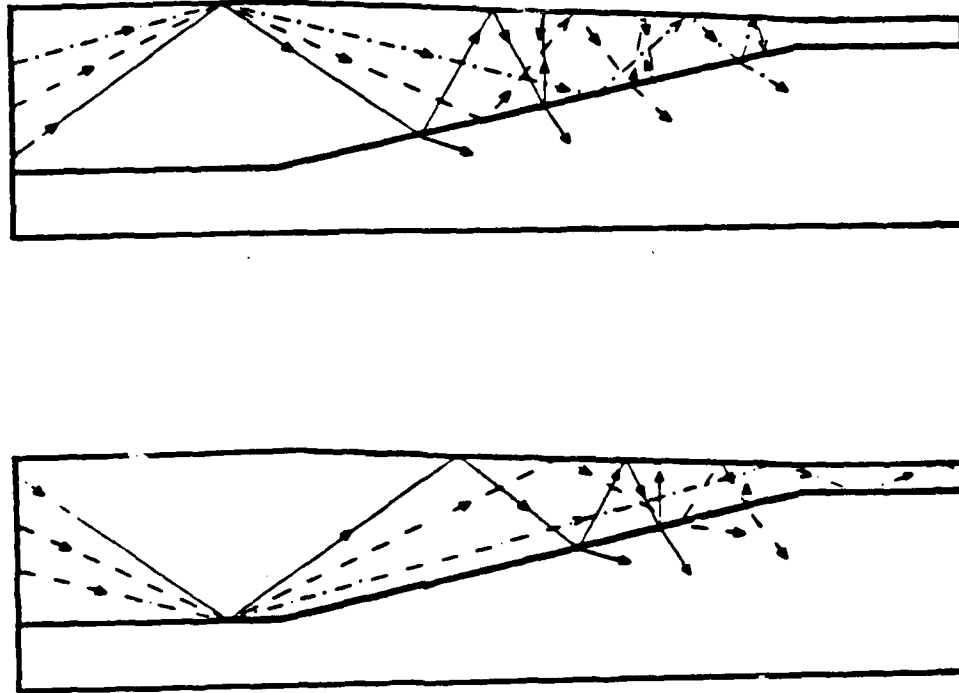


Figure 22: Illustration of ray paths within a forward transition structure. Each diagram shows rays with angles of incidence, i , 55° , 65° , and 75° , at the free surface and crust mantle interface in the continental portion of the model. The transition structure within which the rays are traveling is a 100 km forward transition drawn to scale. The upper diagram shows propagation paths for rays that encounter the crust mantle boundary before the crust water boundary. The lower diagram shows propagation paths for rays that encounter the crust ocean boundary before the crust mantle boundary. The arrows indicate the direction of propagation of the wavefront along the ray.

AD-A194 002

BODY AND SURFACE WAVE MODELING OF OBSERVED SEISMIC
EVENTS PART 2(U) CALIFORNIA INST OF TECH PASADENA
SEISMOLOGICAL LAB R W CLAYTON ET AL. 12 MAY 87

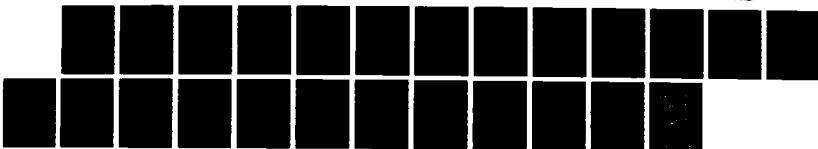
2/2

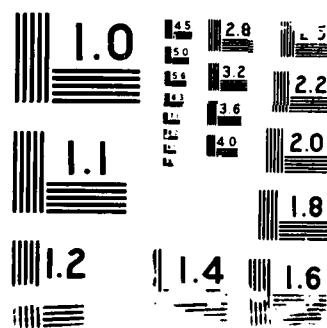
UNCLASSIFIED

AFGL-TR-87-0156 F19620-85-K-0017

F/G 0/11

NL





show the same three multiply reflected rays. These rays are for sample angles of incidence, $i = 55^\circ, 65^\circ$ and 75° , at the crust mantle interface of the continental structure. The angles chosen give a good sampling of the possible range of post-critical incident angles, $> 51^\circ$. The arrows on the rays show the direction of propagation. To avoid cluttering the ray diagrams the incident angles, i , at the crust mantle interface in the continental structure, j , at the crust mantle boundary in the transition, and j' , the angle between the transmitted ray and the normal to the boundary are illustrated only in the first diagram in Figure 15. To explain some of the above effects multiple reflections within the transition region will be considered. To differentiate the angles of incidence for the later reflections within the transition region from j , the angle of incidence at the first boundary encountered in the transition region, an addition to the notation will be made. In further discussions the incident angle j , will become j_1 , and the incident angle for subsequent reflections within and following the transition will be denoted j_n , where n denotes the n^{th} reflection of the ray after it enters the transition region. Similarly, the transmitted rays for the n^{th} reflection of a ray after entering the transition region, will be denoted j'_n . Also useful in the following discussions is the transmission coefficient as a function of the incident angle, j_n . For the examples discussed here the displacement transmission coefficient, $T = \frac{2\cos(j)}{\cos(j) + 1.62\cos(j')}$, varies monotonically between zero for the critical angle $j=51^\circ$, and .76 for normal incidence, $j=0$.

Most of the properties of the wavefield that vary with the length of the forward transition are illustrated in the FE results shown in Figures 23 and 24. The amplitudes represented in these figures are RMS amplitudes calculated using a window length of sixty seconds or less. Figure 23a illustrates the variation in the RMS amplitudes with distance along the surface of the crustal layer for each forward transition model. Figure 24 shows the variation in the RMS amplitudes with depth at distances

corresponding to depth sections A, B, C, D, and E shown in Figure 1, and at an additional depth section ten kilometers further from the source than depth section E. These figures will be used to demonstrate the changes in the properties of the wavefield as it propagates through different forward transitions.

Figure 23a shows the variation of 60s RMS amplitude with distance, Δ , from the source for each of the forward transition FE calculation. The results of the FE calculations for each forward transition region are represented by a line labeled with the length of that transition region. The lines were determined by measuring RMS amplitudes at grid points along the surface of the crustal layer, at intervals of five kilometers, and drawing a line through the resulting points. The vertical axis shows the RMS amplitudes. Since the relative amplitudes produced using the different forward transition amplitudes are being compared the absolute values of the amplitudes are not shown. These absolute values will change according to the moment of the source. The horizontal axis shows the distance, Δ , from the source. The vertical lines labeled B and D are at distances from the source corresponding to the beginnings and the ends of the transitions respectively. The horizontal axis does not have the same scale for all transitions. The scales are identical for all transitions within the region of continental structure to the left of the transition region and within the region of oceanic structure to the right of the the transition region. However, within the transition region, between B and D, the horizontal scale is different for each calculation. Amplitudes recorded within each transition region are plotted with respect to an origin at B, the beginning of the transition region. Consider that the distance between B and D on the plot is BD centimeters. If the horizontal distance from B to the node at which the amplitude is recorded, for a transition of length L kilometers, is x kilometers, then the observation is plotted at a point a distance $(x/L)BD$ centimeters to the right of B. This method of plotting shows the changes in amplitude through the transitions of

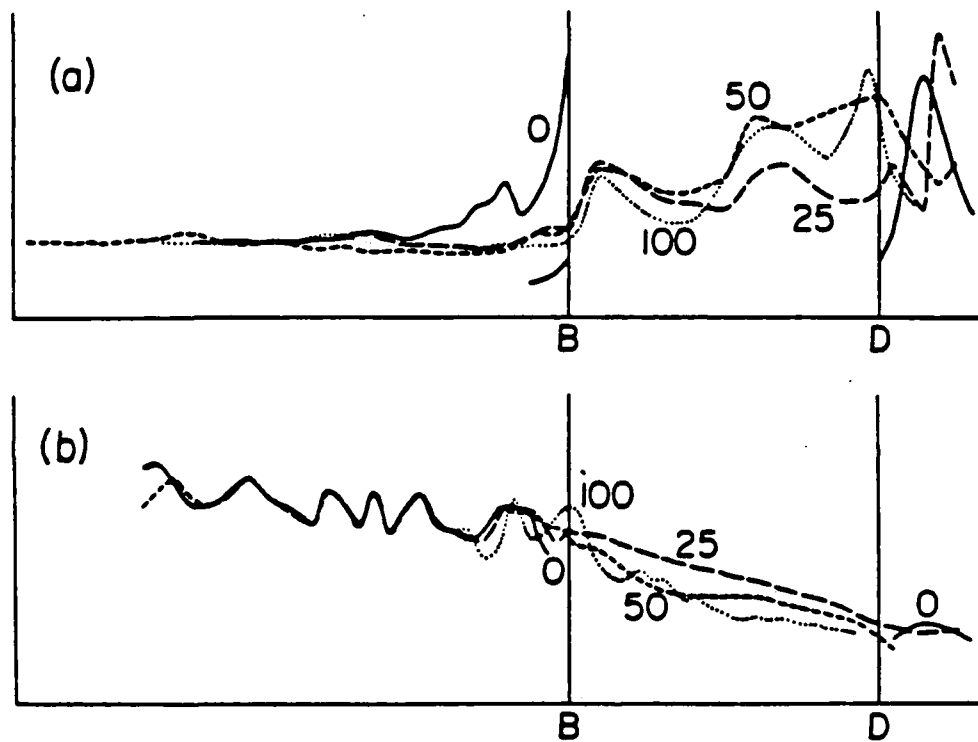


Figure 23: Variation of surface amplitude along the surface of each transition. The upper sketch shows the variation in RMS amplitude (60s) along the surface of each forward transition model. The lower sketch shows the amplitude (50s RMS) distance relation of surface amplitudes for each reverse transition. Amplitude is recorded as the y coordinate. The distance scale is not uniform along the whole x axis. The two vertical lines indicate the limits of the transition region. Outside the transition region the scale is uniform. Within the transition region distances are plotted, with respect to an origin at the beginning of the transition region, as fractions of the transition length. All data points lie on the indicated lines except for some scatter in the 100 km transition results.

various lengths within the same region of the plot. The amplitudes recorded at nodes along the surface of the crustal layer within each transition region show a general increase as one moves from B towards D. The size of this increase is smallest for the step transition and increases as the length of the transition increases. Superimposed on the general increase of amplitude is an oscillatory term. The method of scaling the distance coordinate within the transition region makes the coincidence of maxima and minima at approximately the same fraction of the transition length for all transitions considered very clear. Thus, the variations of amplitude along the surface of the crustal layer in the transition show similar patterns for all transition lengths, and the widths of the fluctuations in amplitude along the surface of the crustal layer within the transition region are approximately proportional to the width of the transition region. If no transition region is present in the grid the increases in amplitude before reaching distance B would not be seen. These increases are due to the presence of energy reflected from the transition back towards the source. The increase is largest for a step transition and decreases as the length of the transition increases. The fluctuations in amplitude following the transition region shows that the wavefield has not stabilized in the few kilometers beyond the transition regions illustrated in this figure.

Figure 24 shows the variation of 50m RMS amplitude with depth recorded at distances corresponding to depth sections A, B, C, D, and E in Figure 1a, and an additional depth section ten kilometers to the right of depth section E. Six individual graphs are shown to illustrate the variation of amplitude with depth in the forward transition models. Each depth section is represented by one graph. Each of these graphs is labeled in the upper left corner with the letter that identifies the depth section on which the illustrated amplitudes were recorded. The unlabeled plot is for the sixth depth section. The vertical axis of each plot shows the depth. The upper end of

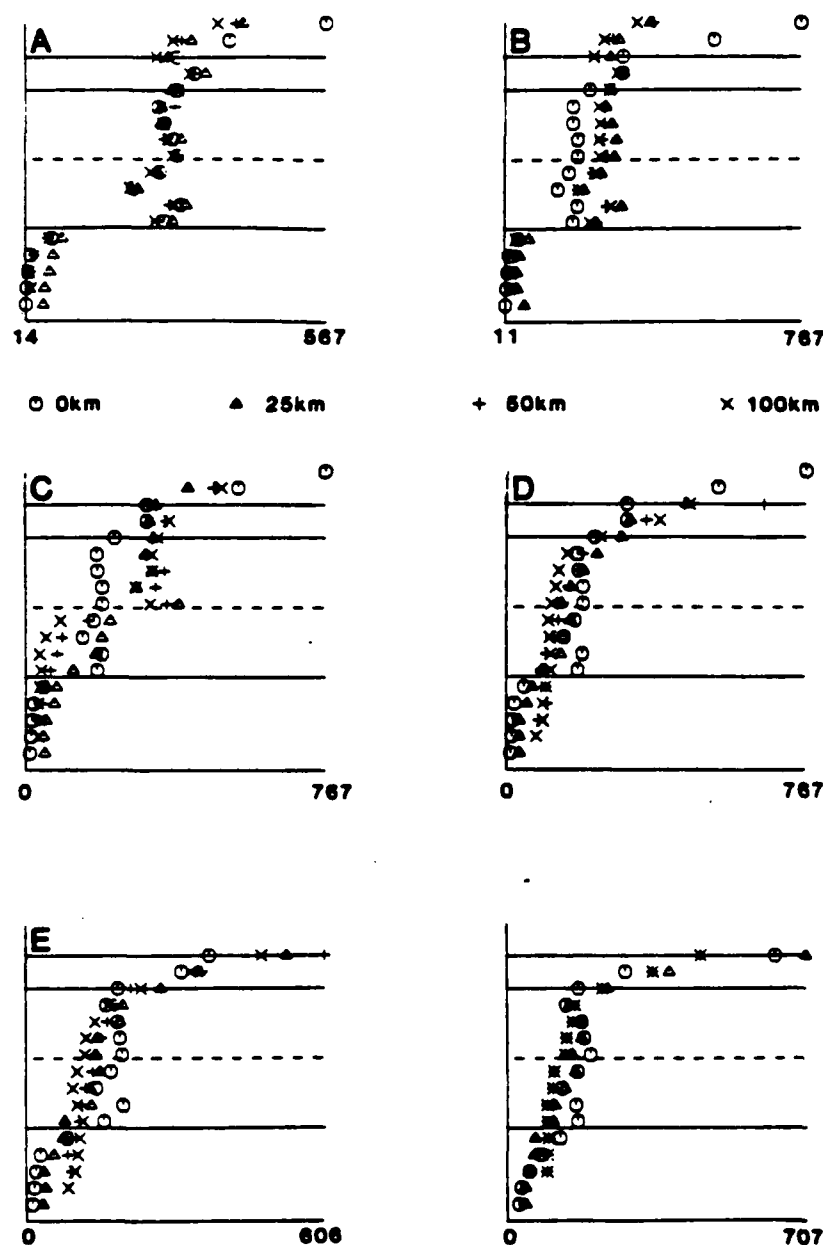


Figure 24: Variation of 55s RMS amplitude with depth on depth sections A, B, C, D, E, of Figure 1 for each forward transition model. An additional depth section 10 km to the right of depth section E is also illustrated. Each plot illustrates results for one depth section. The letter at the upper left of each plot identifies the location of the depth section as illustrated in Figure 1. The three solid horizontal lines are, from top to bottom, the surface and base of the oceanic crustal layer, and the base of the continental crustal layer. The dashed horizontal line shows the depth of the base of the crustal layer in depth section C, at the center of the transition region.

the vertical axis corresponds to the surface of the continental crust. The uppermost solid horizontal line corresponds to the depth of the surface of the oceanic crustal layer. The central solid horizontal line is at a depth corresponding to the bottom of the oceanic crustal layer. The lowermost solid horizontal line shows the depth of the bottom of the continental crustal layer. The dotted horizontal line shows the depth of the bottom of the crustal layer in the transition region at the distance of depth section C. The horizontal axis shows the amplitude of the seismograms. The labels on the horizontal axes show the values of amplitudes at the ends of these axes. Although the length of the horizontal axis is fixed the scale on it is determined by the points with the largest and smallest amplitudes so the scales of each graph differ. The values of amplitude at the ends of the horizontal axis are given to facilitate comparison between results at different distances. Each symbol on any of these graphs represents the RMS amplitude of a seismogram. Each transition length is plotted using a different symbol. A legend defining which symbol represents each transition length is shown below the first row of graphs. A subset of nodes on each depth section was chosen to be included in the appropriate graph. The surface node and nodes equally spaced down the depth section with a separation of 2.5 km were included in this subset.

The increase in amplitude for seismograms at crustal surface nodes at distances ranging from B to D can be explained in terms of amplitude concentrated at the surface of the crustal layer in the transition. Concentrated amplitude is observed as an increase in amplitude of seismograms in the oceanic crustal layer of the transition region, at depths between the surface and ten kilometers, with respect to the amplitudes of seismograms at the same distance from the source and depth, calculated using the forward reference model and the same input forcing functions. In Figure 23a the magnitude of the energy concentrated at the surface of the crustal layer in the transition is seen to increase as the length of the transition increases. In Figure 24 this

tendency is seen to apply within the crustal layer of the transition region. This behavior can be explained using the Figures 15 and 22 and observing the differences between them. In a transition region of any length greater than zero the angles of incidence, j , are less than the angles of incidence, i . Decreasing this angle j will cause the reflection points at the boundaries in the transition region to become closer together. This implies that the density of rays will increase in the transition producing higher amplitudes there. As the length of the transition increases the number of bounces within the transition increases and the angle of incidence is reduced producing increases concentration of amplitude. These effects would be equally efficient at a crust mantle boundary with the same slope if transmission of amplitude across that boundary was not a factor. However, the amplitude concentrated at the crust mantle boundary is partially transmitted across it. Thus the concentration of amplitude near the crust mantle boundary is offset by the escape of energy across it.

At depths corresponding to the crust water boundary the amplitude of the component of the seismogram reflected back into the continental layer, that is back toward the source, decreases as the length of the transition increases. This is also true for the amplitude of the component of the seismograms reflected back into the continental layer at depths corresponding to the depth of the crust mantle boundary. The reflected component of the seismogram is defined to be that component which remains when a hybrid seismograms recorded on depth section A (Figure 1) in a forward transition calculation have the hybrid seismogram at the same depth and distance from the source, recorded during the forward reference calculation, subtracted from it. The amplitudes referred to in this discussion are the RMS amplitudes of seismograms taken using a fifty five second window. The amplitude of the reflected components of the seismograms is much smaller below the bottom of the oceanic crustal layer than above it regardless of the length of the transition.

The reduction in the reflected amplitude as the length of the transition increases is easily explained by observing important differences between Figures 15 and 22. Two different effects contribute. First, as the length of the transition region increases the amount of amplitude concentrated at the crust ocean boundary and thus transmitted into the oceanic crustal layer increases. This reduces the amount of amplitude reflected back toward the source. Second, in the longer transition regions more energy is able to escape into the half-space across the crust mantle boundary. This effect also decreases the amount of amplitude available to be reflected. The cause of the increase in transmission across the crust mantle boundary as the length of the transition increases can be explained by considering the angles ϕ_{CM} , and ϕ_{CO} as shown in Figure 1. Reducing these angles, that is increasing the length of the transition, allows more reflections of a given ray within the transition region before it reaches the oceanic crustal layer or is reflected back toward the continental structure. For each of these reflections the angle of incidence is $j_n = j_1 - (n-1)(\phi_{CM} + \phi_{CO})$. When this angle becomes negative the ray returns toward the source. Clearly, for smaller values of the angles ϕ_{CM} , and ϕ_{CO} more bounces can occur before the ray turns back toward the source or enters the oceanic structure. Each time the ray bounces the angle j_n is smaller, so the angle j'_n is smaller. Thus, the amount of amplitude transmitted across the transition increases, and the angle of incidence of the disturbance transmitted into the half-space with the grid bottom boundary increases. The transmission of additional energy across the transition leaves less energy within the crustal layer to be reflected back towards the source.

The Dependence of Changes to L_g Wavetrains Passing through a

Reverse Transition Region on Transition Length

The reverse transition tests also illustrate the behavior of properties dependent on the length of the transition region. A longer transition is more effective at reducing

surface amplitudes. Examination of Figure 23b shows that the surface amplitude decay across the transition is monotonic for the shorter reverse transitions and shows a small oscillatory component for calculations using longer reverse transition models. The figure also shows the surface amplitude vs. distance relation along the oceanic portion of the path is oscillatory. This oscillatory behavior is also observed for the oceanic reference model calculation, where it is superimposed upon a slow decrease in amplitude. The amplitude distributions with depth indicate that energy is traveling down from the crustal surface, spreading throughout the crustal layer. Some of the energy eventually escapes across the crust mantle boundary in the region of continental structure. The amplitudes in the crustal layer of the transition distribute themselves over a larger depth range in a longer transition. Thus the amplitude originally traveling in the oceanic crustal layer has time to distribute itself over a larger depth range when it is traveling through a longer transition. The amount of amplitude incident on the reverse transition from the half space is transmitted into the crustal layer. The amplitudes below the crustal layer of the transition region do not die off as strongly with depth as they do in the forward transition case, in fact the amplitudes may even increase with depth below the crustal layer as seen in Figure 25. The increase with depth below the crustal layer indicates that amplitude is traveling down toward the grid bottom and out of the system being considered. It appears that it is in the reverse transition and the propagation through the intermediate oceanic layer that causes the attenuation of L_g type waves when they travel across a mixed path containing an oceanic region.

Figure 23b shows the variation of 50s RMS amplitude with distance from the source, Δ , for each of the reverse transition FE calculations. The RMS amplitudes determined during a reverse transition calculation are depicted in this figure by a line labeled with the length of the forward transition region model in which they are

determined. The vertical axis shows the RMS amplitudes. Since the amplitudes produced using the different reverse transition models are dependent on the moment of the source and the effects being investigated are the amplitude variations caused by modifying the transition models numerical values on the amplitude axis are unnecessary. The horizontal axis shows the distance, Δ , from the source. The vertical lines labeled B and D show the locations of the ends of the transitions. The scale on the horizontal axis between B and D is different for each transition length and is defined in the same manner as the scales within the forward transition region shown in Figure 23a. This method of scaling shows the changes in amplitude through the reverse transition regions of various lengths within the same region of the plot. The amplitudes recorded at nodes along the surface of the crustal layer within each reverse transition region show a general decrease as one moves from B towards D. The size of this decrease is smallest for the step transition and increases as the length of the transition increases. Superimposed on the general increase of amplitude is an oscillatory term. The sizes of the oscillations seen in the reverse transition results are much smaller than those seen in the forward transition results. The fluctuations appear to be confined near the beginning of the transition region for the reverse transition case as opposed to distributed throughout the transition for the forward transition case. The amplitudes of the fluctuations in the reverse transition case are approximately proportional to the width of the transition region. The curve for the 25km reverse transition shows no visible fluctuations. For the 100km reverse transition the fluctuations begin smaller than those seen in the oceanic structure and are rapidly reduced as the wavefield passes through the transition. The oscillation in amplitude following the transition region shows that the wavefield has not stabilized in the few kilometers beyond the transition regions illustrated in this figure. The differences between the results for the different transition lengths immediately preceding the transition region

suggests that some type of reflection, diffraction, or scattering from the transition region is affecting the wavefield immediately adjacent to the start of the transition region.

Figure 25 shows the variation of 50s RMS amplitude with depth on depth sections A, B, C, D, and E in Figure 1b, and an additional depth section ten kilometers to the right of depth section E. Each of these depth sections is represented by one of the six individual graphs shown in the figure. Each of these graphs is labeled in the upper left corner with the letter that identifies the depth section on which the illustrated amplitudes were recorded. The unlabeled plot is for the sixth depth section. The vertical axis of each plot shows the depth. The upper end of the vertical axis corresponds to the surface of the continental crust. The horizontal lines within each graph, from the uppermost to the lowermost, are at the depths of the surface, the surface of the oceanic crustal layer, the base of the oceanic crustal layer, the base of the crustal layer at depth section C, and the base of the continental crustal layer respectively. The labels on the horizontal axes show the values of amplitudes at the ends of these axes. These values of amplitude are given to facilitate comparison between the individual graphs, each of which has a different horizontal scale. The RMS amplitudes of seismograms at the surface and equal intervals of length 2.5 km down each depth section are shown as centered symbols on the graph for that depth section. Each transition length is plotted using a different symbol. A legend defining which symbol represents each transition length is shown below the first row of graphs.

The length of the intermediate oceanic path between the continent to ocean and the ocean to continent transition is also being investigated. Calculations for two distances have been completed using single FE calculations. Calculations for an additional, longer, distance were done using multiple FE calculations to go from the edge of the first transition model to the receiver. Due to computational limits, the lengths

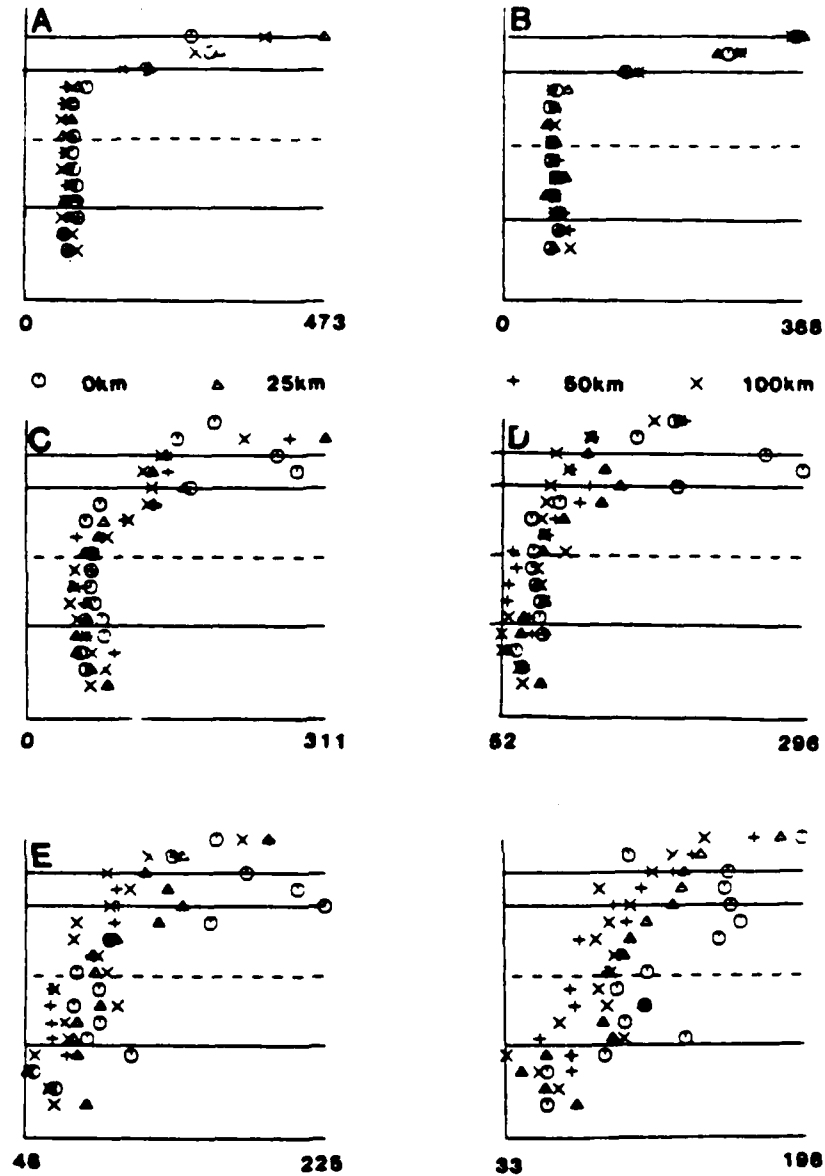


Figure 25: Variation of 55s RMS amplitude with depth on depth sections A, B, C, D, E, of Figure 1 for each reverse transition model. Each plot illustrates results for one depth section. The letter at the upper left of each plot identifies the location of the depth section as illustrated in Figure 1. The horizontal lines are at the same depths as in Figure 24.

of these intermediate paths are short, but definitely within the range of interest. Lengths of 30, 70, and 120 km, have been used. For the shortest paths energy transmitted in to the mantle layer has little time to travel towards the bottom of the grid and thus out of the region of consideration before much of it passes back into the crustal layer as it travels through the reverse transition. This implies that there may be a critical length of intermediate oceanic path beyond which enough of the energy has been propagated through the crust mantle boundary or leaked from the oceanic structure and subsequently escaped from the region of interest that amplitudes of the attenuated L_g recorded after the reverse transition would be reduced to the invisible level due to dilution caused by propagation through the reverse transition region. To completely analyze this assertion models using longer path lengths of intermediate oceanic structure should be considered. In order to investigate longer path lengths in the oceanic structure the RT coupling method for continuing FE calculations through a plane layered structure using RT integration and propagator matrix Green's functions must be used. The accuracy of the numerical implementation of this method must be established before such calculations can be presented. Therefore, the discussion of the numerical implementation of this method and of the results examining the effects of the intermediate path length in the oceanic structure will be left for the next chapter.

Conclusions

In conclusion, a summary of the important observations of the effects of regions of thinning or thickening of the crust on SH L_g type wavefields will be given. First the effects of a forward transition on the incoming SH L_g mode sum seismograms will be summarized. Then, the further effects due to continued propagation of this energy through a reverse transition will be stated in brief. Next, the variation in the effects introduced by the forward transition as a function of transition length will be summed up. Finally, the variations in the effects observed as the wavefront passes through the

reverse transition, as a function of the length of that transition will be summarized. The consideration of the effects due to varying the length of the oceanic path between the two transition regions has been mentioned, but, the detailed discussion of this problem and its summary is reserved for the next chapter.

Now, the effects produced when a SH L_g mode sum wavefield is propagated through a 20km forward transition region will be summarized. First, amplitudes at the surface of the crust are amplified by about fifty percent as the wavefield passes through the transition region. These amplitude increases decrease in magnitude with depth becoming net decreases at the bottom of the oceanic crustal layer. These increases and their behavior with depth can be understood by noticing that as a ray travels through a transition region the distance between successive reflection points decreases thus amplitude concentrated at the surfaces of the crustal layer. However, amplitude is transmitted across the crust mantle boundary and not across the crust ocean boundary. Thus, the concentration at the crust ocean boundary is maximum at the surface and decays with depth. The concentration effect at the crust mantle boundary is masked by the transfer of amplitude across that boundary. The amplitudes in the mantle layer are largest directly below the crust and decay rapidly with depth. The amplitude transmitted across the crust mantle boundary in the transition region propagates at some angle toward the grid bottom as x is increased. The angle that the wavefront formed by this amplitude makes with the grid bottom boundary increases as the width, in x , of the triangular regions of maxima incident from the continental structure increase. Thus, as the phase velocity decreases later in the record this angle increases. The actual size of that angle is dependent on the angle the crust mantle boundary makes with the horizontal, ϕ_{CM} , and is the complement of the difference between the incident angle in the continental structure and the angle ϕ_{CM} . Amplitude crosses the crust mantle transition into the oceanic structure. This leakage

is largest near the end of the transition region and decreases with distance away from it.

Next, a summary of the important observations for the reverse transition will be given. First, amplitudes at the surface of the crustal layer decrease as the wavefield travels through the oceanic layer. The size of this change in amplitude decreases as the propagation distance in the oceanic crustal layer increases. The size of the decrease in amplitude is controlled by the amplitude of wavefronts propagating through the oceanic crustal layer with pre-critical angles of incidence. At each successive reflection of such a wavefront from the crust mantle interface in the oceanic structure, the same fraction of a remaining total amplitude is transmitted across the boundary. Thus, the total amplitude of this component decays most rapidly in the first kilometers of transmission through the oceanic structure while the incident wave still has higher amplitudes. As the wavefield travels through the reverse transition region the surface amplitude reduces rapidly as the concentrations of amplitude previously trapped in the oceanic crustal layer travel up the ocean crust boundary while spreading themselves throughout the depth extent of the crustal layer. The maxima in these regions remain at the surface. At the end of the transition region the amplitude reduces rapidly with depth down to the crust mantle interface. The amplitude incident upon the mantle crust boundary from the oceanic half-space is transmitted across it with a resulting distortion in the wavefield. The form of this distortion is the superposition of a slope, $\text{Slope} = \tan^{-1} \left[\frac{1(v_M - v_c)}{v_M} \right]$, onto the disturbance incident at the mantle crust boundary after it has passed into the continental crustal layer.

Now, the properties of the calculated amplitudes in a forward transition model which depend on the length of the forward transition model will be summarized. First, RMS amplitudes recorded at nodes along the surfaces of the crustal layers show

that amplitude in the transition region increases as the crustal layer thins. The size of the increase is largest for the longest transitions. This is explained by considering that the incident angles at the boundaries in the transitions decrease as the transition region thins, thus, increasing the density of rays and the amplitudes at the transition boundaries. As the crustal layer thins, a similar increase in amplitude at the crust mantle might be expected. However, the amount of amplitude concentrated at the boundary decreases as the angle ϕ_{CM} or ϕ_{CO} increases. The steeper angle of the crust mantle boundary should cause a much smaller concentration at the crust half-space boundary than that seen at the crust ocean boundary. In addition amplitude propagates across the crust mantle boundary and thus any energy concentration at that boundary immediately travels across it. The amount of energy transmitted across the crust mantle boundary increases as its length increases. The increase in transmission across the crust mantle boundary as the length of the transition region increases is explained by the increased number of reflections within a longer transition region. Since amplitude from each ray enters the mantle half-space at each reflection, more reflections produce more transmitted amplitude. The wavefield created by the transmitted energy propagates through the grid towards its base more rapidly as the phase velocity decreases. As discussed earlier, the wavefield also propagates downward more rapidly as the length of the transition region increases. The angle of incidence of the transmitted ray with the horizontal is, $i_b = j_a' + \phi_{CM}$. Clearly, for a longer transition with a smaller ϕ_{CM} the rays are more nearly normally incident at the grid bottom. Thus, for a gentle transition the path length in the oceanic structure that will allow the transmitted energy to escape the system and not reenter the reverse transition is shorter than for a steeper transition region.

DARPA SUPPLEMENTAL LIST FOR TECHNICAL REPORTS (Unclassified)
DISTRIBUTION LIST

Dr. Monem Abdel-Cawad
Rockwell International Science Center
1049 Camino Dos Rios
Thousand Oaks, CA 91360

Professor Keiti Aki
Center for Earth Sciences
University of Southern California
University Park
Los Angeles, CA 90089-0741

Professor Shelton S. Alexander
Geosciences Department
403 Deike Building
The Pennsylvania State University
University Park, PA 16802

Professor Charles B. Archambeau
Cooperative Institute for Research in
Environmental Sciences
University of Colorado
Boulder, CO 80309

Dr. Thomas C. Bache Jr.
Science Applications Int'l Corp.
10210 Campus Point Drive
San Diego, CA 92121

Dr. James Bulau
Rockwell International Science Center
1049 Camino Dos Rios
P.O. Box 1085
Thousand Oaks, CA 91360

Dr. Douglas R. Baumgardt
Signal Analysis and Systems Division
ENSCO, Inc.
5400 Port Royal Road
Springfield, VA 22151-2388

Dr. S. Bratt
Science Applications Int'l Corp.
10210 Campus Point Drive
San Diego, CA 92121

Professor John Ebel
Department of Geology & Geophysics
Boston College
Chestnut Hill, MA 02167

Woodward-Clyde Consultants
Attn: Dr. Lawrence J. Burdick
Dr. Jeff Barker
P.O. Box 93245
Pasadena, CA 91109-3245 (2 copies)

Dr. Roy Burger
1221 Serry Rd.
Schenectady, NY 12309

Professor Robert W. Clayton
Seismological Laboratory
Division of Geological and Planetary
Sciences
California Institute of Technology
Pasadena, CA 91125

Dr. Vernon F. Cormier
Earth Resources Laboratory
Department of Earth, Atmospheric and
Planetary Sciences
Massachusetts Institute of Technology
42 Carleton Street
Cambridge, MA 02142

Professor Anton M. Dainty
Earth Resources Laboratory
Department of Earth, Atmospheric and
Planetary Sciences
Massachusetts Institute of Technology
42 Carleton Street
Cambridge, MA 02142

Dr. Zoltan A. Der
Teledyne Geotech
314 Montgomery Street
Alexandria, VA 22314

Prof. Adam Dziewonski
Hoffman Laboratory
Harvard University
20 Oxford St.
Cambridge, MA 02138

Professor John Ferguson
Center for Lithospheric Studies
The University of Texas at Dallas
P.O. Box 830688
Richardson, TX 75083-0688

Dr. Jeffrey W. Given
Sierra Geophysics
11255 Kirkland Way
Kirkland, WA 98033

Prof. Roy Greenfield
Geosciences Department
403 Deike Building
The Pennsylvania State University
University Park, PA 16802

Professor David G. Harkrider
Seismological Laboratory
Division of Geological and Planetary
Sciences
California Institute of Technology
Pasadena, CA 91125

Professor Donald V. Helmberger
Seismological Laboratory
Division of Geological and Planetary
Sciences
California Institute of Technology
Pasadena, CA 91125

Professor Eugene Herrin
Institute for the Study of Earth & Man
Geophysical Laboratory
Southern Methodist University
Dallas, TX 75275

Professor Robert B. Herrmann
Department of Earth and Atmospheric
Sciences
Saint Louis University
Saint Louis, MO 63156

Professor Lane R. Johnson
Seismographic Station
University of California
Berkeley, CA 94720

Professor Thomas H. Jordan
Department of Earth, Atmospheric and
Planetary Sciences
Massachusetts Institute of Technology
Cambridge, MA 02139

Dr. Alan Kafka
Department of Geology & Geophysics
Boston College
Chestnut Hill, MA 02167

Professor Charles A. Langston
Geosciences Department
403 Deike Building
The Pennsylvania State University
University Park, PA 16802

Professor Thorne Lay
Department of Geological Sciences
1006 C.C. Little Building
University of Michigan
Ann Arbor, MI 48109-1063

Dr. George R. Mellman
Sierra Geophysics
11255 Kirkland Way
Kirkland, WA 98033

Professor Brian J. Mitchell
Department of Earth and Atmospheric
Sciences
Saint Louis University
Saint Louis, MO 63156

Professor Thomas V. McEvilly
Seismographic Station
University of California
Berkeley, CA 94720

Dr. Keith L. McLaughlin
Teledyne Geotech
314 Montgomery Street
Alexandria, VA 22314

Professor Otto W. Nuttli
Department of Earth and Atmospheric
Sciences
Saint Louis University
Saint Louis, MO 63156

Professor Paul G. Richards
Lamont-Doherty Geological Observatory
of Columbia University
Palisades, NY 10964

Dr. Norton Rimer
S-Cubed
A Division of Maxwell Laboratory
P.O. 1620
La Jolla, CA 92038-1620

Professor Larry J. Ruff
Department of Geological Sciences
1006 C.C. Little Building
University of Michigan
Ann Arbor, MI 48109-1063

Professor Charles G. Sammis
Center for Earth Sciences
University of Southern California
University Park
Los Angeles, CA 90089-0741

Dr. David G. Simpson
Lamont-Doherty Geological Observatory
of Columbia University
Palisades, NY 10964

Dr. Jeffrey L. Stevens
S-CUBED,
A Division of Maxwell Laboratory
P.O. Box 1620
La Jolla, CA 92038-1620

Professor Brian Stump
Institute for the Study of Earth
and Man
Geophysical Laboratory
Southern Methodist University
Dallas, TX 75275

Professor Ta-liang Teng
Center for Earth Sciences
University of Southern California
University Park
Los Angeles, CA 90089-0741

Dr. R. B. Tittmann
Rockwell International Science Center
1049 Camino Dos Rios
P.O. Box 1085
Thousand Oaks, CA 91360

Professor M. Nafi Toksoz
Earth Resources Laboratory
Department of Earth, Atmospheric and
Planetary Sciences
Massachusetts Institute of Technology
42 Carleton Street
Cambridge, MA 02142

Professor Terry C. Wallace
Department of Geosciences
Building #11
University of Arizona
Tucson, AZ 85721

Prof. John H. Woodhouse
Hoffman Laboratory
Harvard University
20 Oxford St.
Cambridge, MA 02138

Dr. G. Blake
US Dept of Energy/DP 331
Forrestal Building
1000 Independence Ave.
Washington, D.C. 20585

Dr. Michel Bouchon
Universite Scientifique et
Medicale de Grenoble
Laboratoire de Geophysique
Interne et Tectonophysique
I.R.I.G.M.-B.P. 68
38402 St. Martin D'Heres
Cedex FRANCE

Dr. Hilmar Bungum
NTNF/NORSAR
P.O. Box 51
Norwegian Council of Science,
Industry and Research, NORSAR
N-2007 Kjeller, NORWAY

Dr. Alan Douglas
Ministry of Defense
Blacknest, Brimpton, Reading RG7-4RS
UNITED KINGDOM

Professor Peter Harjes
Institute for Geophysik
Rhur University
Bochum
P.O. Box 102148
4630 Bochum 1
FEDERAL REPUBLIC OF GERMANY

Dr. James Hannon
Lawrence Livermore National Laboratory
P.O. Box 808
Livermore, CA 94550

Dr. E. Husebye
NTNF/NORSAR
P.O. Box 51
N-2007 Kjeller, NORWAY

Dr. Arthur Lerner-Lam
Lamont-Doherty Geological Observatory
of Columbia University
Palisades, NY 10964

Mr. Peter Marshall
Procurement Executive
Ministry of Defense
Blacknest, Brimpton, Reading RG7-4RS
UNITED KINGDOM

Dr. B. Massinon
Societe Radiomana
27, Rue Claude Bernard
75005, Paris, FRANCE

Dr. Pierre Mechler
Societe Radiomana
27, Rue Claude Bernard
75005, Paris, FRANCE

Mr. Jack Murphy
S-CUBED
Reston Geophysics Office
11800 Sunrise Valley Drive
Suite 1212
Reston, VA 22091

Dr. Svein Mykkeltveit
NTNF/NORSAR
P.O. Box 51
N-2007 Kjeller, NORWAY

Dr. Carl Newton
Los Alamos National Laboratory
P.O. Box 1663
Mail Stop C 335, Group ESS3
Los Alamos, NM 87545

Dr. Peter Basham
Earth Physics Branch
Department of Energy and Mines
1 Observatory Crescent
Ottawa, Ontario
CANADA K1A 0Y3

Professor J. A. Orcutt
Geological Sciences Division
Univ. of California at San Diego
La Jolla, CA 92093

Dr. Frank F. Pilotte
Director of Geophysics
Headquarters Air Force Technical
Applications Center
Patrick AFB, Florida 32925-6001

Professor Keith Priestley
University of Nevada
Mackay School of Mines
Reno, Nevada 89557

Mr. Jack Raclin
USGS - Geology, Rm 3C136
Mail Stop 928 National Center
Reston, VA 22092

Dr. Frode Ringdal
NTNF/NORSAR
P.O. Box 51
N-2007 Kjeller, NORWAY

Dr. George H. Rothe
Chief, Research Division
Geophysics Directorate
Headquarters Air Force Technical
Applications Center
Patrick AFB, Florida 32925-6001

Dr. Alan S. Ryall, Jr.
Center for Seismic Studies
1300 North 17th Street
Suite 1450
Arlington, VA 22209-2308

Dr. Lawrence Turnbull
OSWR/NED
Central Intelligence Agency
CIA, Room 5G48
Washington, DC 20505

Professor Steven Grand
Department of Geology
245 Natural History Bldg
1301 West Green Street
Urbana, IL 61801

DARPA/PM
1400 Wilson Boulevard
Arlington, VA 22209

Defense Technical Information Center
Cameron Station
Alexandria, VA 22314 (12 copies)

Defense Intelligence Agency
Directorate for Scientific and
Technical Intelligence
Washington, D.C. 20301

Defense Nuclear Agency
Shock Physics Directorate/SS
Washington, D.C. 20305

Defense Nuclear Agency/SPSS
ATTN: Dr. Michael Shore
6801 Telegraph Road
Alexandria, VA 22310

AFOSR/NPG
ATTN: Director
Bldg 410, Room C222
Bolling AFB, Washington, D.C. 20332

AFTAC/CA (STINFO)
Patrick AFB, FL 32925-6001

AFWL/NTESC
Kirtland AFB, NM 87171

U.S. Arms Control & Disarmament Agency
ATTN: Mrs. M. Hoinkes
Div. of Multilateral Affairs, Rm 5499
Washington, D.C. 20451

U.S. Geological Survey
ATTN: Dr. T. Hanks
National Earthquake Research Center
345 Middlefield Road
Menlo Park, CA 94025

SRI International
333 Ravensworth Avenue
Menlo Park, CA 94025

Center for Seismic Studies
ATTN: Dr. C. Romney
1300 North 17th Street
Suite 1450
Arlington, VA 22209 (3 copies)

Dr. Robert Blandford
DARPA/GSD
1400 Wilson Boulevard
Arlington, VA 22209-2308

Ms. Ann Kerr
DARPA/GSD
1400 Wilson Boulevard
Arlington, VA 22209-2308

Dr. Ralph Alewine III
DARPA/GSD
1400 Wilson Boulevard
Arlington, VA 22209-2308

Mr. Edward Giller
Pacific Sierra Research Corp.
1401 Wilson Boulevard
Arlington, VA 22209

Science Horizons, Inc.
Attn: Dr. Bernard Minster
Dr. Theodore Cherry
710 Encinitas Blvd., Suite 101
Encinitas, CA 92024 (2 copies)

Dr. Jack Evernden
USGS - Earthquake Studies
345 Middlefield Road
Menlo Park, CA 94025

Dr. Lawrence Braille
Department of Geosciences
Purdue University
West Lafayette, IN 47907

Dr. G.A. Bollinger
Department of Geological Sciences
Virginia Polytechnical Institute
21044 Derring Hall
Blacksburg, VA 24061

Dr. L. Sykes
Lamont Doherty Geological Observatory
Columbia University
Palisades, NY 10964

Dr. S.W. Smith
Geophysics Program
University of Washington
Seattle, WA 98195

Dr. L. Timothy Long
School of Geophysical Sciences
Georgia Institute of Technology
Atlanta, GA 30332

Dr. N. Biswas
Geophysical Institute
University of Alaska
Fairbanks, AK 99701

Dr. Freeman Gilbert
Institute of Geophysics &
Planetary Physics
Univ. of California at San Diego
P.O. Box 109
La Jolla, CA 92037

Dr. Pradeep Talwani
Department of Geological Sciences
University of South Carolina
Columbia, SC 29208

University of Hawaii
Institute of Geophysics
Attn: Dr. Daniel Walker
Honolulu, HI 96822

Dr. Donald Forsyth
Department of Geological Sciences
Brown University
Providence, RI 02912

Dr. Jack Oliver
Department of Geology
Cornell University
Ithaca, NY 14850

Dr. Muawia Barazangi
Geological Sciences
Cornell University
Ithaca, NY 14853

Rondout Associates
Attn: Dr. George Sutton
Dr. Jerry Carter
Dr. Paul Pomeroy
P.O. Box 224
Stone Ridge, NY 12484 (3 copies)

Dr. Bob Smith
Department of Geophysics
University of Utah
1400 East 2nd South
Salt Lake City, UT 84112

Dr. Anthony Gangi
Texas A&M University
Department of Geophysics
College Station, TX 77843

Dr. Gregory B. Young
ENSCO, Inc.
5400 Port Royal Road
Springfield, CA 22151

Dr. Ben Menaheim
Weizman Institute of Science
Rehovot, ISRAEL 951729

Weidlinger Associates
Attn: Dr. Gregory Wojcik
620 Hansen Way, Suite 100
Palo Alto, CA 94304

Dr. Leon Knopoff
University of California
Institute of Geophysics & Planetary
Physics
Los Angeles, CA 90024

Dr. Kenneth H. Olsen
Los Alamos Scientific Laboratory
Post Office Box 1663
Los Alamos, NM 87545

Prof. Jon F. Claerbout
Prof. Amos Nur
Dept. of Geophysics
Stanford University
Stanford, CA 94305 (2 copies)

Dr. Robert Burrige
Schlumberger-Doll Research Ctr.
Old Quarry Road
Ridgefield, CT 06877

Dr. Eduard Berg
Institute of Geophysics
University of Hawaii
Honolulu, HI 96822

Dr. Robert Phinney
Dr. F.A. Dahlen
Dept. of Geological & Geophysical Sci.
Princeton University
Princeton, NJ 08540 (2 copies)

Dr. Kin-Yip Chun
Geophysics Division
Physics Department
University of Toronto
Ontario, CANADA M5S 1A7

New England Research, Inc.
Attn: Dr. Randolph Martin III
P.O. Box 857
Norwich, VT 05055

Sandia National Laboratory
Attn: Dr. H.B. Durham
Albuquerque, NM 87185

Dr. Gary McCartor
Mission Research Corp.
735 State Street
P. O. Drawer 719
Santa Barbara, CA 93102

Dr. W. H. K. Lee
USGS
Office of Earthquakes, Volcanoes,
& Engineering
Branch of Seismology
345 Middlefield Rd
Menlo Park, CA 94025

AFGL/XO
Hanscom AFB, MA 01731-5000

AFGL/LW
Hanscom AFB, MA 01731-5000

AFGL/SULL
Research Library
Hanscom AFB, MA 01731-5000 (2 copies)

Secretary of the Air Force (SAFRD)
Washington, DC 20330

Office of the Secretary Defense
DDR & E
Washington, DC 20330

HQ DNA
Attn: Technical Library
Washington, DC 20305

Director, Technical Information
DARPA
1400 Wilson Blvd.
Arlington, VA 22209

Los Alamos Scientific Laboratory
Attn: Report Library
Post Office Box 1663
Los Alamos, NM 87544

Dr. Thomas Weaver
Los Alamos Scientific Laboratory
Los Alamos, NM 87544

Dr. Al Florence
SRI International
333 Ravenswood Avenue
Menlo Park, CA 94025-3493

END

DATE

FILMED

8-88

DTIC